

ELECTROMAGNETIC ANALYSIS AND DESIGN OF  
SEMICONDUCTOR QUBIT STRUCTURES FOR THE  
REALIZATION OF THE QUANTUM COMPUTER

HAMIDREZA MIRZAEI

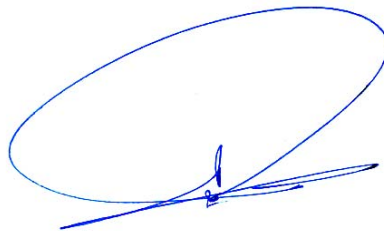
A THESIS SUBMITTED  
FOR THE DEGREE OF DOCTOR OF PHILOSOPHY  
DEPARTMENT OF ELECTRICAL AND COMPUTER  
ENGINEERING  
NATIONAL UNIVERSITY OF SINGAPORE

2013

### **Declaration**

I hereby declare that this thesis is my original work and it has been written by me in its entirety. I have duly acknowledged all the sources of information which have been used in the thesis.

This thesis has also not been submitted for any degree in any university previously.

A handwritten signature in blue ink, consisting of a large, sweeping loop followed by a horizontal line and a small vertical stroke.

HAMIDREZA MIRZAEI

14 August 2013

## **Acknowledgments**

It would not have been possible to write this doctoral thesis without the help and support of the kind people around me, to only some of whom it is possible to give particular mention here.

I would like to express my greatest appreciations to my supervisor professor Hon Tat Hui. This thesis would not have been possible without his help, support and patience, not to mention his advice and unsurpassed knowledge of the related subjects. He has been invaluable on both an academic and a personal level, for which I am extremely grateful.

I would like to acknowledge the financial, academic and technical support of the National University of Singapore and Department of Electrical and Computer Engineering particularly in the award of a Postgraduate Research Scholarship that provided the necessary financial support for my research. The facilities provided in the Radar and Signal Processing Lab (RSPL), have been indispensable.

I am most grateful to all my friends in Singapore, Hamed Kiani, Meisam Kouhi, Mahdi Movahednia and Mohsen Rahmani, for their support and encouragement throughout the PhD years. Also, I give my heartiest appreciation to all my friends elsewhere in the world for their consistent friendship and support through all these years. I also would like to thank my friend Jack, RSPL technician, for all his support, knowledge and efforts in providing a wonderful environment in the Lab.

Above all, I would like to thank my lovely and loving girlfriend Farzaneh for her personal support and great patience at all times, not to mention her

priceless help in editing my PhD thesis. My parents, my brother Omid and my sister Arezoo have given me their unequivocal support throughout, as always, for which my mere expression of thanks likewise does not suffice.

For any errors or inadequacies that may remain in this work, of course, the responsibility is entirely my own.

## Table of Contents

<b>Declaration.....</b>	<b>i</b>
<b>Acknowledgments .....</b>	<b>ii</b>
<b>Table of Contents .....</b>	<b>iv</b>
<b>Summary.....</b>	<b>vii</b>
<b>List of Tables .....</b>	<b>viii</b>
<b>List of Figures.....</b>	<b>ix</b>
<b>List of Symbols.....</b>	<b>xii</b>
<b>Chapter 1. Introduction.....</b>	<b>1</b>
1.1 Quantum Computation: Introduction and History .....	2
1.2 Quantum Bit.....	4
1.2.1 Silicon Qubits.....	6
1.2.2 Donor-based Spin Qubits.....	10
1.3 Nuclear Magnetic Resonance (NMR).....	15
1.3.1 The Nuclear Resonance Effect.....	16
1.3.2 NMR Solid State Quantum Computer .....	22
1.4 Research Motivation .....	26
1.5 Organization of the Thesis .....	29
<b>Chapter 2. Theoretical Analysis.....</b>	<b>32</b>
2.1 Effective Mass Theory for Silicon-Based Devices .....	35
2.2 Perturbation Theory.....	36

2.2.1	First Order Perturbation Theory.....	40
2.2.2	Second Order Perturbation Theory .....	41
2.2.3	Implementation of Perturbation Theory in the Qubit Problem..	44
2.3	Summary .....	47
<b>Chapter 3. The Electromagnetic Numerical and Simulation Method .....</b>		<b>48</b>
3.1	Using Multi-layered Green Function to Solve the Integral Equation	49
3.2	Using Computer-Aided Simulation Method .....	53
3.2.1	Finite Integration Method and Discrete Electromagnetism .....	54
3.2.2	CST Electrostatic Solver.....	59
3.3	Summary .....	62
<b>Chapter 4. Accurate Analysis of the NMR Frequency of the Donor Atom Inside the A-Gate Structure.....</b>		<b>63</b>
4.1	The Quantum Perturbation Method Combined With Accurate EM Simulation .....	65
4.2	Potential Distribution Results.....	68
4.3	Summary .....	72
<b>Chapter 5. Electron Magnetic Resonance Analysis of the Electron-Spin Based Qubit .....</b>		<b>73</b>
5.1	Perturbation Analysis for the Electron-Spin Magnetic Resonance Frequency.....	75
5.2	Numerical Results .....	77
5.3	Summary .....	80

<b>Chapter 6. Alternative A-Gate Structures.....</b>	<b>81</b>
6.1 The Proposed New A-Gate Structures .....	84
6.2 The Performance of the New Structures .....	88
6.2.1 The Potential Distributions .....	88
6.2.2 The NMR Frequencies.....	91
6.2.3 The Effect of Adjacent Qubits .....	96
6.3 Summary .....	98
<b>Chapter 7. Conclusions and Future Works.....</b>	<b>100</b>
7.1 Conclusions .....	101
7.2 Future Works.....	102
7.2.1 More Efficient A-gate Structures.....	102
7.2.2 Different Materials for Insulating Layer.....	103
7.2.3 Multi-Qubit Structures and Exchange Gates .....	103
7.2.4 Further Study on Perturbation Theory and Other Alternative Theories to Find the Wavefunction of the Donor Electron.....	104
7.2.5 Further Study on Determinant Factors Affecting the Wavefunction of the Donor Electron.....	105
<b>Bibliography .....</b>	<b>106</b>
<b>Appendix I .....</b>	<b>111</b>
<b>Appendix II.....</b>	<b>115</b>

## Summary

Since Kane's proposal in 1998, many researchers have been investigating the different factors that affect the performance of a quantum bit (qubit). An important step in analyzing the Kane's system is to model the dependency of nuclear magnetic resonance (NMR) frequency on the external voltage applied via metallic gates called A-gates. To establish this relation, we carry out a second order perturbation theory, including higher order terms up to 3d states. Another requirement in constructing the relation between the applied voltage and the NMR frequency is to accurately obtain the potential distribution inside the silicon substrate. In many previous studies, an analytical approach has been used which is only applicable to ideal structures of metallic gates. To design a quantum bit with an arbitrary gate structure, we use an electromagnetic simulation method to calculate the potential inside the substrate. Two new A-gate structures are proposed and investigated rigorously by a numerical simulation method. The first one is called the coplanar A-gate structure which has the advantage of easy fabrication, but it offers only a relatively weak voltage control over the nuclear magnetic resonance (NMR) frequency of the donor atom. However, this shortcoming can be overcome by doping the donor closer to the substrate interface. The split-ground A-gate structure, on the other hand, produces a similar potential distribution as that of the original Kane's A-gate structure and provides a relatively stronger control over the NMR frequency of the donor atom. Both structures have the advantage of allowing device integration or heterostructure fabrication from below the silicon substrate.



## List of Tables

**Table 1.1.** Some of the nuclei more commonly used in NMR Spectroscopy with the details of their unpaired protons, unpaired neutrons, net spin and gyromagnetic ratio. ....22

**Table I.1.** Electron wavefunctions of a donor phosphorus atom in a silicon host.....111

**Table I.2.** Electron energy levels of a donor phosphorus atom in a silicon host.....114

## List of Figures

<b>Figure 1.1.</b> Block sphere representation in which the qubit state is shown as a point on the unit three-dimensional sphere (block sphere).....	6
<b>Figure 1.2.</b> Kane's qubit: The implementation for a solid-state quantum computer based on nuclear spin of the donor atom in silicon. Reproduced from Kane <sup>9</sup> .....	11
<b>Figure 1.3.</b> The nuclear Zeeman levels of a spin-1/2 nucleus as a function of the applied magnetic field.....	17
<b>Figure 1.4.</b> Spin precession under the effect of a magnetic field.....	21
<b>Figure 1.5.</b> The energy required to cause the spin-flip, $\Delta E$ , depends on the magnetic field strength at the nucleus.....	23
<b>Figure 1.6.</b> The process of driving the addressed qubit (marked in red) into resonance with the RF field. $V_0$ is applied on the A-gate of the qubit and other qubits are left unexcited.....	25
<b>Figure 3.1.</b> Two orthogonal mesh systems. the primary grid $G$ is used for allocating electric grid voltages and magnetic side wall fluxes represented by $e$ and $b$ respectively. The dual grid $G \sim$ (represented by tilde) is used for the dielectric side wall fluxes $d$ and magnetic grid voltages $h$ . This image is reproduced from CST advanced topics Manual <sup>83</sup> .....	55
<b>Figure 3.2.</b> For Faraday's Law, the closed integral on the left hand side of the equation can be replaced by the sum total of four grid voltages. The matrix representation of the Faraday's law is shown. This image is reproduced from CST advanced topics Manual <sup>83</sup> .....	56
<b>Figure 3.3.</b> the electric voltages and magnetic fluxes assigned to facets and edges of a tetrahedral mesh cell. This image is reproduced from CST advanced topics Manual <sup>83</sup> .....	59
<b>Figure 3.4.</b> Comparison of the calculated normalized capacitance for a square section of a microstrip line obtained using CST and Itoh et al. the square plate has a side length of $W$ , and $b$ is the separation between the plates. The comparison has been carried out for two values of relative permittivity, $\epsilon_r = 9.6$ and $\epsilon_r = 1$ .....	60
<b>Figure 3.5.</b> The comparison of potential data obtained from CST and COMSOL simulations. Potentials are obtained along a line drawn from A-gate lead down to the ground plane. A static voltage of 5 V is applied on the A-gate lead. For Kane's A-gate structure, the dimensions are: substrate thickness=100 nm, A-gate lead width=7 nm, insulating layer ( $\text{Si}_{0.5}\text{Ge}_{0.5}$ ) thickness=5 nm. The dielectric constant $\epsilon_r$ of Si is 11.46 and that of SiGe is 13.95.....	61
<b>Figure 4.1.</b> The single qubit structure of the silicon-based solid-state quantum computer proposed by Kane. ....	65

**Figure 4.2.** The nonlinear potential distribution inside the silicon substrate of the qubit structure shown in Fig. 4.1 with  $s = 5$  nm,  $b = 100$  nm,  $W = 7$  nm,  $\epsilon_r$  of silicon = 11.46, and  $\epsilon_r$  of silicon dioxide = 3.9. ....69

**Figure 4.3.** The perturbation energy with respect to the change in the A gate voltage. The phosphorus atom is at  $x = 20$  nm,  $y = 0$ , and  $z = 50$  nm. The other parameters are:  $s = 5$  nm,  $b = 100$  nm,  $W = 7$  nm,  $\epsilon_r$  of silicon = 11.46, and  $\epsilon_r$  of silicon dioxide = 3.9. ....70

**Figure 4.4.** The potential distributions along the  $z$  direction at  $x = 20$  nm and  $y = 0$  inside an A gate structure with different insulator barrier materials. The dimensions of the A gate are:  $s = 5$  nm,  $b = 100$  nm,  $W = 7$  nm, and  $\epsilon_r$  of silicon = 11.46. For the  $\text{SiO}_2$  insulation barrier,  $\epsilon_r = 3.9$ . For the SiGe insulation barrier,  $\epsilon_r = 13.95$ . ....72

**Figure 5.1.** The implementation for a solid-state quantum computer using phosphorus (31P) donor electron as the qubit. ....76

**Figure 5.2.** The tunable bandwidth  $f_w$  and the electron-spin magnetic resonance frequency  $f_0$  with the static magnetic flux strength  $B$ . The dimensions of the A gate are  $s = 5$  nm,  $b = 100$  nm,  $W = 7$  nm,  $\epsilon_r$  of silicon = 11.46, and  $\epsilon_r$  of silicon dioxide = 3.9. phosphorus atom is at  $x = 20$  nm,  $y = 0$ , and  $z = 50$  nm. ....78

**Figure 6.1.** The proposed coplanar A-gate structures for the realization of the semiconductor quantum computer based on the nuclear spin of a phosphorus atom doped inside a silicon substrate, (a) the basic structure, (b) & (c) two possible variants. ....85

**Figure 6.2.** The proposed split-ground A-gate structures, (a) the basic structure, (b) & (c) two possible variants. ....86

**Figure 6.3.** A typical 2D potential distribution of the coplanar A-gate structure shown in Fig. 6.1(a). ....87

**Figure 6.4.** The variation of the potential for the coplanar A-gate structure in Fig. 6.1(a) along a line drawn from A-gate lead down to the silicon substrate with  $x=40$  nm,  $y=0$ , and  $z=0 \sim -105$  nm. A static voltage of 5 V is applied on the A-gate lead. The result is compared with that obtained with Kane's A-gate. The dimensions of the A-gate structure are:  $b=600$  nm,  $s=5$  nm,  $w=7$  nm,  $L_G=L_A=70$  nm, and  $L_s=10$  nm. The dielectric constant  $\epsilon_r$  of Si is 11.46 and that of SiGe is 13.95. For Kane's A-gate structure, the dimensions are: substrate thickness=100 nm, A-gate lead width=7 nm, insulating layer ( $\text{Si}_{0.5}\text{Ge}_{0.5}$ ) thickness=5 nm. ....89

**Figure 6.5.** The variation of the potential for the split-ground A-gate structure in Fig. 6.2(a). (a) The 1D variation along a line drawn from A-gate lead down to the silicon substrate with  $x = 40$  nm,  $y = 0$ , and  $z = 0 \sim -105$  nm and for different A-gate lead widths  $W_p$ , and (b) the 2D distribution of the electric field on a vertical cross section cut at  $x=40$  nm and for the case of  $W_p=60$  nm. The results are compared with that obtained with Kane's A-gate. The

dimensions of the split-ground A-gate structure are:  $b_1=100$  nm,  $s=5$  nm,  $L=100$  nm,  $w=7$  nm,  $L_p=40$  nm,  $W_s=100$  nm,  $W_G=25$  nm, and  $b_2=150$  nm. The dimensions of Kane's A-gate are same as those in Fig. 6.4. .... 90

**Figure 6.6.** The variations of the NMR frequency with applied A-gate voltage for the three different A-gate structures with a uniform static magnetic field of 2T along the z direction. The dimensions of the coplanar A-gate structure, the split-ground A-gate structure, and Kane's A-gate structure are same as those in Figs. 6.4 and 6.5. For the coplanar A-gate structure, two donor positions are shown (at  $z=-35$  nm and  $-55$  nm). For the split-ground A-gate structure, results for two A-gate widths are shown ( $W_p=7$  nm and 40 nm). .... 92

**Figure 6.7.** The variations of the NMR frequency with applied voltage for the split-ground A-gate structure with a uniform static magnetic field of 2T along the z direction, (a) for different substrate heights,  $b_1$ , above the ground, (c) for different widths,  $W_p$ , of A-gate lead, and (c) for different substrate widths,  $W_s$ . The dimensions of the split-ground A-gate structure are same as those in Fig. 6.5 except the ones being varied. Donor position is at  $z=-55$  nm. .... 94

**Figure 6.8.** The 2D potential profiles for three A-gate structures with two end gates being excited, (a) Kane's A-gate structure, and (b) the split-ground A-gate structure. The separation between adjacent phosphorus donors (31P) are  $D=100$  nm for both cases, and the donors are at a distance of 50 nm from the A-gate leads. The dimensions for the split-ground A-gate structure are:  $b_1=100$  nm,  $b_2=100$  nm,  $W=7$  nm,  $s=5$  nm,  $W_p=40$  nm,  $W_s=80$  nm,  $W_G=20$  nm, and  $L=100$  nm. The dimensions for Kane's A-gate structure are same as those in FIG. 6.4. .... 96

## List of Symbols

$Qubit$	Quantum Bit
$ \psi\rangle$	State wavefunction of a quantum bit shown in Dirac notation
$ 0\rangle,  1\rangle$	Basis states of the vector space encompassing the state of the qubit
$H$	Hamiltonian Operator
$\mu_B$	Bohr Magnetron
$g_n$	Nuclear g-factor
$\mu_n$	Nuclear Magnetron
$B$	Static Magnetic Field
$\sigma, \sigma_z^e, \sigma_z^n$	Pauli Spin Matrices
$B_{ac}$	RF Magnetic field
$Si$	Silicon
$P$	Phosphorus
$A, A_h$	Hyperfine Interaction Constant
$\Psi(r)$	Electron Wavefunction
$ \Psi(0) ^2$	Probability Density of the Electron Wavefunction,
$I_z, m$	Spin Quantum Number Operator and Spin Quantum Number
$L, L_z$	Angular Momentum Operator
$\hbar, h$	Planck Constant
$\mu$	Magnetic Moment, Permeability

$T$	Torque
$E$	Energy
$\gamma$	Gyromagnetic Ratio
$\nu_L, \omega_L$	Larmor (angular) Frequency
$M$	Magnetization
$H_0$	Unperturbed Hamiltonian
$H'$	Perturbation Hamiltonian
$\psi_n$	Eigenfunction of the Hamiltonian
$E_n$	Eigenvalues of the Hamiltonian
$\delta_{ij}$	Kronecker delta function
$\Psi'_{A_1}$	Perturbed Wavefunction for the Ground State
<i>NMR</i>	Nuclear Magnetic Resonance
<i>QIP</i>	Quantum Information Processing
<i>EMT</i>	Effective Mass Theory
<i>1s, 2s, 2p, 3s, 3p, 3d</i>	Hydrogenic Quantum States
<i>Norm, N(<math>\lambda</math>)</i>	Normalization Constant
$\Psi^{(1)}$	First Order Perturbation Correction Wavefunction
$\Psi^{(2)}$	Second Order Perturbation Correction Wavefunction
$V, V(\mathbf{r})$	Electric Potential
$\epsilon$	Permittivity
$Q$	Electric Charge
$G$	Green's Function
$\tilde{G}$	Spectral Domain Green's Function
DFT	Density Functional Theory

$e$	Electron Charge
$f$	Nuclear/Electron Magnetic Resonance Frequency
$g_E$	$g$ -factor of the Donor Electron
$f_w$	The Tunable Bandwidth
$F$	Hydrogenic Wavefunctions
$a$	Bohr Radius

# **Chapter 1**

## **Introduction**



## **1.1 Quantum Computation: Introduction and History**

Quantum computation and quantum information is the utilization of quantum mechanical systems for information processing purposes<sup>1</sup>. Since 1970s, the effort of obtaining a better control over the behavior of single quantum mechanical systems has been an important historical milestone which made a significant contribution to the development of quantum computation and quantum information. Before 1970s, this so called “control” was limited only to a bulk sample, ignoring all the microscopic phenomena involved in the large number of quantum mechanical systems contained in the sample. Although it was possible to gain some access to every single quantum mechanical system through devices such as “particle accelerators”, the control over the individual elements was still very limited. Since then, many methods have been developed to enable us in manipulating single quantum systems. For example, trapping a single atom in an “atom trap” makes it isolated from the surrounding world and allows us to investigate different behavior of its quantum mechanical state with high accuracy. Another technique that has been developed for controlling individual quantum systems is the “scanning tunneling microscope” by which we are able to move single atoms around to fabricate arbitrary structures. Also, Electronic devices such as Single Electron Transistors <sup>2</sup> have been fabricated whose operational currents involve the transfer of only single electrons.

Computer Science, in its modern format, experienced a magnificent breakthrough when the great mathematician “Alan Turing” published his remarkable paper in 1936 <sup>3</sup>. He introduced a mathematical platform of all the

machines which today we call “programmable computers”. This model of computation is called “Turing Machine” in his honor.

It was not long after Turing’s paper, that first computers were developed and fabricated using electronic devices and components. All the electronic components constituting the Computer hardware has been growing at an amazing speed. This trend has been analyzed by “Gordon Moore” which has come to be known as Moore’s law <sup>4</sup> simply stating that roughly once every two years the computer power will double for constant cost.

Moore’s Law has predicted this trend approximately true since 1960s. However, this amazing fit between the Moore’s law and industry was predicted to end sometime maybe as soon as the first two decades of the twenty first century. The main reason for this future mismatch is the belief that conventional methods in fabrication of computer components are facing serious issues against significant reduction in size of the samples. This is because of the emergence and interference of quantum effects as the electronic devices are made smaller and smaller.

Moving from the conventional computing paradigm to a new one can be considered one of the possible solutions to the above-mentioned problem. This new paradigm is based on the rules of quantum physics instead of the classical physics which was previously used in classical computation methods. It’s been shown that although a classical computer is capable of simulating a quantum computer, it is unable to conduct this simulation in an efficient way. In other words, quantum computers provide us with a significant speed advantage over their classical counterparts. This advantage is caused intrinsically by classical computation not the state of advances in the current technologies and that’s

why many researchers in this field believe that even in the future, classical computation won't be able to reach this level of speed and power.

As an example, in 1992, Deutsch<sup>5</sup> defined a computational device for efficient simulation of an arbitrary physical system. As we know the ultimate laws which govern the nature are quantum mechanical, therefore Deutsch believed that this computational device should be based on principles of quantum mechanics. These new devices, the quantum version of all the Turing machines used in the past 50 years, resulted in the modern idea of a quantum computer.

The article published by Deutsch<sup>5</sup> was an important step in transition from classical to quantum computation. A decade later, his idea was even more improved by many people such as Peter Shor who, in 1994, demonstrated two significant problems<sup>6</sup>: the problem of finding the prime factors of an integer and "discrete logarithm" problem which can be solved efficiently on a quantum computer. This dramatic discovery, led to the extensive interest in quantum computers since it is believed that these two problems have no efficient solution on a classical computer.

## **1.2 Quantum Bit**

“Bit” is the fundamental constituent concept in classical computation and classical information. In a same manner, in Quantum computation and quantum information, this basic concept is called quantum bit or “qubit”. Just like the classical bit which has a state (either 0 or 1), a qubit also has a state. Two possible states for a qubit are represented by  $|0\rangle$  and  $|1\rangle$  and are the analogue versions of the states 0 and 1 in a classical bit. The main difference between a classical bit and a qubit is that the latter can be in a state which is

neither  $|0\rangle$  nor  $|1\rangle$ . In other words, the state of a qubit can be linear superposition of states:

$$|\psi\rangle = \alpha|0\rangle + \beta|1\rangle \quad (1.1)$$

In which the numbers  $\alpha$  and  $\beta$  are complex numbers. In other words, considering the  $|0\rangle$  and  $|1\rangle$  states as the orthogonal basis states of a two-dimensional complex vector space, an arbitrary state of a qubit is a vector in this space.

A classical bit is like a coin; either heads or tails up. By contrast, a qubit can have a state between  $|0\rangle$  and  $|1\rangle$ . It should be emphasized that this is true only before the state of a qubit is observed. Put in another way, When we measure a qubit we get either the result 0, with probability  $|\alpha|^2$ , or the result 1, with probability  $|\beta|^2$ . Basically,  $|\alpha|^2 + |\beta|^2 = 1$ , since the probabilities must add up to one. Considering the qubit in a geometrical representation, we can interpret this by the normalization of the qubit's state to length 1. Therefore, in general a qubit's state is a unit vector in a two-dimensional complex vector space.

Since  $|\alpha|^2 + |\beta|^2 = 1$ , we can rewrite equation (1.1) as:

$$|\psi\rangle = \cos\frac{\theta}{2}|0\rangle + e^{i\varphi}\sin\frac{\theta}{2}|1\rangle \quad (1.2)$$

Where  $\theta$  and  $\varphi$  are real numbers. This equation lead us to “block sphere representation” in which  $\theta$  and  $\varphi$  define a point on the unit three-dimensional sphere also called as the “block sphere”. This sphere is shown in Fig. 1.1.

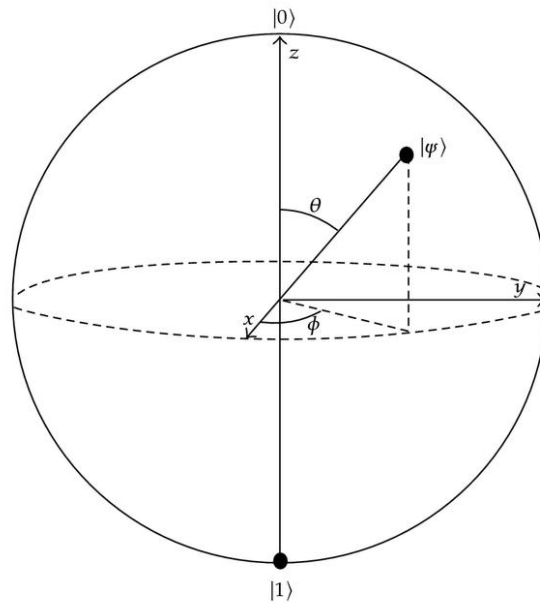


Figure 1.1. Bloch sphere representation in which the qubit state is shown as a point on the unit three-dimensional sphere (Bloch sphere).

This representation has been shown as a useful method for geometrical visualization of a qubit's state. Many different physical systems can be used to realize qubits such as the two different polarizations of a photon; the different alignments of a nuclear spin in a uniform magnetic field; and two states of an electron orbiting a single atom.

### 1.2.1 Silicon Qubits

In the past 50 years, silicon technology has been the principal cause for the fast growing advances in the field of microelectronics. Even after almost half a century of progress and development in this technology and using many new materials, silicon is still the main ingredient for fabricating classical computation devices. Besides, considering the paradigm shift from classical to

quantum computation discussed in the previous section, silicon is believed to be capable of playing an equally dominant role as the host material for this new generation of devices. These new structures incorporate the quantum properties of charges and spins. Quantum computers and spintronic devices are two major examples of this new category.

The importance of silicon in these quantum applications is due to its weak spin-orbit coupling and the existence of isotopes with zero nuclear spin<sup>7</sup>. Also, magnificent progress in silicon technology since the development of classical computers has been another reason that makes silicon an ideal host for quantum mechanical-based devices. These factors, as well as the ability of quantum spin control, have attracted a vast interest in silicon-based quantum devices during the past years.

Although there have been many realization methods for quantum information processing systems<sup>2,8</sup>, semiconductor-based quantum computers has attracted more interests due to their shared features with classical computers and classical electronics technology<sup>9,10</sup>. Since the study by Loss and DiVincenzo<sup>10</sup> in 1998, electron spins in quantum dots have received a significant attention which has led to considerable experimental and fabrication progress. Quantum dots in GaAs/AlGaAs heterostructures has been realized lithographically and experiments have shown different stages in the working cycle of a quantum computer, namely qubit initialization, single-shot single electron spin readout<sup>11</sup>, and coherent control of single-spin<sup>12</sup> and two-spin<sup>13</sup> states. The concept of coherence plays a central role in realization of quantum computers, since quantum computations tasks can only be carried out in perfectly isolated systems. In other words, any uncontrolled interference from the surroundings

cause the system to enter the decoherence stage in which the quantum algorithms cannot be precise and trustworthy<sup>9</sup>. One of the major drawbacks of using Al- GaAs/GaAs heterostructures is the intrinsic nuclear spins existing in the host material which ultimately result in short coherence and spin-relaxation times. This is due to great interaction of host material spin with electron spins leading to uncontrolled behavior of the system. Therefore, using proper isotopes of silicon makes it possible to increase this coherent time by removing the magnetic nuclei from the host material. Natural silicon consists of 95% non-magnetic nuclei (92%  $^{28}\text{Si}$  and 3%  $^{30}\text{Si}$ ). Purification processes can be utilized to obtain almost zero nuclear spin isotopes. There have been many studies considering the qubits based on electron spins embedded in donors<sup>14-17</sup> doped inside Si and quantum dots<sup>18</sup> in Si. In order to realize a spin quantum bit, whether we use a quantum dot or a donor, we have to find a way to confine single electrons. This process is quite challenging. Compared to the significant advances in the technology of classical field effect transistors (FETs), silicon quantum dots haven't experienced as much progress mainly because of the high impact of epitaxial growth in lattice matched III-V materials on GaAs systems<sup>7</sup>. Many studies have investigated the controllability of individual spins and charges inside silicon single or double quantum dots and reported different quantum behaviors such as coulomb blockade, Pauli spin blockade and Rabi oscillations. Since in this dissertation we consider only the dopant quantum bits, we suffice to refer the reader to few works which have been done in the field of quantum dot systems<sup>19-29</sup>. Considering the dopants in silicon, a study by Fuechsle et al. investigated the valley excited states<sup>30</sup>. As mentioned above, the confinement of an electron is

an essential condition for realization of a qubit. Lansbergen et al<sup>31</sup> achieved this confinement using external gates and by analyzing the transport spectra of donor atoms. Eventually we should mention about the studies on the fabrication of single atom transistor<sup>32</sup> and single-shot read out<sup>33</sup> relating to the embedded spin of phosphorus inside the silicon host. Considering the above-mentioned results and investigations carried out during the past decade, potentiality of silicon as a key material in quantum computation systems is more evident.

Although the priceless experiences of CMOS technology for several decades has eased the quantum bit fabrication in many stages<sup>34</sup>, the significance of current classical computer technology must not be overrated, as the issues existing in the process of integrated circuits design sometimes are entirely different when it comes to quantum bits and their scalability. For instance, usage of interfaces in classical ICs and transistors serves as a means of manipulating the threshold voltages while in quantum bit system, this interface can play a determinant role in the coherent time of the spin<sup>7</sup>.

Before moving to the discussion on the main subject of this dissertation, donor-based spin qubits, it is worth mentioning that despite all the advantages of silicon as the platform for realization of quantum bit systems such as non-magnetic isotopes and negligible spin-orbit coupling, there are also some shortcomings in the general understanding of Silicon. To name a few, we can mention about the effective mass and lattice constant of silicon and presence of multi-valley conduction band. During the past years, there have been a lot of investigations to grasp the new physics of these issues to facilitate the understanding of future silicon-based quantum systems.



### 1.2.2 Donor-based Spin Qubits

Spin qubits linked with donor atom doped inside silicon are considered an ideal choice. This is due to the fact that electron and nucleus spins at the donor site experience a great level of coherence in temperatures below 4K since they are highly isolated from the surrounding silicon atoms<sup>35</sup>. The only remaining task is to construct a suitable and efficient method to manage the interactions of individual spins. These interactions can be of two major types: spin-spin interaction and interaction of spins with external agents such as electric fields. The general picture of incorporating donor atoms as a means of realization of qubits, is to find a way to harness the donor's electron cloud distribution (electron wavefunction) using the external voltages and control the spins behaviors by exposing the qubit to externally applied magnetic fields. Whether we base the qubit states on the electron spin or nuclear spin, a common yet vital step in almost all the spin-based qubit proposals is the ability to control the wave function of the donor electron. This ability makes it possible to construct single-qubit and double-qubit quantum logic gates.

The original idea was proposed by Kane in which he introduced a quantum bit based on nuclear spin of the donor atom in silicon<sup>9</sup>. The original qubit structure proposed by Kane for realization of a quantum bit in a silicon host is shown in Fig. 1.2. It is a phosphorus atom (isotope <sup>31</sup>P) doped in a silicon substrate (isotope <sup>28</sup>Si). On top of the silicon substrate is an insulating layer of silicon dioxide. At the bottom of the silicon substrate is a metallic layer served as the ground, called the back gate. On top of the silicon dioxide layer there are two types of metallic strip, called the A-gate which controls the electron

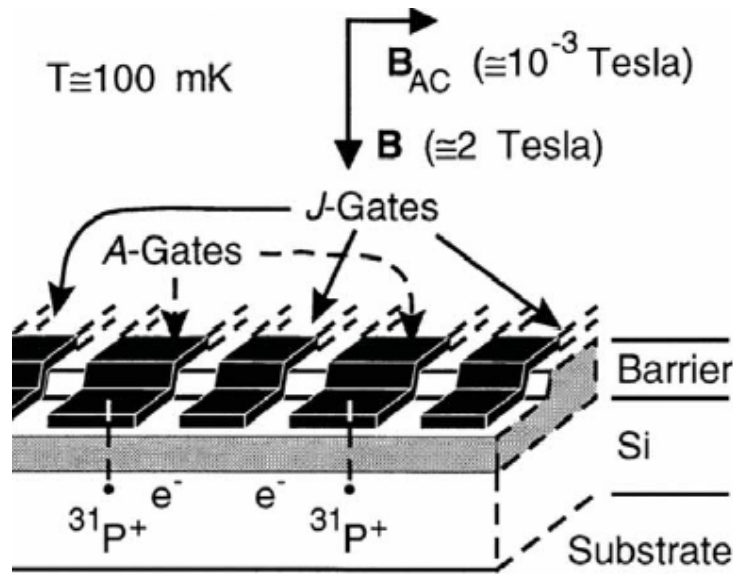


Figure 1.2. Kane's qubit: The implementation for a solid-state quantum computer based on nuclear spin of the donor atom in silicon. Reproduced from Kane<sup>9</sup>.

wavefunction and J-gate which control the exchange interactions. The concept of exchange interaction and J-gates are beyond the scope of this dissertation.

Determined by the orientation of the applied electric field (positive or negative gate voltage), the electron cloud is either pulled toward the A-gate or is pushed away from it. In either case, the electron cloud of the phosphorus atom can be drifted by applying a voltage on the A-gate. The drift of the electron cloud can change the hyperfine interaction between the phosphorus nucleus and the outermost valence electron and hence change the Nuclear Magnetic Resonance (NMR) frequency of phosphorus. The control over the hyperfine interaction enables us to tune a particular donor into resonance with an externally applied oscillating magnetic field. Regarding a quantum system formed by donor nucleus and donor electron, we can write the spin qubit Hamiltonian when there is an excitation source driving the electric field through the A-gate<sup>9,36</sup>:

$$|H_{en}\rangle = \mu_B B \sigma_z^e - g_n \mu_n B \sigma_z^n + A \sigma^e \cdot \sigma^n \quad (1.3)$$

where  $\mu_B$  is the Bohr magneton,  $g_n$  is the nuclear g-factor, and  $\mu_n$  is the nuclear magneton. B is the static magnetic field which in this case is assumed to be along the z direction.  $\sigma$  are the Pauli spin matrices (with eigenvalues equal to +1 and -1).

The contact hyperfine interaction constant (A) appearing in the above equation can be obtained if information about the electron wavefunction is provided. In other words, by applying an external voltage through A-gate, it is possible to drift the electron cloud, thus changing the electron wavefunction at the donor site which results in the alteration of hyperfine interaction constant based on the equation 1.4:

$$A = \frac{8}{3} \pi \mu_B g_n \mu_n |\Psi(0)|^2 \quad (1.4)$$

$|\Psi(0)|^2$  is the probability density of the electron wavefunction, estimated at the donor nucleus site.

Estimating the effect of A-gate external voltage on the hyperfine interaction has been the subject of many studies right after Kane made his proposal in 1998. In order to evaluate the hyperfine interaction constant as a function of the gate electric potential, as equation 1.4 suggests, first it is required to obtain the extent of displacement in the electron distribution caused by the interfering external voltage. Then, we are able to estimate the electron wavefunction at

the nucleus center. Besides the effect of electric field, it is worth noting that contact hyperfine interaction is highly affected by some other important factors such as the depth at which the donor atom has been doped.

Since Kane, many approaches have been used to find a reliable relationship between hyperfine interaction constant and A-gate voltage. Using hydrogenic-like wavefunctions merely weighted by silicon dielectric constant was among the first methods that have been used to build this relationship. Larinov et al.<sup>37</sup> adopted an analytical approach for obtaining the A-gate potential which means that it is only applicable to ideal structures of A gates (an ideal circular plate). Then perturbation theory was used to calculate the effect of gate voltage in changing the hyperfine interaction constant. Using the same method of hydrogenic orbitals (scaled for silicon), Wellard et al.<sup>38</sup> proposed a commercial software to solve the Poisson equation and obtain the potential distribution inside the structure caused by the external voltage. This method provided more realistic results for the electric potential inside the substrate. Instead of using perturbation theory, they used an extensive set of hydrogenic orbitals basis to expand the electron wavefunction and used diagonalization to numerically solve the Hamiltonian. Later, a modification to this method was proposed by utilizing the non-isotropic orbital basis states<sup>39</sup>. As well as using group theory to describe the degeneracy of valley states, two studies<sup>40-42</sup> also used perturbation theory to find the splitting in spectral lines of energy levels also known as Stark shift. In order to evaluate the Stark shift and/or hyperfine behaviors relating to the donor electron, other methods such as tight-binding have been used<sup>43,44</sup>. These studies also provide some information about the details of the Bloch structures.

Furthermore, some techniques such as combined variational method<sup>45,46</sup> and Gaussian expansion of the envelope function in EMT<sup>47</sup> have been used to further develop the effective mass treatment. Later, the direct diagonalization in K space (momentum domain) was employed<sup>48</sup> to include the direct effect of the A-gate potential in the system Hamiltonian. This method was able to provide the same picture as the seminal tight-binding method of Martins et al<sup>44</sup> which showed the dependency of contact hyperfine interaction stark shift on the external applied electric field strength and also the depth of the donor site. At low fields, the k-space diagonalization scheme can be useful in the consistency check process for calculating the contact hyperfine interaction stark shift using real-space tight-binding method<sup>49</sup>. Also, it can be used for evaluation of theoretical convergence to a certain level in comparison with experiment<sup>50</sup>. One should note that despite all the advantages mentioned above, this method has not been computationally optimized<sup>7</sup>. Basically, the precise behavior and details of the hyperfine interaction at the nucleus site is not obtained by these descriptions. In fact, only the relative change of hyperfine interaction due to the external variation of the gate voltage is calculated and precise details about the contact hyperfine interaction can be studied in ab-initio theories<sup>51,52</sup>. Because of the recent advances in experimental measurement, many researchers have investigated the dependence of orbital wavefunction and electron quantum states on the location of the donor atom below the interface<sup>53-55</sup>. In an article by Lansbergen et al., tight-binding method was applied to an electron mediated donor system to evaluate the effect of donor depth and external voltage on the quality of

quantum confinement. This method was able to give an excellent picture of the lower lying donor states<sup>31</sup>.

Thanks to extensive studies in theoretical and engineering description of donor electron inside the device, we have a substantial knowledge on the wavefunction behavior of donor based systems. The original Kane's article helped to modify many theoretical aspects of donor wavefunction including: local electric contacts and non-isotropic hyperfine interaction relations<sup>56,57</sup> for calculating the effect of electric fields on wavefunction mapping<sup>58</sup>, the effect of external magnetic fields and the effect of metallic gate in controlling the g-factor<sup>59,60</sup>, molecular donor-based structures and their dynamics<sup>61-64</sup>, analysis of cross-talk interference in hyperfine interaction control<sup>65</sup>, designing continuous chain of ionized donors to develop a path for coherent single electron transport<sup>59</sup>, read-out mechanisms such as spin-to-charge technique<sup>61,66</sup>, and finally the estimation of donor energy states under the effect of supplementary nanostructures to modify the net potential distribution inside a single atom transistor<sup>30</sup>.

### **1.3 Nuclear Magnetic Resonance (NMR)**

In 1896, Pieter Zeeman discovered that the optical spectral lines are split when exposed to an electromagnetic field<sup>67</sup>. Therefore, the splitting of energy levels due to an applied external magnetic field is called "Zeeman effect". This effect causes magnetic resonances which lie in the radio frequency range. In other words, two branches (or eigenvalues) of a particular energy level will split in an external magnetic field and the energy difference between these two states is measured in megahertz or gigahertz<sup>68</sup>.

Around half a century later and shortly after the discovery of the electron

paramagnetic resonance by Jevgeni Konstantinovitch Savoiski, two groups simultaneously demonstrated the existence of nuclear magnetic resonance (NMR) which sometimes is called nuclear induction or paramagnetic nuclear resonance<sup>69</sup>.

### 1.3.1 The Nuclear Resonance Effect

Subatomic particles such as protons, electrons and neutrons are associated with a purely quantum mechanical concept called “spin”<sup>70</sup>. The overall effect of spins in protons and neutrons form the spin of different nuclei. Here we adopt the formulation provided by Freude<sup>68</sup>. The nuclear spin quantum number is represented by  $I$ . Spin angular momentum has an absolute value of:

$$|L| = \hbar\sqrt{I(I+1)} \quad (1.5)$$

when an external magnetic field is applied, the component of spin angular momentum in the direction of the field is:

$$L_z = I_z\hbar \equiv m\hbar \quad (1.6)$$

A nuclear state with spin  $I$  is said to be  $(2I+1)$ -fold degenerate. It means that a nucleus of spin  $I$  will have  $2I+1$  possible orientations. Since the external field is usually along the  $z$  direction, the magnetic quantum number is represented by  $I_z$  or  $m$  and therefore can have  $2I+1$  values:

$$I_z \equiv m = -I, -I+1, \dots, I-1, I \quad (1.7)$$

In the most important case for NMR, which is  $I=1/2$ , nucleus will have 2 possible cases. In the absence of a magnetic field these states have same energy levels (degenerate states). However, applying a magnetic field will break this degeneracy. This splitting between nuclear spin levels is called Nuclear Zeeman Splitting. Fig. 1.3 sketches the nuclear Zeeman levels of a spin-1/2 nucleus as a function of the applied magnetic field.

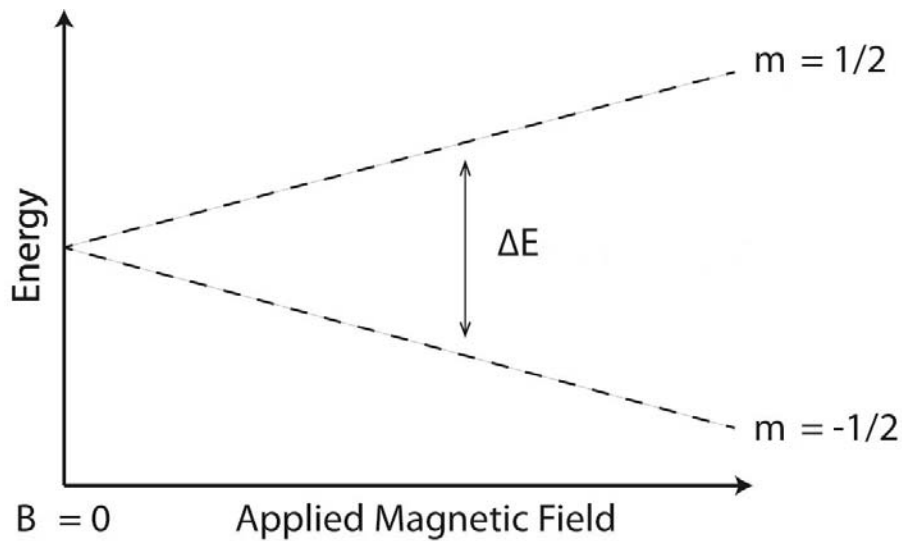


Figure 1.3. The nuclear Zeeman levels of a spin-1/2 nucleus as a function of the applied magnetic field

The concept of magnetic moment can be described as follows: atomic nucleus carries electric charge and because of the spin angular rotation, a circular current is created. This circular current creates a magnetic moment  $\mu$ . Applying an external magnetic field (B) results in a torque:

$$T = \mu \times B \quad (1.8)$$

And the energy of this magnetic moment is:



$$E = -\mu \cdot B \quad (1.9)$$

In order to relate the magnetic moment to the spin angular momentum, the gyromagnetic ratio  $\gamma$  is introduced. Gyration is the rotation of an electrically charged particle. The gyromagnetic ratio  $\gamma$  is defined by:

$$\mu = \gamma L \quad (1.10)$$

As mentioned before we are interested in the z component of the nuclear magnetic moment. Thus,

$$\mu_z = \gamma L_z = \gamma I_z \hbar \equiv \gamma m \hbar \quad (1.11)$$

The splitting of an energy level of a nucleus with nuclear spin quantum number of I and under the effect of an external magnetic field along the z-direction  $B_0$  is associated with  $2I+1$  Zeeman levels. The energy difference between two cases with and without the magnetic field is:

$$E_m = -\mu_z B_0 = -\gamma m \hbar B_0 \quad (1.12)$$

For the special case that we are interested in, when  $I=1/2$ ,  $m = \pm 1/2$ , we have two Zeeman levels with an energy difference of:

$$\Delta E_{-\frac{1}{2}, \frac{1}{2}} = \gamma \hbar B_0 = \hbar \omega_L = h \nu_L \quad (1.13)$$

Instead of dealing with energy difference between two levels, in the above equation, the Larmor frequency has been introduced. Joseph Larmor in 1897,

used this resonance frequency to describe the precession of orbital magnetization when influenced by an external magnetic field. To have a better insight of the Larmor frequency  $\nu_L$  (or Larmor angular frequency  $\omega_L$ ) we can use a classical model: considering the magnetic dipole, we can define the torque as the derivative of the angular momentum with respect to time. Following along with equation (1.10) we have:

$$\mathbf{T} = \frac{d\mathbf{L}}{dt} = \frac{1}{\gamma} \frac{d\boldsymbol{\mu}}{dt} \quad (1.14)$$

Afer some manipulation and using eq. (1.8),  $\mathbf{T} = \boldsymbol{\mu} \times \mathbf{B}$ ,

$$\frac{d\boldsymbol{\mu}}{dt} = \gamma \boldsymbol{\mu} \times \mathbf{B} \quad (1.15)$$

Magnetization is the overall effect of all the nuclear dipoles in the unit volume. Basically the magnetization is not aligned with the external magnetic field, thus we must solve the motion equation:

$$\frac{d\mathbf{M}}{dt} = \gamma \mathbf{M} \times \mathbf{B} \quad (1.16)$$

as assumed before, we consider the magnetic field to be in the z-direction ( $\mathbf{B} = B_0 \hat{z}$ ). We also assume that the initial conditions for the magnetization are defined as  $\mathbf{M}(t = 0) = |\mathbf{M}|(\sin \alpha, 0, \cos \alpha)$ . Finally the solutions to the motion equation are:

$$M_x = |\mathbf{M}| \sin \alpha \cos \omega_L t \quad (1.17)$$

$$M_y = |M| \sin \alpha \sin \omega_L t$$

$$M_z = |M| \cos \alpha$$

in which  $\omega_L = \gamma B_0$ . Depending on the negative or positive value of the gyromagnetic ratio, gamma, the rotation vector is either in the same direction or the opposite direction of the magnetic field  $B_0$ . Relating the magnetic field to the resonant frequency, Larmor relation is the most important equation of the NMR theory and commonly the negative sign is omitted to form an equation of magnitudes.

$$\nu_L = \frac{\gamma}{2\pi} B_0 \quad (1.18)$$

The frequency of precession is the Larmor frequency which is same as the transition frequency between two spin states. Thus, If a nucleus of  $I=1/2$  is excited by an energy package equal to the transition energy, the state of the nucleus will change which is equivalent to flipping the spin. For this to happen, a RF magnetic field is used. Flipping the spin of the nucleus under the applied RF magnetic field is called Nuclear Magnetic Resonance (NMR) and the frequency required for this resonance to happen is called NMR frequency. Fig. 1.4 shows the spin precession under the effect of a magnetic field.

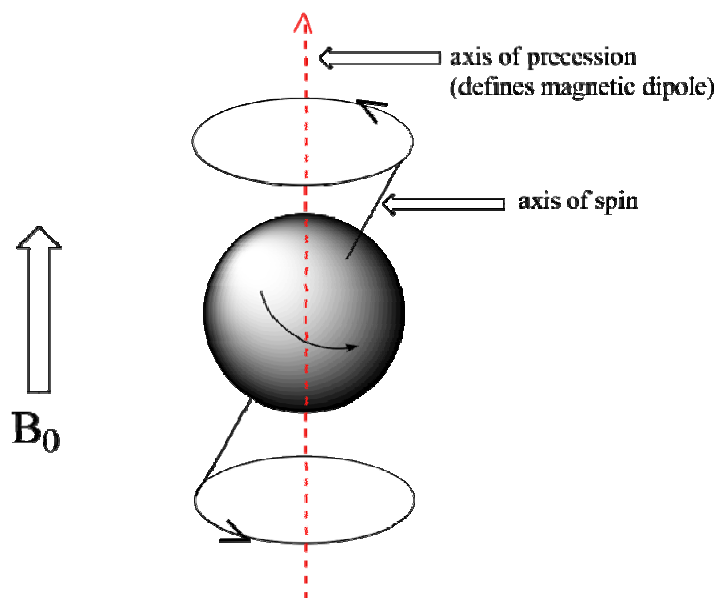


Figure 1.4. Spin precession under the effect of a magnetic field

In Table 1.1, some of the nuclei that are more commonly used in NMR are shown<sup>71</sup>. Basically, NMR can only be performed on isotopes with high natural abundance which possess a non-zero nuclear spin.

In NMR spectroscopy, the detection signal is collected based on the difference between the amount of energy absorbed or emitted by the spins. When the transition is performed from a lower energy state to a higher energy state the

Table 1.1. Some of the nuclei more commonly used in NMR Spectroscopy with the details of their unpaired protons, unpaired neutrons, net spin and gyromagnetic ratio.

Nuclei	Unpaired Protons	Unpaired Neutrons	Net Spin	$\gamma$ (MHz/T)
$^1\text{H}$	1	0	1/2	42.58
$^2\text{H}$	1	1	1	6.54
$^{31}\text{P}$	1	0	1/2	17.25
$^{23}\text{Na}$	1	2	3/2	11.27
$^{14}\text{N}$	1	1	1	3.08
$^{13}\text{C}$	0	1	1/2	10.71
$^{19}\text{F}$	1	0	1/2	40.08

spins absorb energy and when the transition is from a higher energy state to a lower energy state, the spins emit energy. In this sense, the population of spins in each state is deterministic and the output signal is proportional to this population difference. NMR is a sensitive spectroscopy, since it's capable of detecting very small differences in population. This sensitivity is due to the resonance, or energy exchange between the spins and the spectrometer which occurs at a specific frequency.

### 1.3.2 NMR Solid State Quantum Computer

Nuclear magnetic resonance provides a realistic environment to implement a quantum information processing (QIP) unit. Maturity of NMR spectroscopy is a key advantage in coherent manipulation of spin dynamics. Previously, for the sake of observation and understanding, the liquid state NMR has been used to conduct research and experiment with QIPs. However, the small number of

realizable qubits in a liquid-state NMR quantum computer, gave birth to the development of scalable solid state NMR quantum computers using spin 1/2 particles.

Before following along with the solid state NMR quantum computer idea, we review some of the advantages of this method compared to the liquid state NMR. Basically, a solid state NMR QIP has four advantages in this sense. First, to increase the sensitivity of the system required for read-out processes and exporting the results of computations among many qubits, the solid state NMR QIP offers a highly polarized system. Second, the solid state NMR QIP compared to its ancestor, suffers from slower decoherence rates. Third, inter-spin couplings are stronger which enables the system to perform faster and more reliable computations. This permits the QIP unit to deal with algorithms with higher degrees of complexity. Finally, in the solid state designs, there are possible methods and dynamic mechanisms to reset the qubits to their initial conditions. This permits removing information from the system and also generates suitable groundwork to implement efficient error-correcting codes.

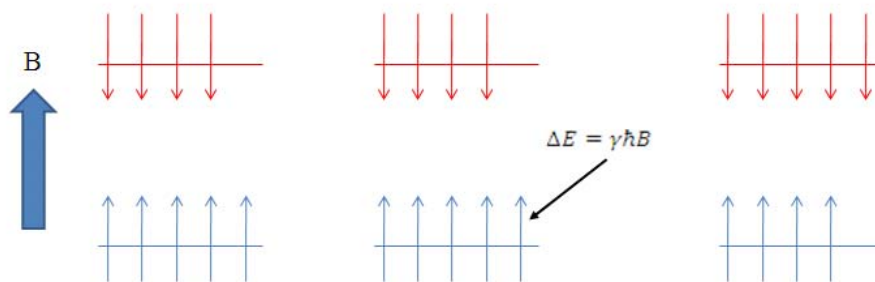


Figure 1.5. The energy required to cause the spin-flip,  $\Delta E$ , depends on the magnetic field strength at the nucleus.

The Hamiltonian of the quantum system together with the suitable coupling to external RF fields provides all the required ingredients to construct a basic quantum gate. Single quantum gates can be realized by on and off resonant RF pulses provided that, the resonance frequencies of the involved spins are far apart. In addition, two-qubit quantum gates can also be created by embedding an intentional delay between the pulses to exploit the coupling of qubits in the Hamiltonian of the system.

Single qubit manipulations would be done with the use of NMR. If we apply a static magnetic field, all the spins polarize in the direction of the applied field. For flipping the spins of phosphorus nuclei we apply a RF magnetic field, as shown in Fig. 1.5, with certain frequency to drive the qubit into resonance. However, to avoid driving all the qubits at once, an off resonant RF field is applied and the active qubit (marked in red in Fig. 1.5) is tuned into resonance when desired by using the interaction with its electron spin (hyperfine interaction). The electron spin in turn is controlled by drifting the Phosphorus electron distribution with a voltage applied to a nearby gate, called the A-gate. The process of driving a qubit into resonance with the RF field, also called spin addressing, is illustrated in Fig. 1.6.

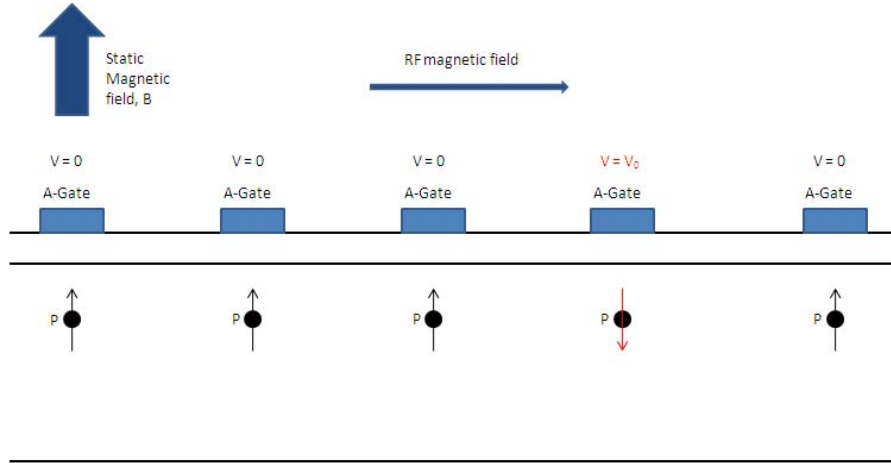


Figure 1.6. The process of driving the addressed qubit (marked in red) into resonance with the RF field.  $V_0$  is applied on the A-gate of the qubit and other qubits are left unexcited.

The discovery of quantum mechanics showed the potential ability in manipulating information in a more powerful way than its classical model and can be considered as a revolution in the computation theory. In principle, the drawbacks of quantum information processing systems can be reduced as the accuracy threshold theorem suggests. These limitations are caused by interfering factors such as noise and decoherence. However, it should be noted that realizing a scalable quantum computer involves a lot of practical difficulties<sup>72</sup>. This process needs accurate implementation and fabrication techniques and so far, we have only been able to realize very small scale quantum computers.

One possibility is that the required accuracies will never be achieved or on the other hand, we will not be able to introduce optimum and practical algorithms for quantum information processing. Nevertheless, as solid state NMR quantum has shown to be a suitable platform for controlling, manipulating and even observing around 100 spin coherences, this question arises that whether



or not we are able to efficiently preserve the information in the individually designed quantum bits<sup>72</sup>. This can lead to a more complex system since the stability of the QIP should be conserved.

Finally, it is worth mentioning that by everyday progresses in the fields of quantum computation and quantum control, we may encounter new physics theories in the future which disprove the possibility of realizing a scalable quantum computer. Consequently, the close accompaniment of practical physics and principle theories is of great significance.

#### **1.4 Research Motivation**

Using the embedded spin in a silicon environment has been proposed previously to realize a qubit<sup>1</sup>. Following Kane's idea, many studies have investigated more on this design to accurately determine the relation of the gate voltage and nuclear magnetic resonance (NMR) frequency<sup>37,39,73-75</sup>. To establish this relation, several studies have applied the perturbation theory<sup>37,75,76</sup> to this system, considering the applied voltage on the A-gate as a small perturbation affecting the original unperturbed structure with the silicon substrate and donor phosphorus. However, in applying the perturbation theory, only perturbation of the first order has been considered previously<sup>75</sup>, except the article by Larionov *et al.*<sup>37</sup>. Nevertheless, even in the Larionov study, perturbation terms include only up to 2s orbitals for the hydrogenic wavefunctions. Basically, the major contribution of the A-gate potential is a linear perturbation. Hence, the inclusion of only 1s and 2s spherically symmetric wavefunctions results in a zero net effect. In other words, only the effect of the non-linear portion of the perturbation is reflected by s orbitals while major role of the linear perturbation is neglected. In Hui<sup>75</sup> study, first

order perturbation theory is used which is found to be insufficient since the perturbation theory of first order underestimates the nonlinear characteristic of the potential distribution inside the silicon layer. To improve the above mentioned issues in applying the perturbation theory, we formulate a second order perturbation analysis. To account for the effect of the external applied voltage as the perturbation to the system, we consider up to 3d hydrogenic wavefunctions in our calculations.

For the unperturbed system, the wavefunctions and energy levels of Hamiltonian obtained by Ning and Sah<sup>77</sup> are well known and have been extensively used before. Their result is based on a modification to Effective Mass Theory (EMT) first proposed by Kohn and Luttinger<sup>42,78-80</sup>. The main advantage of Ning and Sah's work is the use of single effective mass instead of two. Apart from the simplicity that this method offers, the energy levels obtained through this scheme present close agreement with the experimental values<sup>81</sup>. However, the value of the wavefunction of the ground state at the position of the donor needs to be modified by a "central-cell correction factor"<sup>42</sup> in order to make an agreement between this method and experimental results. To remove the "central cell correction factor" from our formulation we used the revised approach introduced in a recent report<sup>82</sup> in which the correct forms of perturbed wavefunction are provided to obtain the magnitude squares of the electron state functions  $|\Psi(\mathbf{r}_0)|^2$  even at the position of the phosphorus donor.

Another issue that is frequently found in the literature is the use of analytical methods for obtaining the potential distribution and assumption of linear potential profile inside the silicon substrate<sup>37</sup>. This assumption is only valid for

some ideal structures of the metallic strip. In our method, we first used the green function method to solve the Poisson equation and later for more complex structures we applied a computer-aided numerical method (CST<sup>83</sup>) which gives the exact potential distributions of the A-gate structures inside the silicon substrate. It should be noted that this EM simulator gives the three-dimensional potential distribution inside the silicon substrate due to an arbitrary voltage excited on the A-gate lead. Using these methods, any geometric shape of an A-gate structure can be simulated to a very high accuracy, with no need of any kind of unrealistic assumptions.

Studies<sup>14,15,17,84</sup> have suggested that in realization of a quantum computer, the use of electron spin qubit as compared to the nuclear spin qubit lead to designing systems with faster clock speeds. However, in all of these studies, an accurate method for determining the conditions of operation in the electron-spin quantum bit such as the magnetic resonance frequency of the electron spin and its dependence on the applied voltage is missing. We use the previously mentioned perturbation method together with the computer aided simulation software to investigate the details of this type of qubit.

Due to the typical structure of the Kane's A-gate and its simplicity, especially for demonstration purposes, most of the studies following along Kane's idea<sup>75,85,86</sup>, adopted the original structure without any modification to the A-gate geometry. Nevertheless, the existence of some drawbacks in Kane's A-gate motivated us to make some improvements to the qubit structure. The first issue is that the ground plane at the bottom of the structure is not compatible with other electric-field- or magnetic-field-controlled devices<sup>12,87</sup>. Existence of ground gate and A-gate in the same plane, facilitate the fabrication of the qubit

and reduces the sensitivity of performance to the thickness of the silicon layer. In addition, it is easier to integrate the qubit unit with other ancillary devices (such as reading out devices), if the ground gate is not restricting the substrate from the bottom.

Finally, the Kane's structure shows a poor efficiency in using the gate voltage for controlling the NMR frequency of the phosphorus nucleus. To reduce the effect of the above mentioned issues, we have introduced two new A-gate designs, coplanar A-gate and split-ground A-gate. The advantages and disadvantages of these new geometries have been discussed and their effectiveness in controlling the NMR frequency is compared with Kane's original design.

## **1.5 Organization of the Thesis**

This thesis is directed towards the design, simulation and electromagnetic analysis of silicon quantum bits used in realization of a scalable solid state quantum computer. The scope of this thesis is first, to formulate the second order perturbation theory to obtain the wavefunction of the perturbed system. We have rigorously derived the necessary equations for the calculation of the magnetic resonance frequencies. Using this perturbation formulation and based on modified EMT theory we have analyzed two novel A-gate structures which can replace the original Kane's idea.

In chapter 2 we present two principle theories we have used in our analysis. Firstly, The Effective Mass Theory has been introduced to provide the reader with an insight to the nature of unperturbed Hamiltonian eigenfunctions. Secondly, we have shown, in extensive details, the derivation of second order

perturbation terms used to obtain the perturbed wavefunction. Also, we have shown the application of perturbation formulas in our problem of interest.

In chapter 3 we have discussed about the two simulation methods that have been used in this project. First, the green function method has been introduced which was used primarily to obtain the potential distribution inside the qubit structure. Later, as required by more complex A-gate structures, we used a computer simulation method<sup>83</sup> in order to calculate the exact potential profile caused by the newly proposed A-gate designs. The potential data is then exported to MATLAB for numerical estimation of perturbation coefficients.

Chapter 4 presents the accurate analysis of Kane's and other qubit designs based on the discussions provided in chapter 2 and 3. In this section, using the CST software we simulate the Kane's structure to show the potential profile inside the silicon layer in the position of phosphorus atom. Also, the effect of changing the insulator on the potential profile is investigated by using an alternative material. Assuming that the information on the perturbed wavefunction is provided, we can use the relevant formulations to calculate the NMR frequency of the doped phosphorus.

In chapter 5 we show some of the results related to the Electron Magnetic Resonance of the Kane's qubit structure such as electron magnetic resonance frequency and tunable bandwidth.

In chapter 6, two novel A-gate structures, coplanar A-gate and split-ground A-gate, are proposed and analyzed based on the theoretical and numerical approaches introduced in the previous chapters. The advantages and disadvantages of these structures are discussed and their NMR frequencies are compared as we change the A-gate applied voltage. Also, the potential

distribution inside Kane's, coplanar and split-ground A-gates are shown for comparison. Finally, we show the effect of adjacent qubits on the performance of the main qubit for these three structures.

In Chapter 7, after giving a summary of all the contributions of this dissertation we propose some of the possible future studies that can be considered for a more efficient analysis and design of spin-based semiconductor quantum bits.

# **Chapter 2**

## **Theoretical Analysis**

In Kane's model, an important step is to establish the relation between the applied A-gate voltage and the NMR frequency of the donor. Several studies have used the perturbation theory<sup>37,75,76</sup>, treating the A gate voltage as a small perturbation to the original unperturbed system with the donor phosphorus atom inside a silicon substrate. Another approach is to solve the changed Poisson equation including the A gate voltage term directly, usually by a numerical method<sup>39</sup>. For the perturbation approach, only first order perturbation has been considered previously<sup>75</sup>, except the study by Larionov *et al.*<sup>37</sup>. However the Larionov study adopted an analytical approach for obtaining the A-gate potential which means that it is only applicable to ideal structures of A gates (an ideal circular plate). Furthermore, for the second order perturbation theory considered by Larionov *et al.*, the perturbation includes only up to the  $2s$  term for the hydrogenic wavefunction. As we know, the major part of the A-gate voltage introduces a linear perturbation under which the inclusion of the  $1s$  and  $2s$  spherically symmetric hydrogenic wavefunctions only gives a zero net effect. Hence the mere inclusion of the  $1s$  and  $2s$  wavefunction terms only accounts for the non-linear perturbation introduced by the A-gate voltage, while the major linear perturbation has not been accounted for. For the study by Hui<sup>75</sup>, the perturbation theory was again used. However, this study considered perturbation up to the first order only. This was insufficient because due to a rather nonlinear nature of the external applied potential distribution inside the silicon substrate, the first order perturbation substantially under-estimates this effect. In order to improve on this, we carry out a second order perturbation analysis of the additional effect



due to the potential introduced by the A-gate voltage. We will consider up to the  $2p$ ,  $3s$ ,  $3p$ , and  $3d$  hydrogenic orbitals in our theory.

The wavefunctions and energy levels of the unperturbed Hamiltonian  $H_0$  are well known and we use those obtained by Ning and Sah<sup>77</sup> (Appendix I) who considered a modified effective-mass theory (EMT) proposed by Kohn and Luttinger<sup>42,78-80</sup> 35-38. The advantage of Ning and Sah's results is that they used a single effective mass instead of two. This substantially simplifies the formulation of the perturbation theory. Another reason is that the energy levels obtained from their results are in close agreements with the experimental values<sup>81</sup>. The disadvantage is that the value of the ground state wavefunction at the donor site has to be corrected by the so-called "central-cell correction"<sup>42</sup> in order to match with the experimental value. In order to remove this disadvantage, we have used the revised unperturbed wavefunctions in the calculation of the perturbed wavefunction in (2) provided in a recent report<sup>27</sup> which formulated the correct unperturbed wavefunctions that correctly produce the magnitude squares of the wavefunctions  $|\Psi(\mathbf{r}_0)|^2$  at the donor nucleus position. In essence, the report in Ref.<sup>82</sup> provides a more accurate effective-mass-theory (EMT) equation for the wavefunction of a phosphorus donor in a silicon host by correctly taking into account of the inter-valley mixing effect of the silicon conduction band structure. The most important result of this reformulated EMT equation is that the unperturbed wavefunctions (i.e.,  $\Psi_{4i}(\mathbf{r})$ ,  $\Psi_{2s}(\mathbf{r})$ , and  $\Psi_{3s}(\mathbf{r})$  in (2)) can be calculated accurately, not only their energy levels but also their specific values at the donor site  $\mathbf{r} = \mathbf{r}_0$ . This eliminates the usual practice of needing to artificially introduce a so-called central-cell correction factor to account for the difference

between the theoretically calculated and the experimental measured value of the magnitude squares of the wavefunctions  $|\Psi(\mathbf{r}_0)|^2$  at the donor site.

## 2.1 Effective Mass Theory for Silicon-Based Devices

The effective mass theory (EMT) has widely been used to describe the electron structure and excited states of shallow impurities in semiconductors. In the seminal proposal of Luttinger and Kohn<sup>78</sup>, the shallow impurity atom embedded inside the silicon was modeled as a hydrogen atom with the impurity ion playing the role of the hydrogen core. Later, it was shown<sup>42</sup> that there are some inconsistency between the calculated results based on EMT and experimental values. This nonoccurrence was observed especially for the ionization energy (experimental value was 45.47 meV and calculated value based on EMT was reported to be 29 meV). For the calculation of the square modulus of the ground-state wavefunction at the donor position,  $|\Psi_{A_1}(0)|^2$  the "central-cell correction" method had to be used to compensate for the difference between experimental and EMT-calculated results ( $4.1 \times 10^{29} \text{ m}^{-3}$  obtained from EMT and  $4.4 \times 10^{29} \text{ m}^{-3}$  obtained experimentally). Two main factors have been suggested to account for the above-mentioned mismatches: (i) the invalidity of the assumed impurity potential screened by the dielectric constant in the vicinity of nucleus which is far from a columbic potential and significantly affects the accuracy of calculation especially in 1S state, (ii) the negligence of inter-valley effects arising from the band structure of the silicon because of the presence of six conduction minima in the lowest conduction band. Later, these six minima were shown to be split into three different sub-levels<sup>88</sup>. Ning and Sah<sup>77</sup>, proposed a new formulation for the EMT by using

variational method and taking into account the effect of inter-valley mixing. This study provided accurate results for the energies of the three sub-level ground states. Ever since, many studies have tried to improve Ning and Sah's work<sup>77</sup> by more accurately investigating the effect of inter-valley mixing<sup>46,89,90</sup>. Most of the theories and formulations proposed so far, haven't been able to predict accurately both the energy levels and  $|\Psi_{A_1}(0)|^2$  i.e. the ground state wavefunction of the impurity at the nucleus site<sup>39,45,73,91,92</sup>. In this dissertation we have used the theory proposed by Hui<sup>82</sup> which enables us to accurately calculate both energy levels and donor-site wavefunction, even for the A1 state, which is the lowest lying sub-level of the 1S state. The details of this formulation can be found in Ref.<sup>82</sup>.

## 2.2 Perturbation Theory

Similar to the case of classical mechanics, there are few realistic problems in quantum mechanics that can be solved for a closed-form solution. Therefore, making use of approximation methods is inevitable in nearly all of the physically worthwhile applications of the quantum mechanics theory. The Rayleigh-Schrodinger perturbation theory or perturbation theory in short, which studies the effect of a small disturbance to the unperturbed system, will be discussed below for a time-independent Hamiltonian.

Let us assume that the Hamiltonian of an arbitrary time-independent system is stated as:

$$H = H_0 + \lambda H' \quad (2.1)$$

where  $H_0$  is the unperturbed Hamiltonian pertaining to the system without any disturbance which, we shall suppose, can be simply solved using an unperturbed Schrödinger equation:

$$H_0 \psi_n^{(0)} = E_n^{(0)} \psi_n^{(0)} \quad (2.2)$$

and  $\lambda H'$  is the term accounting for the perturbation. The parameter  $\lambda$  is a real quantity and introduces the order of perturbation. If  $\lambda$  goes to zero, the system Hamiltonian  $H$  tends to the unperturbed system Hamiltonian,  $H_0$ . On the other hand, we may choose  $\lambda$  to be 1 as its full value.

Assuming that the eigenfunctions  $\psi_n^{(0)}$  linked to the eigenvalues  $E_n^{(0)}$  of the unperturbed Hamiltonian  $H_0$  form an orthonormal set we can write:

$$\langle \psi_i^{(0)} | \psi_j^{(0)} \rangle = \delta_{ij} \quad (2.3)$$

where  $\psi_i^{(0)}$  and  $\psi_j^{(0)}$  are two arbitrary eigenfunctions from the above-mentioned set and  $\delta_{ij}$  is the Kronecker delta function and for simplicity of formulation we suppose the system is introduced by only discrete states. Since in the next chapters we will only deal with non-degenerate ground-states, in the following formulation of the perturbation theory we will assume all the energy levels to be non-degenerate. Consider the eigenvalue problem which we intend to solve

$$H \psi_n = E_n \psi_n \quad (2.4)$$

Thus, we can start by assuming that  $E_n^{(0)}$ , a particular energy level of the unperturbed Hamiltonian, is the nearest unperturbed level to the perturbed energy level  $E_n$ . This is because the perturbation  $\lambda H'$  is very small compared to  $H_0$ . As  $\lambda$  approaches zero:

$$\lim_{\lambda \rightarrow 0} E_n = E_n^{(0)} \quad (2.5)$$

$$\lim_{\lambda \rightarrow 0} \psi_n = \psi_n^{(0)} \quad (2.6)$$

The general concept of the perturbation theory is to expand the perturbed eigenfunctions and eigenvalues in powers of  $\lambda$ ,

$$E_n = \sum_{j=0}^{\infty} \lambda^j E_n^{(j)} \quad (2.7)$$

$$\psi_n = \sum_{j=0}^{\infty} \lambda^j \psi_n^{(j)} \quad (2.8)$$

where  $j$  is the order of perturbation. Putting the expressions 2.8 and 2.7 into the Schrödinger equation 2.4 we obtain

$$\begin{aligned} & (H_0 + \lambda H') (\psi_n^{(0)} + \lambda \psi_n^{(1)} + \lambda^2 \psi_n^{(2)} + \dots) \\ & = (E_n^{(0)} + \lambda E_n^{(1)} + \lambda^2 E_n^{(2)} + \dots) \times (\psi_n^{(0)} + \lambda \psi_n^{(1)} + \lambda^2 \psi_n^{(2)} + \dots) \end{aligned} \quad (2.9)$$

Equating the coefficient of the terms with same power of  $\lambda$  in both sides of the above equation we find that for  $\lambda^0$ , the expected equation 2.2 appears. for  $\lambda^1$  we have

$$H_0\psi_n^{(1)} + H'\psi_n^{(0)} = E_n^{(0)}\psi_n^{(1)} + E_n^{(1)}\psi_n^{(0)} \quad (2.10)$$

while the coefficient for  $\lambda^2$  gives us

$$H_0\psi_n^{(2)} + H'\psi_n^{(1)} = E_n^{(0)}\psi_n^{(2)} + E_n^{(1)}\psi_n^{(1)} + E_n^{(2)}\psi_n^{(0)} \quad (2.11)$$

Generally for the case of  $\lambda^j$  we have

$$H_0\psi_n^{(j)} + H'\psi_n^{(j-1)} = E_n^{(0)}\psi_n^{(j)} + E_n^{(1)}\psi_n^{(j-1)} + \dots + E_n^{(j)}\psi_n^{(0)} \quad (2.12)$$

After some manipulations to equations 2.10 to 2.12 we obtain first-order energy term  $E_n^{(1)}$  as

$$E_n^{(1)} = \left\langle \psi_n^{(0)} \left| H' \right| \psi_n^{(0)} \right\rangle \quad (2.13)$$

This equation is simply the perturbation factor  $H'$  averaged over  $\psi_n^{(0)}$  the unperturbed eigenfunction of the system.

In a similar manner, we will find the second-order correction term to the energy of the system

$$E_n^{(2)} = \left\langle \psi_n^{(0)} \left| H' - E_n^{(1)} \right| \psi_n^{(1)} \right\rangle \quad (2.14)$$

It is worth mentioning that knowing the unperturbed state function  $\psi_n^{(0)}$  is sufficient for obtaining  $E_n^{(0)}$  and  $E_n^{(1)}$ , while calculating  $E_n^{(1)}$  need the knowledge of  $\psi_n^{(1)}$ . As a general rule, knowing  $\psi_n^{(0)}, \psi_n^{(1)}, \dots, \psi_n^{(s)}$ , gives all the information needed to obtain the energy correction terms  $E_n^{(0)}, E_n^{(1)}, \dots, E_n^{(2s-1)}$ .

### 2.2.1 First Order Perturbation Theory

By recalling equation 2.10 and following the Rayleigh-Schrödinger method, we expand  $\psi_n^{(1)}$  as a superposition of basis states obtained from solving the unperturbed Hamiltonian equation:

$$\psi_n^{(1)} = \sum_k a_{nk}^{(1)} \psi_k^{(0)} \quad (2.15)$$

Now, we substitute the above expansion into equation 2.10 to obtain

$$(H_0 - E_n^{(0)}) \sum_k a_{nk}^{(1)} \psi_k^{(0)} + (H' - E_n^{(1)}) \psi_n^{(0)} = 0 \quad (2.16)$$

After some manipulation of the above equation, we derive:

$$a_{nl}^{(1)} (E_l^{(0)} - E_n^{(0)}) + H'_{ln} - E_n^{(1)} \delta_{nl} = 0 \quad (2.17)$$

where we used  $H'_{ln} \equiv \langle \psi_l^{(0)} | H' | \psi_n^{(0)} \rangle$ . Leaving the special case of  $n = l$  for

later, we find the expression for first-order perturbation coefficient  $a_{nl}^{(1)}$  as

$$a_{nl}^{(1)} = \frac{H'_{ln}}{E_n^{(0)} - E_l^{(0)}}, \quad l \neq n \quad (2.18)$$

Later we return to finding the term  $a_{nn}^{(1)} = \langle \psi_n^{(0)} | \psi_n^{(0)} \rangle$  which is indeed the projection of  $\psi_n^{(1)}$  along  $\psi_n^{(0)}$  and cannot be found from equation 2.18.

## 2.2.2 Second Order Perturbation Theory

Following the same method we can expand the second order perturbation function as

$$\psi_n^{(2)} = \sum_k a_{nk}^{(2)} \psi_k^{(0)} \quad (2.19)$$

And obtain an expression for the second order perturbation coefficients

$$a_{nl}^{(2)} (E_l^{(0)} - E_n^{(0)}) + \sum_k H'_{lk} a_{nk}^{(2)} - E_n^{(1)} a_{nl}^{(1)} - E_n^{(2)} \delta_{nl} = 0 \quad (2.20)$$

For  $n = l$  we have

$$E_n^{(2)} = \sum_{k \neq n} \frac{H'_{nk} H'_{kn}}{E_n^{(0)} - E_k^{(0)}} = \sum_{k \neq n} \frac{|H'_{kn}|^2}{E_n^{(0)} - E_k^{(0)}} \quad (2.21)$$

Thus, the second order energy correction term is obtained by performing the above-mentioned summation. We should note that in the case of ground state, the term  $E_n^{(0)} - E_k^{(0)}$  is always negative for  $k \neq n$ ; hence  $E_n^{(2)}$ , the second order correction of the energy is always negative.

In summary, we can write the expression for a perturbed energy level by applying the perturbation theory to second order (we have set  $\lambda = 1$ )

$$E_n = E_n^{(0)} + H'_{nn} + \sum_{k \neq n} \frac{|H'_{kn}|^2}{E_n^{(0)} - E_k^{(0)}} \quad (2.22)$$

Considering equation 2.20 and remembering that  $E_n^{(1)} = H'_{nn}$ , we obtain the expression for  $a_{nl}^{(2)}$  when  $l \neq n$  which is the general case,



$$\begin{aligned}
a_{nl}^{(2)} = & \frac{1}{E_n^{(0)} - E_l^{(0)}} \sum_{k \neq n} \frac{H'_{lk} H'_{kn}}{E_n^{(0)} - E_k^{(0)}} - \frac{H'_{nn} H'_{ln}}{(E_n^{(0)} - E_l^{(0)})^2} \\
& - a_{nn}^{(1)} \frac{H'_{ln}}{E_n^{(0)} - E_l^{(0)}}
\end{aligned} \tag{2.23}$$

As mentioned previously about  $a_{nn}^{(1)}$ , also  $a_{nn}^{(2)}$  cannot be determined from equation 2.23.

More generally we have

$$a_{nn}^{(j)} = \langle \psi_n^{(0)} | \psi_n^{(j)} \rangle, \quad j \geq 1 \tag{2.24}$$

where  $a_{nn}^{(j)}$  represents the component of  $\psi_n^{(j)}$  along  $\psi_n^{(0)}$ . Due to the loss of information on  $a_{nn}^{(j)}$ , we are not able to use equations 2.21 to 2.23 to find these coefficients. Thus we can infer that these quantities are not physically valuable and choosing the appropriate coefficient can be determined merely by the assumptions on the perturbed wavefunction  $\psi_n$ . One way is to find these coefficients in a way that the perturbed wavefunction is normalized to 1, of course by making the assumption of expanding  $\psi_n$  up to  $j$ th order of  $\lambda$ ,

$$\begin{aligned}
& \langle \psi_n | \psi_n \rangle \\
& \simeq \langle \psi_n^{(0)} + \lambda \psi_n^{(1)} + \dots + \lambda^j \psi_n^{(j)} | \psi_n^{(0)} + \lambda \psi_n^{(1)} + \dots + \lambda^j \psi_n^{(j)} \rangle \\
& = 1 + \mathcal{O}(\lambda^{j+1})
\end{aligned} \tag{2.25}$$

where  $\mathcal{O}(\lambda^{j+1})$  is a type of error function of the order  $\lambda^{j+1}$ . Thus, for first order correction we may write:

$$\langle \psi_n^{(0)} | \psi_n^{(1)} \rangle + \langle \psi_n^{(1)} | \psi_n^{(0)} \rangle = 0 \tag{2.26}$$

or equivalently

$$a_{nn}^{(1)} + a_{nn}^{(1)*} = 0 \quad (2.27)$$

The above equation means that the real part of  $a_{nn}^{(1)}$  should be zero. In a similar way, for second order correction we may write

$$\langle \psi_n^{(0)} | \psi_n^{(2)} \rangle + \langle \psi_n^{(2)} | \psi_n^{(0)} \rangle + \langle \psi_n^{(1)} | \psi_n^{(1)} \rangle = 0 \quad (2.28)$$

And therefore,

$$a_{nn}^{(2)} + a_{nn}^{(2)*} + \sum_k |a_{nk}^{(1)}|^2 = 0 \quad (2.29)$$

Again, the above equation gives the real part of  $a_{nn}^{(2)}$  like equation 2.27 which determined the real part of  $a_{nn}^{(1)}$ . Since there is no information about the imaginary part of coefficients in equations 2.29 and 2.27, without loss of generality, we can set the imaginary parts to zero. Thus for second order correction we have,

$$a_{nn}^{(1)} = 0, \quad a_{nn}^{(2)} = -\frac{1}{2} \sum_{k \neq n} |a_{nk}^{(1)}|^2 \quad (2.30)$$

And finally the perturbed wavefunction is obtained to second order by ( $\lambda = 1$ )

$$\psi_n = \psi_n^{(0)} + \psi_n^{(1)} + \psi_n^{(2)} \quad (2.31)$$

Where

$$\psi_n^{(1)} = \sum_{l \neq n} \frac{H'_{ln}}{E_n^{(0)} - E_l^{(0)}} \psi_l^{(0)} \quad (2.32)$$

and

$$\begin{aligned} \psi_n^{(2)} = \sum_{l \neq n} \left[ \sum_{k \neq n} \frac{H'_{ln}}{(E_n^{(0)} - E_l^{(0)})(E_n^{(0)} - E_k^{(0)})} \right. \\ \left. - \frac{H'_{nn}H'_{ln}}{(E_n^{(0)} - E_l^{(0)})^2} \right] \psi_l^{(0)} \\ - \frac{1}{2} \sum_{k \neq n} \frac{|H'_{kn}|^2}{(E_n^{(0)} - E_k^{(0)})^2} \psi_n^{(0)} \end{aligned} \quad (2.33)$$

Choosing the above method ensures that the perturbed wavefunction is normalized up to a particular order of  $j$ . However, another method used for determining the coefficients  $a_{nn}^{(j)}$  is

$$a_{nn}^{(j)} = 0, \quad j \geq 1 \quad (2.34)$$

Using the second convention, the first order perturbed wavefunction is normalized similar to the previous case. However, the higher order perturbed functions don't obey this rule. Nevertheless, to solve this problem, we may need to introduce some normalization constant  $N(\lambda)$  such that  $\langle N(\lambda)\psi_n | N(\lambda)\psi_n \rangle = 1$ .

### 2.2.3 Implementation of Perturbation Theory in the Qubit Problem

Performing a second order perturbation theory we have:

$$\begin{aligned}
\Psi'_{A_1} &= \Psi_{A_1} + \lambda\Psi^{(1)} + \lambda^2\Psi^{(2)} \\
\text{Norm} &= |\Psi'_{A_1}| = \sqrt{\langle \Psi'_{A_1} | \Psi'_{A_1} \rangle} \\
\Psi'_{A_1, \text{norm}} &= \frac{1}{\text{Norm}} (\Psi_{A_1} + \lambda\Psi^{(1)} + \lambda^2\Psi^{(2)})
\end{aligned} \tag{2.35}$$

where  $\Psi'_{A_1}$  is the perturbed wavefunction for the ground states,  $\Psi_{A_1}$  is the unperturbed ground-state wavefunction, Norm is the normalization constant and  $\Psi'_{A_1, \text{norm}}$  is the normalized perturbed wavefunction for the ground state. We follow the perturbation theory method by expanding first and second order correction functions  $\Psi^{(1)}$  and  $\Psi^{(2)}$  in terms of unperturbed basis functions. In our method we have used unperturbed basis function up to 3d levels i.e. we have used basis functions A1, 2s, 2p, 3s, 3p and 3d. In addition since we are only interested in the wavefunction at the donor position we set the argument to zero. Recalling equation 2.15 and 2.19 we have

$$\psi^{(1)}(0) = \alpha_{A1}^{(1)}\psi_{A1}(0) + \alpha_{2s}^{(1)}\psi_{2s}(0) + \alpha_{3s}^{(1)}\psi_{3s}(0) \tag{2.36}$$

and

$$\psi^{(2)}(0) = \alpha_{A1}^{(2)}\psi_{A1}(0) + \alpha_{2s}^{(2)}\psi_{2s}(0) + \alpha_{3s}^{(2)}\psi_{3s}(0) \tag{2.37}$$

The reason we have only considered three of the basis functions and ignored the rest is the fact that only s orbital wavefunctions have a contribution at the origin and p and d wavefunctions vanishes at the nucleus position. Now we use the formulation of the previous section to determine the coefficient of perturbation terms. It should be noted that we have used a new method for the

normalization in which we first obtain the whole expression of the perturbed wavefunction and then normalize it.

$$\begin{aligned}
\Psi'_{A_1} &= \Psi_{A_1} + \lambda\Psi^{(1)} + \lambda^2\Psi^{(2)} \\
\text{Norm} &= |\Psi'_{A_1}| = \sqrt{\langle \Psi'_{A_1} | \Psi'_{A_1} \rangle} \\
\langle \Psi'_{A_1} | \Psi'_{A_1} \rangle &= \langle \Psi_{A_1} + \lambda\Psi^{(1)} + \lambda^2\Psi^{(2)} | \Psi_{A_1} + \lambda\Psi^{(1)} + \lambda^2\Psi^{(2)} \rangle
\end{aligned} \tag{2.38}$$

After putting the expression for first and second order perturbation terms in eq. 2.38 we derive the Norm of the perturbed wavefunction

$$\begin{aligned}
&\langle \Psi'_{A_1} | \Psi'_{A_1} \rangle \\
&= 1 + 2 \text{Re} \left\{ \lambda\alpha_{2s}^{(1)} H_{A_1 2s} + \lambda\alpha_{3s}^{(1)} H_{A_1 3s} \right\} \\
&+ 2 \text{Re} \left\{ \lambda^2\alpha_{2s}^{(2)} H_{A_1 2s} + \lambda^2\alpha_{3s}^{(2)} H_{A_1 3s} \right\} \\
&+ |\lambda\alpha_{2s}^{(1)}|^2 + |\lambda\alpha_{2p10}^{(1)}|^2 + |\lambda\alpha_{2p11}^{(1)}|^2 + |\lambda\alpha_{2p1-1}^{(1)}|^2 \\
&+ |\lambda\alpha_{3s}^{(1)}|^2 + |\lambda\alpha_{3p10}^{(1)}|^2 + |\lambda\alpha_{3p11}^{(1)}|^2 + |\lambda\alpha_{3p1-1}^{(1)}|^2 \\
&+ |\lambda\alpha_{3d20}^{(1)}|^2 + |\lambda\alpha_{3d21}^{(1)}|^2 + |\lambda\alpha_{3d2-1}^{(1)}|^2 + |\lambda\alpha_{3d22}^{(1)}|^2 + |\lambda\alpha_{3d2-2}^{(1)}|^2 \\
&+ 2 \text{Re} \left\{ \lambda\alpha_{2s}^{(1)*} \lambda^2\alpha_{2s}^{(2)} + \lambda\alpha_{2p10}^{(1)*} \lambda^2\alpha_{2p10}^{(2)} + \lambda\alpha_{2p11}^{(1)*} \lambda^2\alpha_{2p11}^{(2)} \right. \\
&+ \lambda\alpha_{2p1-1}^{(1)*} \lambda^2\alpha_{2p1-1}^{(2)} + \lambda\alpha_{3s}^{(1)*} \lambda^2\alpha_{3s}^{(2)} + \lambda\alpha_{3p10}^{(1)*} \lambda^2\alpha_{3p10}^{(2)} \\
&+ \lambda\alpha_{3p11}^{(1)*} \lambda^2\alpha_{3p11}^{(2)} + \lambda\alpha_{3p1-1}^{(1)*} \lambda^2\alpha_{3p1-1}^{(2)} + \lambda\alpha_{3d20}^{(1)*} \lambda^2\alpha_{3d20}^{(2)} \\
&+ \lambda\alpha_{3d21}^{(1)*} \lambda^2\alpha_{3d21}^{(2)} + \lambda\alpha_{3d2-1}^{(1)*} \lambda^2\alpha_{3d2-1}^{(2)} \\
&\left. + \lambda\alpha_{3d22}^{(1)*} \lambda^2\alpha_{3d22}^{(2)} + \lambda\alpha_{3d2-2}^{(1)*} \lambda^2\alpha_{3d2-2}^{(2)} \right\} \\
&+ |\lambda^2\alpha_{2s}^{(2)}|^2 + |\lambda^2\alpha_{2p10}^{(2)}|^2 + |\lambda^2\alpha_{2p11}^{(2)}|^2 + |\lambda^2\alpha_{2p1-1}^{(2)}|^2 \\
&+ |\lambda^2\alpha_{3s}^{(2)}|^2 + |\lambda^2\alpha_{3p10}^{(2)}|^2 + |\lambda^2\alpha_{3p11}^{(2)}|^2 + |\lambda^2\alpha_{3p1-1}^{(2)}|^2 \\
&+ |\lambda^2\alpha_{3d20}^{(2)}|^2 + |\lambda^2\alpha_{3d21}^{(2)}|^2 + |\lambda^2\alpha_{3d2-1}^{(2)}|^2 + |\lambda^2\alpha_{3d22}^{(2)}|^2 + |\lambda^2\alpha_{3d2-2}^{(2)}|^2
\end{aligned} \tag{2.39}$$

Thus, for the perturbed wavefunction we have

$$\begin{aligned} & \Psi'_{A_1, norm}(0) \\ & \approx \frac{1}{\text{Norm}} \left[ \Psi_{A_1}(0) + (\lambda \alpha_{2s}^{(1)} + \lambda^2 \alpha_{2s}^{(2)}) \Psi_{2s}(0) + (\lambda \alpha_{3s}^{(1)} + \lambda^2 \alpha_{3s}^{(2)}) \Psi_{3s}(0) \right] \end{aligned} \quad (2.40)$$

Following the same method as discussed before, all the coefficients and energy correction terms of the perturbed wavefunction in eq. 2.39 and 2.40 can be obtained. These coefficients are presented in Appendix II. The only difference is that A1 state is not orthogonal to 2s and 3s states and this should be taken into account.

### 2.3 Summary

In this chapter, firstly, we have introduced the revised Effective mass theory that has been reported in a recent study. This method enables us to modify the previous EMT formulations and remove the so-called "central cell correction factor" from the perturbation analysis and to accurately calculate the unperturbed wavefunctions and energy levels even at the donor site  $\mathbf{r} = \mathbf{r}_0$ . An introduction of previous EMT methods and their disadvantages has been given. Secondly, we have provided the details of second order perturbation theory and its implementation in our problem of interest. We first introduced the first order perturbation correction and then expanded this analysis to the second order. All the coefficient of the perturbed wavefunction are obtained by mathematical manipulations of the equations provided in this chapter and are presented in Appendix II. In order to expand the wavefunctions we have used up to 3d orbital basis states and finally the normalization method used in this project has been discussed.

**Chapter 3**

**The Electromagnetic**

**Numerical and Simulation**

**Method**

### 3.1 Using Multi-layered Green Function to Solve the Integral Equation

The determination of the NMR frequencies of the phosphorus donor consists of two steps. The first step is to calculate the electric potential distribution  $V(\mathbf{r})$  inside the silicon substrate for a known A-gate voltage. The second step is to calculate the change of NMR frequency.

In order to solve the first problem, primarily we used the multilayered Green's functions to solve an integral equation by the moment method<sup>88</sup>. The multilayered Green's functions are obtained from the work of Li *et al.*<sup>93</sup> for qubit structure and are presented in this section.

In this method, the Poisson's equation  $\nabla^2 V(\mathbf{r}) = -Q(\mathbf{r})/\epsilon_{Si}$  (where  $\epsilon_{Si}$  is the permittivity of silicon) for the static electric potential  $V(\mathbf{r})$  induced by an arbitrary 3D A-gate structure is solved first by formulating an integral equation for the charge distribution  $Q(\mathbf{r})$  on the A gate as:

$$V_0(\mathbf{r}) = \iint_S G_{33}(\mathbf{r}|\mathbf{r}') Q(\mathbf{r}') ds' \quad (3.1)$$

where  $G_{33}(\mathbf{r}|\mathbf{r}')$  is the Green's function<sup>40</sup> for the potential on the A gate due to a unit charge on the A gate itself. The Green's function  $G_{33}(\mathbf{r}|\mathbf{r}')$  was obtained by considering a general multilayered planar structure<sup>93</sup> with  $G_{33}(\mathbf{r}|\mathbf{r}')$  being formulated to satisfy all the boundary conditions on each layer (details in Ref.<sup>93</sup>). Eq. (3.1) is solved numerically by the moment method<sup>94</sup> for  $Q(\mathbf{r})$  with a given known potential  $V_0(\mathbf{r})=1$  V on the A gate.



Once the charge distribution  $Q(\mathbf{r})$  is known, the potential inside the silicon substrate is calculated by the following integration formula<sup>93</sup>:

$$V(\mathbf{r}) = \iint_S G_{13}(\mathbf{r}|\mathbf{r}') Q(\mathbf{r}') ds' \quad (3.2)$$

where  $G_{13}(\mathbf{r}|\mathbf{r}')$  is the Green's function<sup>94</sup> for the potential inside the silicon substrate due to a unit charge on the A gate. Note that in (3.1), the field coordinate  $\mathbf{r}$  is on the A-gate while in (3.2)  $\mathbf{r}$  can be any location inside the silicon substrate. From (3.2), it can be seen that the potential distribution  $V(\mathbf{r})$  is a complex function of both the highly localized Green's function  $G_{13}(\mathbf{r}|\mathbf{r}')$  and the charge distribution function  $Q(\mathbf{r})$  which result in  $V(\mathbf{r})$  being far from a linear distribution. The use of a numerical method can accommodate an arbitrary geometry of the A gate, facilitating an engineering approach to solve this problem.

Below is the list of green functions used for a three-layered structure in which the excitation source is placed on top of the second layer right in the interface of second and third layers. In the qubit problem, layer 1 is associated with the silicon substrate, layer 2 is the silicon dioxide layer and layer 3 is assumed to be the free space above the structure. in this formulation  $(x, y, z)$  represents the field coordinates while the source coordinates are shown with  $(x', y', z')$  which both are local coordinates relating to each layer. Spectral domain kernel, which can be numerically calculated by Prony's method, is then used to express the various green's functions. Finally the spatial Green's functions

are numerically obtained using the complex image method. Following is the list of above-mentioned three-layered Green's functions.

$$G_{13}(x, y, z | x', y', z') = \frac{1}{(2\pi)^2} \int_{-\infty}^{\infty} \int_{-\infty}^{\infty} \tilde{G}_{13}(k_x, k_y, z, z') \exp[-jk_x(x-x')] \exp[-jk_y(y-y')] dk_x dk_y \quad (3.3)$$

where the spectral domain kernel is

$$\begin{aligned} \tilde{G}_{13}(k_x, k_y, z, z') = & \left( \frac{1}{\varepsilon_0 \gamma} \right) \times \left( \frac{\varepsilon_{r2} \sinh(\gamma z)}{\sinh(\gamma h_1) \sinh(\gamma h_2)} \right) / (\varepsilon_{r2} \varepsilon_{r3}) \\ & + \varepsilon_{r2} \varepsilon_{r3} \coth(\gamma h_2) + \varepsilon_{r1} \varepsilon_{r3} \coth(\gamma h_1) + \varepsilon_{r1} \varepsilon_{r2} \coth(\gamma h_1) \coth(\gamma h_2) \end{aligned} \quad (3.4)$$

with  $\gamma = \sqrt{k_x^2 + k_y^2}$ .  $G_{13}(x, y, z | x', y', z')$  is the Green's function for the potential inside silicon layer (layer 1) produced by a unit charge in the metallic strip in layer 3. The other two Green's functions are

$$G_{23}(x, y, z | x', y', z') = \frac{1}{(2\pi)^2} \int_{-\infty}^{\infty} \int_{-\infty}^{\infty} \tilde{G}_{23}(k_x, k_y, z, z') \exp[-jk_x(x-x')] \exp[-jk_y(y-y')] dk_x dk_y \quad (3.5)$$

where

$$\begin{aligned} \tilde{G}_{23}(k_x, k_y, z, z') = & \left( \frac{1}{\varepsilon_0 \gamma} \right) \times \frac{\varepsilon_{r1} \coth(\gamma h_1) \sinh(\gamma z) + \varepsilon_{r2} \cosh(\gamma z)}{\sinh(\gamma h_2)} / (\varepsilon_{r2} \varepsilon_{r3}) \\ & + \varepsilon_{r2} \varepsilon_{r3} \coth(\gamma h_2) + \varepsilon_{r1} \varepsilon_{r3} \coth(\gamma h_1) + \varepsilon_{r1} \varepsilon_{r2} \coth(\gamma h_1) \coth(\gamma h_2) \end{aligned} \quad (3.6)$$

Finally, the potential inside the free space above the structure (layer 3) is represented by another Green's function produced by a unit charge on the metallic strip in layer 3,

$$G_{33}(x, y, z | x', y', z') = \frac{1}{(2\pi)^2} \int_{-\infty}^{\infty} \int_{-\infty}^{\infty} \tilde{G}_{33}(k_x, k_y, z, z') \exp[-jk_x(x-x')] \exp[-jk_y(y-y')] dk_x dk_y \quad (3.7)$$

where

$$\begin{aligned} \tilde{G}_{33}(k_x, k_y, z, z') &= \left( \frac{1}{\epsilon_0 \gamma} \right) \times (\epsilon_{r1} \coth(\gamma h_1) + \epsilon_{r2} \coth(\gamma h_2)) / (\epsilon_{r2} \epsilon_{r3} \\ &+ \epsilon_{r2} \epsilon_{r3} \coth(\gamma h_2) + \epsilon_{r1} \epsilon_{r3} \coth(\gamma h_1) + \epsilon_{r1} \epsilon_{r2} \coth(\gamma h_1) \coth(\gamma h_2)) \end{aligned} \quad (3.8)$$

Using the Green's function introduced above, the charge distribution  $Q(x', y')$  on the metallic A-gate strip as the result of a unit voltage on the A-gate can be calculated by numerically solving the following integral equation. This integral equation is solved using the moment method.

$$1 = \iint_S G_{33}(x, y, 0 | x', y', 0) Q(x', y', z') dx' dy' \quad (3.9)$$

where  $S$  shows the area of the A gate strip. assuming  $Q(x', y')$  is obtained, the potentials in different layers due to a unit voltage on the A-gate strip can be calculated as:

$$V_{13}(x, y, z) = \iint_S G_{13}(x, y, z | x', y', 0) Q(x', y') dx' dy', \quad \text{in layer 1} \quad (3.10)$$

$$V_{23}(x, y, z) = \iint_S G_{23}(x, y, z | x', y', 0) Q(x', y') dx' dy', \quad \text{in layer 2} \quad (3.11)$$

$$V_{33}(x, y, z) = \iint_S G_{33}(x, y, z | x', y', 0) Q(x', y') dx' dy', \quad \text{in layer 3} \quad (3.12)$$

### 3.2 Using Computer-Aided Simulation Method

In order to analyze qubit structures with complex geometrical parameters, using the Green's function can be tedious and sometimes even impossible. To design the new A-gate structures (introduced later in chapter 6) and to characterize their performance, we use a computer-aided numerical method. First, the exact potential distributions of the A-gate structures inside the silicon substrate are obtained using an electromagnetic simulation tool - the CST Electrostatic Module<sup>83</sup>. Note that this EM simulator gives the three-dimensional potential distribution inside the silicon substrate due to an arbitrary voltage excited on the A-gate lead. In this way, any geometric shape of an A-gate structure can be simulated to a very high accuracy, with no need of any kind of unrealistic assumptions.

CST STUDIO SUITE is a multi-purpose electromagnetic simulation software. The foundation method of this simulator is the Finite Integration Technique<sup>95</sup>, which was proposed for the first time by Weiland in 1976/1977<sup>96</sup>.

The Finite Integration Technique<sup>95</sup> provides a general spatial discretization method which is applicable to a wide range of electromagnetic problems.

These problems may be ranging from static field and low frequency simulations to high frequency calculations in both time and frequency domains.

### 3.2.1 Finite Integration Method and Discrete Electromagnetism

Unlike most of the numerical techniques which use differential form of the Maxwell's equations, the discretization scheme used in FIT involves the integral form of the Maxwell's equations:

$$\begin{aligned}
 \oint_{\partial A} \vec{E} \cdot d\vec{s} &= - \int_A \frac{\partial \vec{B}}{\partial t} \cdot d\vec{A}, & \oint_{\partial A} \vec{H} \cdot d\vec{s} &= \int_A \left( \frac{\partial \vec{D}}{\partial t} + \vec{J} \right) \cdot d\vec{A}, \\
 \oint_{\partial V} \vec{D} \cdot d\vec{A} &= \int_V \rho dV, & \oint_{\partial V} \vec{B} \cdot d\vec{A} &= 0.
 \end{aligned}
 \tag{3.13}$$

To find the numerical solutions to these equations, one should first define a finite simulation domain which encloses all the components of the problem structure. The next step is to divide this domain into small grid cells by choosing a suitable method for mesh generation. For sake of simplicity, we will first consider the orthogonal hexahedral mesh system. In CST, the primary mesh system can be chosen in a visual format. However, an internal dual mesh is defined by the software which is orthogonal to the primary mesh set. Finally, the Maxwell's equations are spatially discretized using these two orthogonal mesh systems and the integral values are used as the degrees of freedom. as shown in the following Fig. 3.1, the primary grid  $\mathbf{G}$  is used for allocating electric grid voltages and magnetic side wall fluxes represented by  $\mathbf{e}$  and  $\mathbf{b}$  respectively.

On the other hand, the dual grid  $\tilde{G}$  (represented by tilde) is used for the dielectric side wall fluxes  $\mathbf{d}$  and magnetic grid voltages  $\mathbf{h}$ :

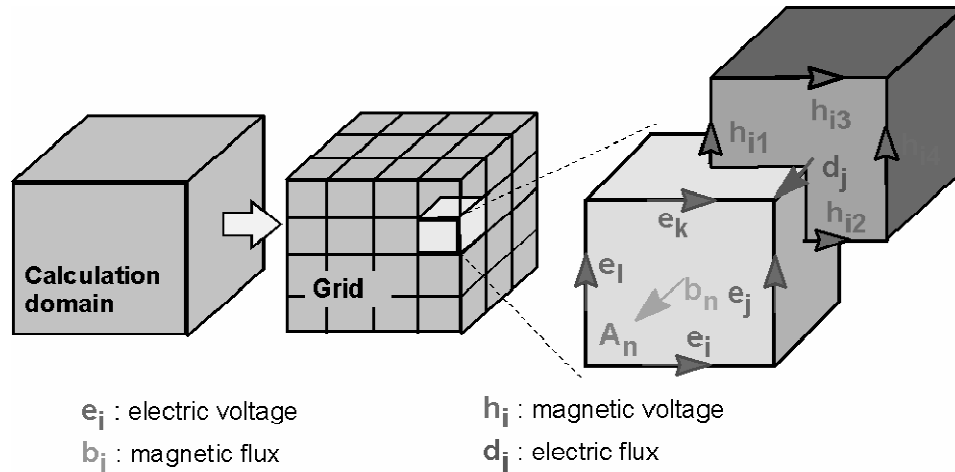


Figure 3.1. Two orthogonal mesh systems. the primary grid  $G$  is used for allocating electric grid voltages and magnetic side wall fluxes represented by  $e$  and  $b$  respectively. The dual grid  $\tilde{G}$  (represented by tilde) is used for the dielectric side wall fluxes  $d$  and magnetic grid voltages  $h$ . This image is reproduced from CST advanced topics Manual<sup>83</sup>.

The next step is to formulate the Maxwell's equations for every cell face wall (facet) individually as shown in the Fig. 3.2. For Faraday's Law, we can replace the closed integral on the left hand side of the equation with the sum total of four grid voltages. This simplification doesn't introduce any error factor to our calculations. Therefore, the right hand side of the equation is equivalent to the time derivative of the magnetic flux integrated on the encircled primary cell facet as shown in the figure below. By carrying out the same procedure for all of the cell facets in the primary grid, we obtain a matrix representation. This topological matrix  $\mathbf{C}$ , obtained by summarizing the

calculation rule in all the cell facets, is the discrete representation of the curl operator in the Faraday's law.

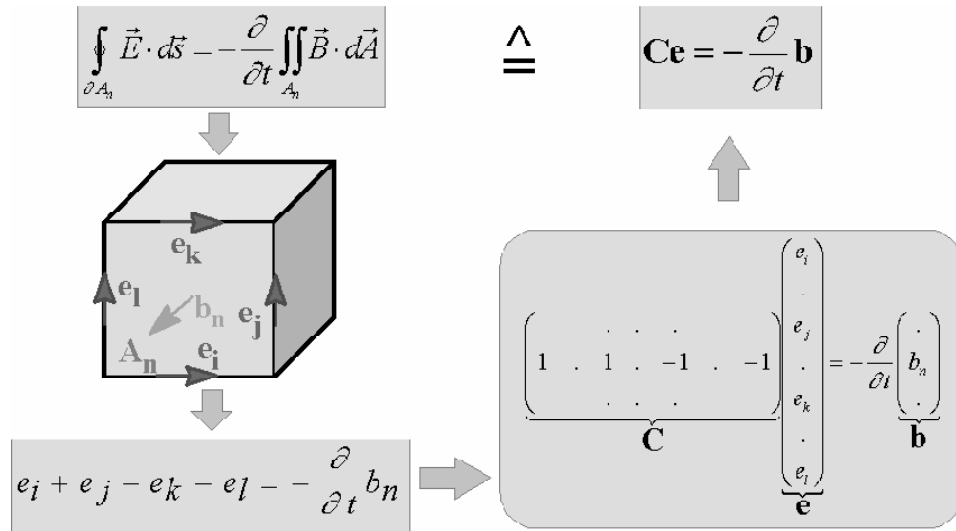


Figure 3.2. For Faraday's Law, the closed integral on the left hand side of the equation can be replaced by the sum total of four grid voltages. The matrix representation of the Faraday's law is shown. This image is reproduced from CST advanced topics Manual<sup>83</sup>.

Repeating the above-mentioned procedure for Ampere's Law, it is required to define a dual discrete curl operator  $\mathbf{C} \sim$  on the dual grid. Applying the same scheme for discretizing the remaining two divergence equations results in definition of discrete divergence operator pair:  $\mathbf{S}$  and  $\mathbf{S} \sim$  which correspond respectively to the primary and dual grids. As mentioned before, these discrete matrix representations are merely composed of '0', '1' and '-1' elements which carry topological information. The complete set of discrete Maxwell's Grid Equations (MGEs) are:

$$\begin{aligned}
\mathbf{C}\mathbf{e} &= -\frac{d}{dt}\mathbf{b}, & \tilde{\mathbf{C}}\mathbf{h} &= -\frac{d}{dt}\mathbf{d} + \mathbf{j}, \\
\tilde{\mathbf{S}}\mathbf{d} &= \mathbf{q}, & \mathbf{S}\mathbf{b} &= \mathbf{0}.
\end{aligned}
\tag{3.14}$$

Comparing the above form of Maxwell's equations to the continuous description confirms the similarity between the two representations. Once again it should be emphasized that up to this stage, no discretization error has been spotted in the change of representation. One of the vital aspects of using FIT is that by discretizing the Maxwell's equations in grid space, continuous operators (gradient, curl and divergence) still preserve their important properties.

$$\begin{aligned}
\mathbf{S}\mathbf{C} = \tilde{\mathbf{S}}\tilde{\mathbf{C}} = 0 & \quad \Leftrightarrow \quad \text{div rot} \equiv 0, \\
\mathbf{C}\tilde{\mathbf{S}}^T = \tilde{\mathbf{C}}\mathbf{S}^T = 0 & \quad \Leftrightarrow \quad \text{rot grad} \equiv 0.
\end{aligned}
\tag{3.15}$$

It should be pointed out that even in the case of discretizing a numerical algorithm there is a chance of long-term instability. Fortunately, referring to the fundamental relations presented above, it can be shown that such problems don't affect the formulation used in FIT. This is because both energy and charge are conserved by using the set of discretized equations (MEGs)<sup>97</sup>.

Although no supplementary error has been introduced so far, spatial discretization of the remaining material relations will cause an inevitable inaccuracy in the numerical results. In other words, definition of voltage and flux relations requires some approximation to be applied over the grid edges and cell areas to calculate their integral values. As a result, the final



coefficients depend on the material parameters averaged over the enclosed domain. In addition, the grid spatial resolution affects the final value of the parameters. Similarly, these coefficients can be summarized in matrix forms:

$$\begin{aligned}
 \vec{D} &= \epsilon \vec{E} & \mathbf{d} &= \mathbf{M}_\epsilon \mathbf{e} \\
 \vec{B} &= \mu \vec{H} & \Leftrightarrow & \mathbf{B} = \mathbf{M}_\mu \mathbf{h} & (3.16) \\
 \vec{J} &= \sigma \vec{E} + \vec{J}_s & \mathbf{j} &= \mathbf{M}_\sigma \mathbf{e} + \mathbf{j}_s
 \end{aligned}$$

Finally, all the necessary discretized matrix equations have been obtained for solving an electromagnetic problem on the grid space. Based on the discussed relations so far, it is evident that topological and metric information are presented in different matrix equations. This fact has critical consequences in theory, numerical and algorithmic calculations<sup>97</sup>.

Generally, range of application of FIT is not limited to orthogonal hexahedral grids. It can also be employed for more subtle mesh types such as tetrahedral grids and irregular grids. As shown in Fig. 3.3, the electric voltages and magnetic fluxes are assigned to facets and edges of a tetrahedral mesh cell.

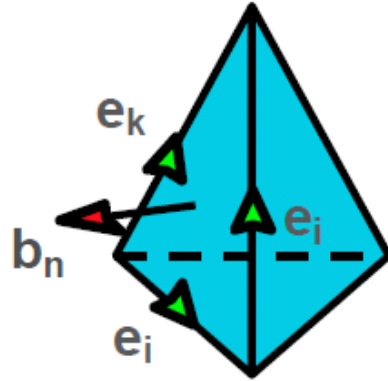


Figure 3.3. the electric voltages and magnetic fluxes assigned to facets and edges of a tetrahedral mesh cell. This image is reproduced from CST advanced topics Manual<sup>83</sup>.

The details of generalized FIT applied to these more complicated mesh types can be understood by extending the basic scheme described above<sup>98</sup>.

As shown in this section, we witnessed that FIT is a general formulation technique that can be applied to a wide range of electromagnetic problems from static and low frequencies to high frequencies.

### 3.2.2 CST Electrostatic Solver

If we consider the discretized Faraday's Law and remove its time dependency together with the corresponding divergence equation, we obtain a set of linear equations for the electrostatic problem:

$$\text{div } \varepsilon \text{ grad } \phi = -\rho \Rightarrow \tilde{\mathbf{M}}_\varepsilon \tilde{\mathbf{S}}^T \boldsymbol{\varphi}_e = \mathbf{q} \quad (3.17)$$

The electrostatic solver module is able to solve the problem with both hexahedral and tetrahedral mesh grids.

We use the CST Electrostatic Solver to simulate the qubit structure. In contrary to the unreliable analytical methods and tedious formulation of Green's functions, this module easily provides the 3D potential data inside the silicon substrate with high accuracy and without any unnecessary assumptions.

In order to validate the data obtained from CST simulation, we first calculate the capacitance for a square section of a microstrip line for two cases of dielectric constants,  $\epsilon_r = 9.6$  and  $\epsilon_r = 1$ . The computed values are normalized with respect to the capacitance of a parallel plate structure with dielectric constant of  $\epsilon = \epsilon_r \epsilon_0$ . The normalization constant is  $\epsilon W^2 / b$ , where  $W$  is the side length of the square plate and  $b$  is the separation between the square plate and ground plate. The results are shown in Fig. 3.4 and show good agreement with the results obtained by Itoh *et al*<sup>99</sup>.

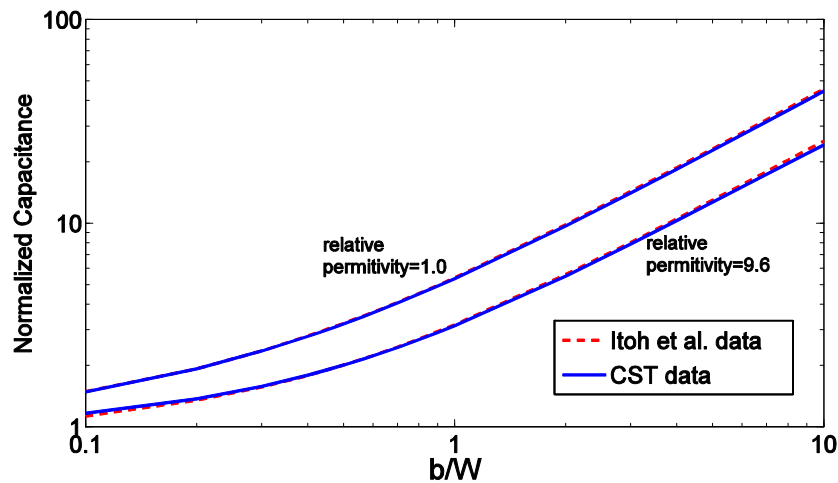


Figure 3.4. Comparison of the calculated normalized capacitance for a square section of a microstrip line obtained using CST and Itoh *et al.* the square plate has a side length of  $W$ , and  $b$  is the separation between the plates. The comparison has been carried out for two values of relative permittivity,  $\epsilon_r = 9.6$  and  $\epsilon_r = 1$ .

Furthermore in order to perform another validation for the potential distribution data, we simulate the Kane's structure using another commercial software, COMSOL Multiphysics. The potential data obtained from these two softwares are almost indistinguishable as shown in Fig. 3.5.

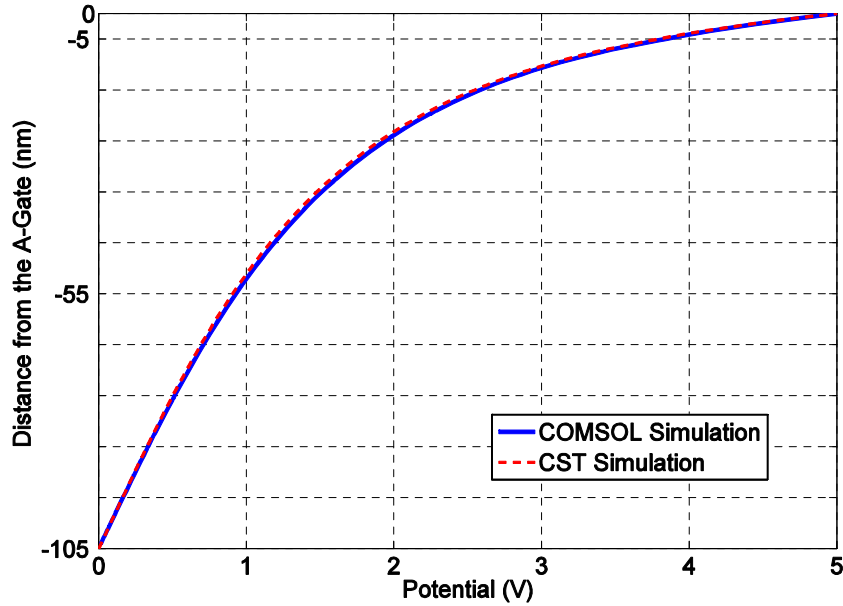


Figure 3.5. The comparison of potential data obtained from CST and COMSOL simulations. Potentials are obtained along a line drawn from A-gate lead down to the ground plane. A static voltage of 5 V is applied on the A-gate lead. For Kane's A-gate structure, the dimensions are: substrate thickness=100 nm, A-gate lead width=7 nm, insulating layer ( $\text{Si}_{0.5}\text{Ge}_{0.5}$ ) thickness=5 nm. The dielectric constant  $\epsilon_r$  of Si is 11.46 and that of SiGe is 13.95.

After obtaining the potential information inside the silicon layer, data is exported to MATLAB in order to numerically solve for the perturbed wavefunction of the donor electron. By calculating the perturbed wavefunction we have  $\Psi_{A'_i, norm}(\mathbf{r}_0)$  and subsequently we can calculate the hyperfine interaction and Magnetic Resonance Frequency as discussed in the next chapter.

### 3.3 Summary

In this chapter we try to discuss two numerical and simulation methods we have been using in order to simulate the qubit structure and obtain the potential data inside the silicon substrate. Primarily, we formulated an integral equation from the Poisson equation which can be solved using multi-layered Green's Functions to obtain the voltage distribution inside the Kane's structure. The formulations and different Green's functions are listed and solved by moment method. The advantage of this method compared to analytical approaches used before is that we don't need to make any unrealistic assumptions on the potential profile and its applicability is not limited to idealistic A-gate geometries such as circular plate A-gate. However, for the complex A-gate structures (as will be introduced in chapter 6), the Green's functions will be very difficult and time consuming to formulate and the process will be tedious. Therefore, we use an electromagnetic simulation software (CST Electrostatic Solver) to simulate the qubit unit and obtain the potential profile inside the structure. Since CST is based on Finite Integration Technique, an introduction to this numerical method has been provided in this chapter. CST software is able to easily and reliably export the 3D potential data that later can be used by MATLAB to solve the unperturbed wavefunction of the donor electron.

**Chapter 4**

**Accurate Analysis of the  
NMR Frequency of the  
Donor Atom Inside the  
A-Gate Structure**

The use of a spin embedded inside a silicon host has been proposed to be a promising method for the realization of a qubit, the basic operation unit of a quantum computer<sup>1</sup>. Since Kane<sup>9</sup> proposed the use of nuclear spins as the realization method of a silicon-based solid-state scalable quantum computer, there have been many studies on this realization method<sup>74,75,86,87,100-117</sup>. Instead of using the donor nuclear spins as qubits, one study<sup>8</sup> showed the possibility of using the nuclear spin of a silicon isotope <sup>29</sup>Si as the qubit. A digital implementation method<sup>100</sup> was later suggested as an alternative to Kane's original design. In order to overcome the oscillatory behavior of the electronic mediated exchange interaction between two neighboring phosphorus donors in a silicon host, several studies have proposed to make use of the Si/SiO<sub>2</sub> interface mode to perform the two-qubit operation<sup>53,54,101,102</sup>. Yet another study revealed the possibility of indirectly controlling the nuclear spins via anisotropic hyperfine interactions with an electron which undergoes spin transitions<sup>104</sup>. On the other hand, pursuing along Kane's original proposed design, several studies have elaborated more details on Kane's model such as more accurate determinations of the relation between the gate voltage and the nuclear magnetic resonance (NMR) frequency<sup>37,39,73-75</sup>, the determinations of the *J*-gate voltage on the exchange interaction<sup>66,86,105,106,108,109</sup>, and the study of the decoherence characteristics of the spin qubit structure<sup>110</sup>. Except these mainly theoretical studies, some initial-stage experimental studies<sup>115</sup> on Kane's proposal were also reported in the literature.

#### 4.1 The Quantum Perturbation Method Combined With Accurate EM Simulation

The original qubit structure proposed by Kane for realization in a silicon host is shown in Fig. 4.1. It is a phosphorus atom (isotope  $^{31}\text{P}$ ) doped in a silicon substrate (isotope  $^{28}\text{Si}$ ). On top of the silicon substrate is an insulating layer of silicon dioxide. At the bottom of the silicon substrate is a metallic layer served as the ground, called the back gate. On top of the silicon dioxide layer is a metallic strip, called the A gate, which carries a control voltage  $V$  through an excitation source on its other end. The dimensions of the A gate are as labeled in Fig. 4.1. The electron cloud of the phosphorus atom can be drifted by applying a voltage on the A gate. The drift of the electron cloud can change the hyperfine interaction between the phosphorus nucleus and the outermost valence electron and hence change the nuclear magnetic resonance frequency of phosphorus.

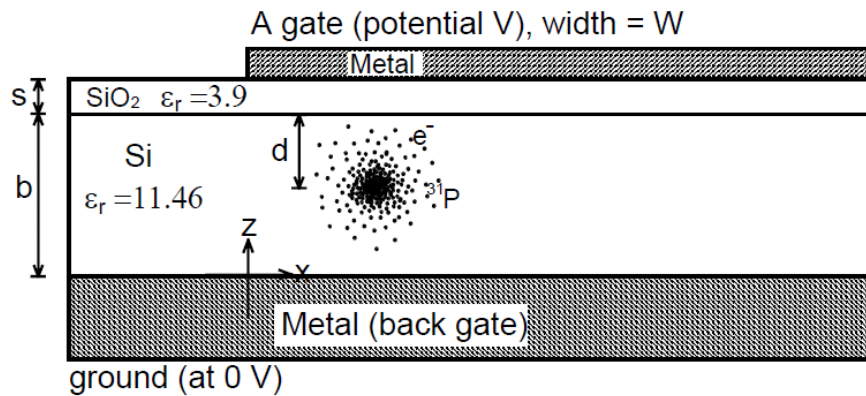


Figure 4.1. The single qubit structure of the silicon-based solid-state quantum computer proposed by Kane.



Once the accurate potential distributions of the A-gate structures are known, we use the 2<sup>nd</sup> order perturbation theory<sup>92</sup> to determine the effect of the potential distributions on the change of the hyperfine interaction and hence the change of NMR frequency of the donor phosphorus atom. Note that except the perturbation theory, there have been a number of other methods for the evaluation of the effect of potential distributions on the hyperfine interaction. These include the variational effective mass theory<sup>45,118</sup>, the tight-binding calculations<sup>49,91</sup>, the density functional theory (DFT)<sup>52</sup>, and the numerical diagonalization of the donor Hamiltonian in the basis of the pure crystal Bloch functions<sup>48</sup>. To use the perturbation method, the Hamiltonian of the donor valence electron is first written as:

$$H = H_0 + H_V \quad (4.1)$$

where  $H_0$  is the Hamiltonian with a zero control voltage on the A gate and  $H_V = eV$  is the additional electron Hamiltonian due to a control voltage  $V$  on the A gate (with  $e$  being the electron charge). As given in chapter 2, the 2<sup>nd</sup> order perturbation theory finds the perturbed wavefunction  $\Psi_{A',norm}(\mathbf{r}_0)$  of (4.1) for the donor valence electron at the donor site ( $\mathbf{r} = \mathbf{r}_0$ ) by the following formula:

$$\Psi_{A',norm}(\mathbf{r}_0) \approx \frac{1}{Norm} \left[ \Psi_{A_1}(\mathbf{r}_0) + (\alpha_{2s}^{(1)} + \alpha_{2s}^{(2)}) \Psi_{2s}(\mathbf{r}_0) + (\alpha_{3s}^{(1)} + \alpha_{3s}^{(2)}) \Psi_{3s}(\mathbf{r}_0) \right] \quad (4.2)$$

where  $Norm$  is a constant for normalizing the perturbed wavefunction and  $\alpha_{2s}^{(1)}$ ,  $\alpha_{3s}^{(1)}$  and  $\alpha_{2s}^{(2)}$ ,  $\alpha_{3s}^{(2)}$  are the first and second order coefficients for the perturbation terms (details in Appendix II). The detailed forms of the unperturbed wavefunctions in (4.2), i.e.,  $\Psi_{A_1}(\mathbf{r})$ ,  $\Psi_{2s}(\mathbf{r})$ , and  $\Psi_{3s}(\mathbf{r})$ , are given in Appendix I, in which the general forms of these wavefunctions are expressed as a composite function of two parts: an envelope function part resulting from the effective-mass-theory equation and the Bloch wave function part accounting for the motion of the donor electron inside the periodic structure of silicon. Note that  $Norm$ ,  $\alpha_{2s}^{(1)}$ ,  $\alpha_{3s}^{(1)}$  and  $\alpha_{2s}^{(2)}$ ,  $\alpha_{3s}^{(2)}$  are all calculated numerically with the values of the potential distribution being known everywhere. When  $\Psi_{A_1, norm}(\mathbf{r}_0)$  is known, the hyperfine interaction constant  $A_h$  is calculated by<sup>37</sup>:

$$A_h = \frac{2}{3} |\Psi_{A_1, norm}(\mathbf{r}_0)|^2 \mu_B g_N \mu_N \mu_0 \quad (4.3)$$

where  $\mu_B$  is the Bohr magnetron,  $g_N$  is the nuclear  $g$ -factor for  $^{31}\text{P}$ ,  $\mu_N$  is the nuclear magnetron, and  $\mu_0$  is the permeability of free space. Note that comparing the formula in (4.3) to the same formula in previous reports<sup>92</sup>, it can be seen that the correction factor,  $c$ , has been removed from (4.3). The reason is that we have used the revised unperturbed wavefunctions in the calculation of the perturbed wavefunction in (4.2) provided in a recent report<sup>82</sup> which formulated the correct unperturbed wavefunctions that correctly produce the magnitude squares of the wavefunctions  $|\Psi(\mathbf{r}_0)|^2$  at the donor

nucleus position. In essence, the report in Ref.<sup>82</sup> provides a more accurate effective-mass-theory (EMT) equation for the wavefunction of a phosphorus donor in a silicon host by correctly taking into account of the inter-valley mixing effect of the silicon conduction band structure. The most important result of this reformulated EMT equation is that the unperturbed wavefunctions (i.e.,  $\Psi_{A_1}(\mathbf{r})$ ,  $\Psi_{2s}(\mathbf{r})$ , and  $\Psi_{3s}(\mathbf{r})$  in (2)) can be calculated accurately, not only their energy levels but also their specific values at the donor site  $\mathbf{r} = \mathbf{r}_0$ . This eliminates the usual practice of needing to artificially introduce a so-called central-cell correction factor to account for the difference between the theoretically calculated and the experimental measured value of the magnitude squares of the wavefunctions  $|\Psi(\mathbf{r}_0)|^2$  at the donor site. The details of this formulation can be found in Ref.<sup>82</sup>. After the hyperfine constant  $A_h$  is known, the nuclear spin magnetic resonance frequency  $f$  is calculated by (to the second order accuracy)<sup>9,39</sup>

$$hf = 2g_N\mu_N B + 2A_h + \frac{2A_h^2}{\mu_B B} \quad (4.4)$$

where  $h$  is the Planck's constant and  $B$  is the applied static magnetic field.

## 4.2 Potential Distribution Results

For a common Kane's A-gate structure studied before by several authors with the dimensional parameters given by  $s = 5$  nm,  $b = 60$  nm,  $W = 7$  nm,  $\epsilon_r$  of silicon = 11.46,  $\epsilon_r$  of silicon dioxide = 3.9 the potential distribution results are shown in Fig. 4.2. As can be seen, for a practical A gate structure as shown in

Fig. 4.1, the potential distribution inside the silicon substrate is far from a linear one in contrast with the assumption of a linear voltage distribution across the silicon substrate in the previous studies.

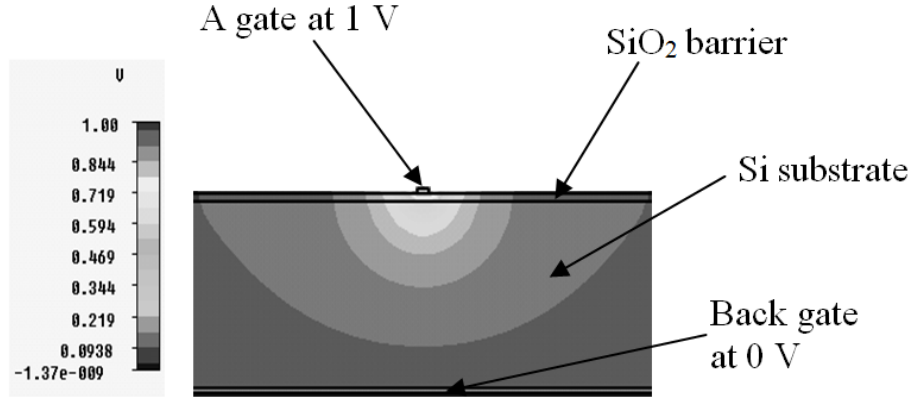


Figure 4.2. The nonlinear potential distribution inside the silicon substrate of the qubit structure shown in Fig. 4.1 with  $s = 5$  nm,  $b = 100$  nm,  $W = 7$  nm,  $\epsilon_r$  of silicon = 11.46, and  $\epsilon_r$  of silicon dioxide = 3.9.

From the electromagnetic analysis point of view, this nonlinear potential distribution is a result of the finite narrow width of the A gate metallic strip which causes the electric field to concentrate more along its surface rather than to extend evenly down to the back gate (the ground). Furthermore, the presence of the barrier layer  $\text{SiO}_2$  with a much lower dielectric constant ( $\epsilon_r = 3.9$ ) just beneath the A gate will actually absorb most of potential drop from the A-gate, causing a very inefficient use of the applied voltage on the A gate. To solve this problem, we have proposed a method to be discussed later on this chapter.

In Fig. 4.3, we calculate the perturbation energy ( $\lambda E^{(1)} + \lambda^2 E^{(2)}$  in (4)). The dimensional parameters of the A gate structure are  $s = 5$  nm,  $b = 100$  nm,  $W = 7$  nm,  $\epsilon_r$  of silicon = 11.46, and  $\epsilon_r$  of silicon dioxide = 3.9 and the phosphorus atom is now placed at  $x = 20$  nm,  $y = 0$ , and  $z = 50$  nm. This is to

anticipate the inclusion of the  $3d$  sub-orbitals (which have a much larger spatial extent) in the calculation of the perturbed wavefunction. The result is compared with the estimation obtained by using Kohn's Stark shift formula<sup>42</sup>. It can be seen that the Stark shift estimation is much smaller than our calculations. This is because the Stark shift formula in Kohn's study<sup>42</sup> is based on a linear potential distribution which results in all the first-order perturbation terms being vanished.

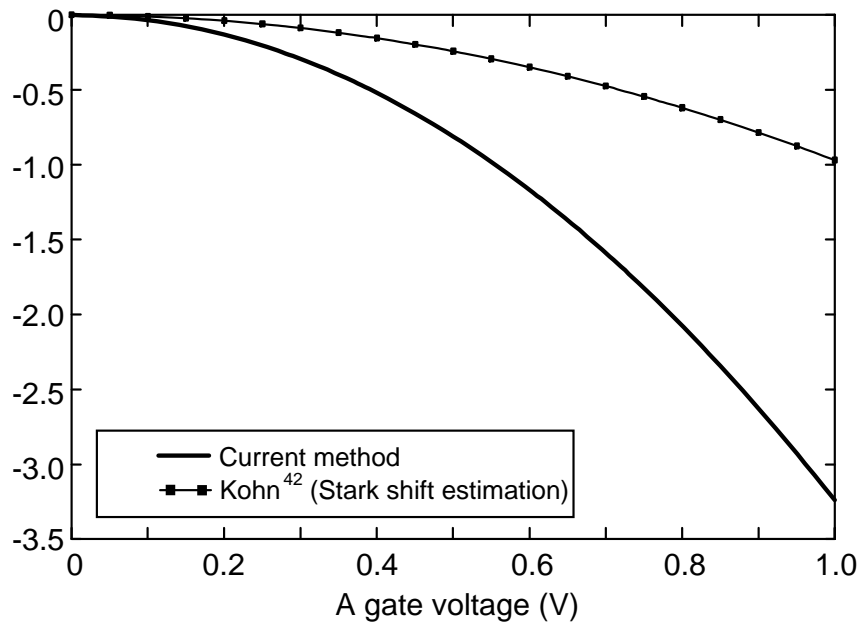


Figure 4.3. The perturbation energy with respect to the change in the A gate voltage. The phosphorus atom is at  $x = 20$  nm,  $y = 0$ , and  $z = 50$  nm. The other parameters are:  $s = 5$  nm,  $b = 100$  nm,  $W = 7$  nm,  $\epsilon_r$  of silicon = 11.46, and  $\epsilon_r$  of silicon dioxide = 3.9.

However, in our method, the nonlinear potential distribution leads to non-zero first-order perturbation terms. Another reason may be that we include more higher-order states (such as  $2p$ ,  $3s$ ,  $3p$ , and  $3d$ ) in our calculation than Kohn's study did. Furthermore, as we can see, the greatest perturbation energy is only about -3 meV, which is much smaller than the energy level of the ground stage ( $\sim 45$  meV). This justifies the use of a perturbation theory to solve this

problem. From the results in Figs. 4.3 and 4.2, it can be seen that the nonlinear potential distribution inside the silicon substrate is a significant consideration in designing practical A gates.

For practical A gate structures, numerical studies<sup>75</sup> have revealed the nonlinear potential distributions inside the silicon substrate. Furthermore, for the material combination of Si/SiO<sub>2</sub> (silicon substrate and silicon dioxide insulation layer), it was found<sup>75</sup> that most of the applied A gate voltage is actually dropped across the SiO<sub>2</sub> layer though it is much thinner than the silicon substrate. This reduces the effectiveness of the A gate control and is not an optimum design. In the original proposal of Kane's quantum computer, Kane proposed an alternative<sup>9</sup> to the Si/SiO<sub>2</sub> design, the Si/SiGe combination. In this A gate structure, the SiGe material instead of SiO<sub>2</sub> is used as the insulation layer. SiGe has a much greater dielectric constant than SiO<sub>2</sub>. One of the compounds of SiGe (Si<sub>0.5</sub>Ge<sub>0.5</sub>) has a dielectric constant<sup>119</sup> of  $\epsilon_r = 13.95$ , much greater than that of SiO<sub>2</sub> ( $\epsilon_r = 3.9$ ). A more similar dielectric constant of SiGe to Si ( $\epsilon_r = 11.46$ ) will actually push a greater portion of A gate voltage being dropped across the silicon substrate and not the insulation layer. This is shown in Fig. 4.4, which shows clearly that the combination of Si/SiGe results in a much larger portion (~67%) of the A gate voltage being dropped across the silicon substrate, compared with that for the case of Si/SiO<sub>2</sub> (~47%).

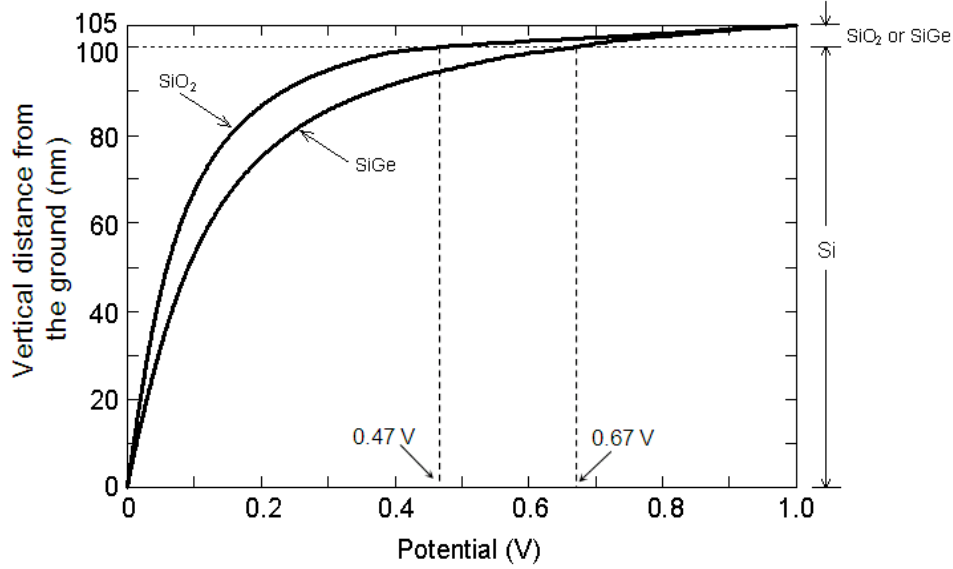


Figure 4.4. The potential distributions along the  $z$  direction at  $x = 20$  nm and  $y = 0$  inside an A gate structure with different insulator barrier materials. The dimensions of the A gate are:  $s = 5$  nm,  $b = 100$  nm,  $W = 7$  nm, and  $\epsilon_r$  of silicon = 11.46. For the  $\text{SiO}_2$  insulation barrier,  $\epsilon_r = 3.9$ . For the SiGe insulation barrier,  $\epsilon_r = 13.95$ .

### 4.3 Summary

In this chapter by using the second order perturbation theory, Kane's solid state quantum bit is analyzed and its NMR frequency is investigated in details. Higher-order excited states (up to  $3d$  modes) are included in our calculation of second order perturbation theory and the perturbation energies are obtained numerically. Potential distributions inside Kane's qubit are calculated using the numerical and simulation methods introduced in chapter 3. The results show that the potential profiles are far from linear ones. We also investigate an alternative A-gate structure using SiGe as the insulation barrier. Our study shows that this A-gate structure offers a much more efficient utilization of the control voltage than the original A-gate structure using  $\text{SiO}_2$  as the insulation barrier.

**Chapter 5**

**Electron Magnetic**

**Resonance Analysis of the**

**Electron-Spin Based Qubit**



Studies<sup>14,15,17,84</sup> in quantum computer realization methods have suggested the use of electron spin as the qubit to achieve a much faster clock speed than that based on a nuclear spin. Obviously, except for the possibility to speed up the gate operation time, an electron-spin based qubit structure will have the additional advantages of easing the state read-out circuit design and facilitating the building of a CNOT gate. A method known as the “global control of the electron spin” has been proposed by Hill et al.<sup>15</sup> to realize the fast gate operation time provided by the electron-spin qubit. Earlier than that, Vrijen et al.<sup>17</sup> have proposed the design of an electron-spin-resonance transistor to use an electron spin as the qubit for a quantum computer. Sousa et al.<sup>14</sup> proposed to use the magnetic dipolar interaction between electron spins for the realization of a quantum computer. More recently, Tsai et al.<sup>84</sup> reported to apply the gradient ascent pulse engineering approach to reduce the gate operation time of an electron-spin based quantum computer by almost three times compared to that achieved by the “global control of the electron spin” method. All these studies have demonstrated the possibility of using the electron spin to realize a “high speed” quantum computer. Notwithstanding these studies, an accurate determination of the operation conditions of an electron-spin based quantum computer such as the electron-spin magnetic resonant frequency and its relation to the external A gate voltage has not been obtained before. In this chapter, we use the previously introduced numerical method to investigate the relation between the externally applied A gate voltage and the magnetic resonant frequency of an electron spin. The electric potential distribution inside the qubit structure is accurately calculated by a rigorous electromagnetic field simulation method. The perturbation method is

then applied to determine the electron-spin magnetic resonant frequency. Our results show that for the same A gate structure as originally proposed by Kane<sup>9</sup> for the nuclear spin qubit operation, the choice of the static magnetic field  $B$  is important in order to achieve a magnetic resonant frequency with a manageable tunable bandwidth.

### **5.1 Perturbation Analysis for the Electron-Spin Magnetic Resonance Frequency**

The electron spin single qubit structure to be considered is the same as the nuclear spin single qubit structure originally proposed by Kane<sup>9</sup> by doping a donor atom (isotope  $^{31}\text{P}$ ) into a silicon host (isotope  $^{28}\text{Si}$ ) as was previously shown in chapter 4 and is illustrated again in Fig.5.1 . By applying a voltage on the top A gate, the hyperfine interaction and so the magnetic resonance frequency of the electron spin of the donor phosphorus electron can be changed. This enables the addressing of a particular qubit via an electric field control. Note that though the magnetic resonance frequency of the donor nuclear spin also changes due to a change of the hyperfine interaction, the donor nuclear spin is only treated as a localization site for the donor electron and does not take part in the operation of the electron spin qubit.

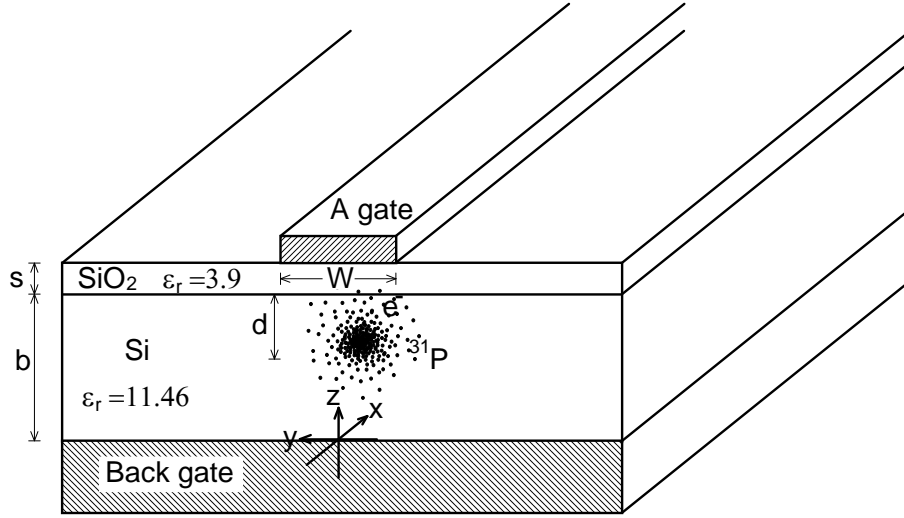


Figure 5.1. The implementation for a solid-state quantum computer using phosphorus ( $^{31}\text{P}$ ) donor electron as the qubit.

The Hamiltonian equation for the valence electron wavefunction under the influence of an applied voltage  $V$  on the A gate is the same as the Hamiltonian for the nuclear-spin qubit. In fact, all the calculation leading to the derivation of perturbed wavefunction and hyperfine interaction constant are identical to those we have used for Kane's nuclear-spin qubit.

When the phosphorus donor electron is in the ground state, its magnetic resonance frequency  $f_0$  is given by (to the second order accuracy)<sup>15,120</sup>

$$hf_0 = g_E \mu_B B + 2A_h + \frac{2A_h^2}{\mu_B B} \quad (5.1)$$

where  $h$  is the Planck's constant,  $g_E \approx 2$  is the  $g$ -factor of the donor electron, and  $B$  is the applied static magnetic field.

Note that previous studies<sup>49,50,59,121</sup> have shown that  $g_E$  is in general not a constant under the action of externally applied electric and magnetic fields, which alter the wavefunctions of the donor electron, resulting in the so-called spin-orbit Stark shift, which changes the value of  $g_E$  from its free-electron value. The relation of the change of  $g_E$  to the applied electric field was found to be quadratic in nature<sup>49,50,59</sup>. Furthermore, the application of an external electric or magnetic field breaks the symmetry of the six minimum valleys of the conduction band of the silicon host, giving rise to the anisotropic values of  $g_E$ <sup>59</sup>. Hence the combined effect of an external electric and magnetic fields on the  $g$ -factor of the donor electron is a complicated one. But as reported in the literature<sup>49,50,121</sup>, the deviation of the electron  $g$ -factor in silicon from the free-electron  $g$ -factor is actually very small, about several parts in  $10^4$ . Given both the static electric and magnetic field strengths in the order of about  $1\text{V}/\mu\text{m}$  and  $0.01\text{ T}$ , respectively, in this study, the spin-orbit Stark shift of  $g_E$  will be very small and therefore not to be taken into account.

## 5.2 Numerical Results

To calculate the perturbation coefficients, we need the knowledge of the potential distribution  $V(\mathbf{r})$  inside the silicon substrate induced by an A gate voltage. Since the electron-spin qubit is exactly the same as nuclear-spin qubit structure we already have the potential distribution data obtained in the previous chapter.

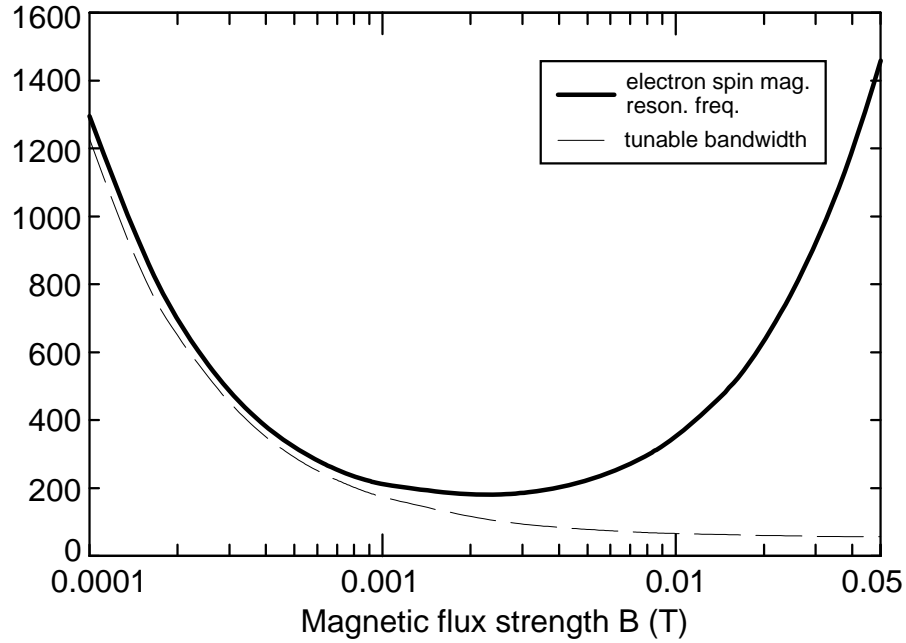


Figure 5.2. The tunable bandwidth  $f_w$  and the electron-spin magnetic resonance frequency  $f_0$  with the static magnetic flux strength  $B$ . The dimensions of the A gate are  $s = 5$  nm,  $b = 100$  nm,  $W = 7$  nm,  $\epsilon_r$  of silicon = 11.46, and  $\epsilon_r$  of silicon dioxide = 3.9. phosphorus atom is at  $x = 20$  nm,  $y = 0$ , and  $z = 50$  nm.

As mentioned in the study of Hill et al.<sup>15</sup>, in order for the detuning frequency of the electron spin to be large enough to achieve an acceptable level of fidelity, the rf magnetic field  $B_{ac}$  must be reduced. We found that this is same for the static magnetic field  $B$  which must be small enough in order to produce a large tunable bandwidth for the magnetic resonant frequency of the electron spin. This is different from the case of using the nuclear spin as the qubit because the Bohr magneton is three orders greater than the nuclear magneton. The relation between the tunable bandwidth  $f_w$  and the static magnetic flux strength  $B$  is illustrated in Fig. 5.2. The dimensions of the A gate (see Fig. 5.1 for the symbol labels) are  $s = 5$  nm,  $b = 100$  nm,  $W = 7$  nm,  $\epsilon_r$  of silicon = 11.46, and  $\epsilon_r$  of silicon dioxide = 3.9. The phosphorus atom is at  $x = 20$  nm,  $y = 0$ , and  $z = 50$  nm (for the coordinate system shown in Fig. 5.1).

The tunable bandwidth  $f_w$  is defined as the 95% of the maximum change in electron-spin magnetic resonant frequency for an A gate voltage change of 0~0.5V. Shown in Fig. 5.2 is also the relation between the electron-spin magnetic resonant frequency  $f_0$  and the static magnetic flux strength  $B$ . It can be seen that both  $f_w$  and  $f_0$  have a rather non-linear relationship with the applied static field  $B$ . To illustrate our study, we choose the operation point at  $B = 0.002$  T. With this field strength, the electron-spin magnetic resonant frequency is  $f_0 = 176.4$  MHz and the tunable bandwidth is  $f_w = 114.0$  MHz. When the static magnetic flux  $B$  is greater than or smaller than 0.002 T, the magnetic resonant frequency  $f_0$  is higher than 176.4 M, leading to a reduced percentage tunable bandwidth. Particularly, when  $B$  is increased above 0.002 T, the magnetic resonant frequency increases rapidly while the tunable bandwidth decreases continuously. For example, when  $B = 2$  T (as suggested for the nuclear-spin qubit operation),  $f_0 = 55986$  MHz and  $f_w = 55$  MHz. The tunable bandwidth is only about 0.1% of the magnetic resonant frequency. This poses a great difficulty in controlling the error in the magnetic resonant frequency  $f_0$ . This finding implies that a large static magnetic field  $B$  may not be a good choice for an electron-spin quantum computer. But on the other hand, a small magnetic field makes it difficult to achieve a complete polarization of the electron spins, and this means that an external method, for example the optical pumping method<sup>122</sup>, to polarize the electron spins is required.

### 5.3 Summary

The electron-spin magnetic resonance frequency of an electron-spin qubit structure proposed for the realization of a quantum computer is rigorously investigated by a numerical method. The potential distribution inside the silicon qubit structure is accurately calculated by an electromagnetic simulation method and the perturbation theory to the second order is formulated to obtain the magnetic resonance frequency of the phosphorus donor electron spin. Our results showed that for the same qubit structure (Si:P) as originally proposed by Kane for the nuclear spin qubit quantum computer, a smaller static magnetic field  $B$  is in favor of producing a wider tunable bandwidth for the magnetic resonance frequency of the electron spin.

**Chapter 6**

**Alternative A-Gate**

**Structures**



After Kane's proposal<sup>9,35</sup> of a scalable solid-state quantum computer based on the nuclear magnetic resonance (NMR) effect, there have been many studies investigating the different factors which affect the performance of the quantum bit (qubit). Kane's original idea consists of rotating the spin of a donor atom (phosphorus) doped inside a silicon substrate by applying a global magnetic field while addressing a particular qubit by applying an electric field through a local gate called the A-gate<sup>9</sup>. Kane's A-gate structure is a typical metallic lead (or a microstrip-line as known in the radio-frequency (RF) community) laid on top of a silicon substrate serving as the gate while the bottom side of the silicon substrate is a metallic layer serving as the ground (or the back-gate). This A-gate structure is so typical, especially for the sake of principle demonstration, that most of the subsequent studies<sup>39,85,106</sup> almost all adopted it. Nevertheless, there are some intrinsic disadvantages in Kane's A-gate that are worth our effort to make improvements. The first issue is its having the ground plate at the bottom of the silicon substrate which is not in common with most other electric-field- or magnetic-field-controlled devices<sup>12,87</sup> which favor the design of putting all the metallic structures (the gate and the ground) on one side of the substrate layer only. One advantage of putting the gate and the ground on one side of the substrate is the ease of fabrication compared to the separate gate and ground structure. Secondly, the presence of a back-gate on the bottom side makes the qubit's performance very sensitive to the substrate thickness, since a change in the substrate thickness will change the position of the back-gate and thus changes the potential profile. Thirdly, because of the second issue, there is in general a restriction being put on the thickness of the silicon substrate and this makes it difficult to integrate other

ancillary devices (such as reading out devices) from below the ground plane or for fabricating heterostructure devices. Finally, as will be shown in this chapter, the original Kane's A-gate structure is not the best one in terms of the efficiency of making use of the gate voltage to control the NMR frequency of the donor atom.

To improve on the original Kane's A-gate structure with respect to the above-mentioned problems, we will introduce two types of new A-gate structures in this study. The first type are the coplanar A-gate structures in which there is no back-gate and the ground lead is laid on the same surface as the A-gate lead. These coplanar structures remove the restriction on the silicon substrate thickness, making it possible for the integration of the A-gate structure with other devices through extending the silicon substrate in the opposite direction. The second type of new structures are called the split-ground A-gate structures in which the ground is split into two halves and deposited on two sides of the A-gate but at a lower level. These structures offer the advantage of a more effective voltage control on the NMR frequency as well as avoiding the restriction on the silicon substrate thickness, same as the coplanar structures. Effective voltage control is an important consideration in nuclear- or electron-spin qubit design as it affects the fidelity of the performance of the quantum computer. In this chapter, we will investigate the design and performance of these two new A-gate structures through a computer-aided numerical simulation method. In the next section, the detailed geometries of these new A-gate structures will be explained, and the numerical and simulation methods mentioned in previous chapters is used to analyze and characterize the performance of these new structures.

## 6.1 The Proposed New A-Gate Structures

The proposed new A-gate structures are shown in Fig. 6.1(a) and Fig. 6.2(a). Fig. 6.1(a) is a coplanar A-gate structure with both the ground lead and the A-gate lead being laid on top of silicon substrate while the donor phosphorus atom is doped under the A-gate lead. The isolation barrier is suggested to be a layer of high dielectric constant silicon-germanium SiGe instead of the usual material SiO<sub>2</sub> whose dielectric constant ( $\epsilon_r=3.9$ ) is much lower than that of Si ( $\epsilon_r=11.46$ ). A specific compound<sup>17</sup> Si<sub>0.5</sub>Ge<sub>0.5</sub> gives a dielectric constant of 13.95, which is more similar to the dielectric constant of silicon. This Si/SiGe system has been suggested before<sup>9,17</sup> for the design of qubit structures. Compared to the Si/SiO<sub>2</sub> system, the advantage of the Si/SiGe system is that a larger portion of the applied A-gate voltage will drop across the silicon substrate rather than the isolation layer due to the similarity of the dielectric constants between Si and SiGe. A possible problem with the Si/SiGe system is the strain imposed on silicon near the interface due to lattice mismatch<sup>9</sup>. Doping the donor away from the interface region can be a possible solution to avoid this problem. For the coplanar A-gate structure shown in Fig. 6.1(a), it has an advantage of easy fabrication and is commonly used in traditional radio-frequency (RF) circuit design or in some recent quantum-dot control circuit design<sup>12,87</sup>. In traditional RF circuit design, the coplanar microstrip structure provides the great advantage that other circuits can be designed freely on the opposite side of the same substrate board. The coplanar A-gate structure in Fig. 5.1 can be modified into several variants as shown in Figs. 6.1(b) and 6.1(c) for different applications.

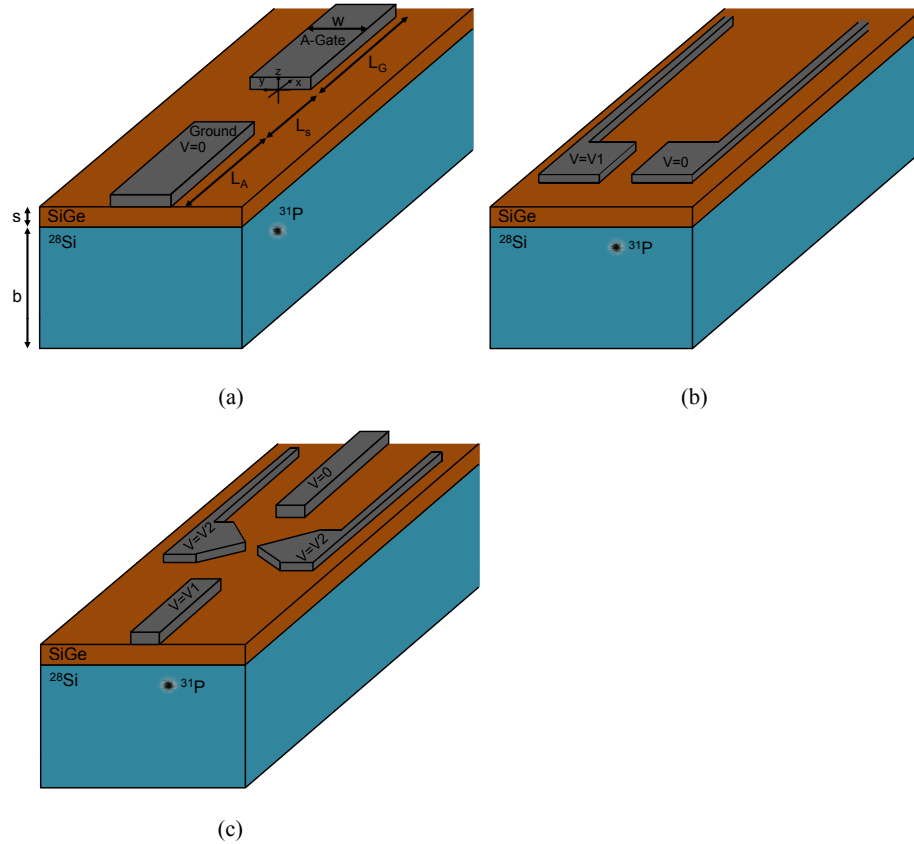


Figure 6.1. The proposed coplanar A-gate structures for the realization of the semiconductor quantum computer based on the nuclear spin of a phosphorus atom doped inside a silicon substrate, (a) the basic structure, (b) & (c) two possible variants.

The structure in Fig. 6.2(a) is a split-ground A-gate structure. The motivation for this structure is that its potential distribution may provide a more effective control on the NMR frequency. Same as the coplanar A-gate structure in Fig. 6.1(a), this A-gate structure can be fabricated from one side of the silicon substrate, thus offering a fabrication convenience and an advantage for downward integration with other structures or devices.

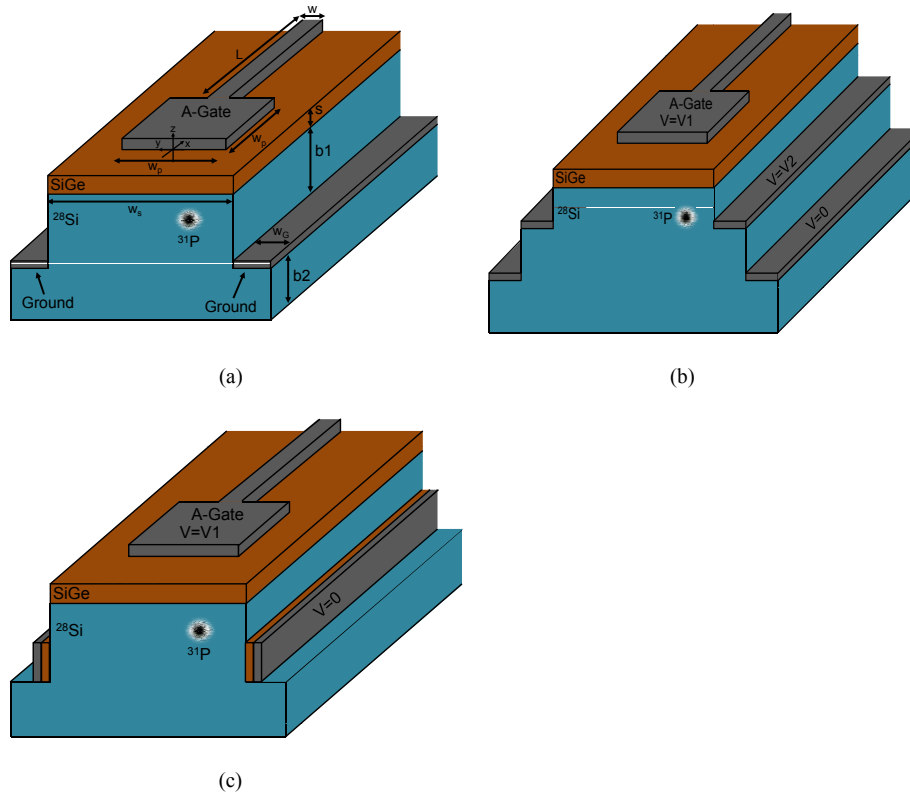


Figure 6.2. The proposed split-ground A-gate structures, (a) the basic structure, (b) & (c) two possible variants.

Instead of on the same plane as the A-gate lead, the ground is split into two halves and lowered to the two sides of the A-gate lead. In this way, the position of the doped donor phosphorus atom is at a higher level as the ground, resulting in a potential distribution under the A-gate lead region being similar to that in the Kane's A-gate structure. Furthermore, the potential distribution under the A-gate lead region is to be controlled by a proper selection of the width of the A-gate lead, as denoted by  $W_p$  in Fig. 6.2(a). Same as the case of the coplanar A-gate structure in Fig. 6.1(a), there are several modified split-ground A-gate structures that can be designed to suit for different applications and they are depicted in Figs. 6.2(b) and 6.2(c). In the

next section, we will compare and contrast the performance of this structure with that of the coplanar structure and Kane's structure.

To design the proposed new A-gate structures and to characterize their performance, we use a computer-aided numerical method as illustrated in previous chapters. First, the exact potential distributions of the A-gate structures inside the silicon substrate are obtained using an electromagnetic simulation tool - CST Electrostatic Solver.

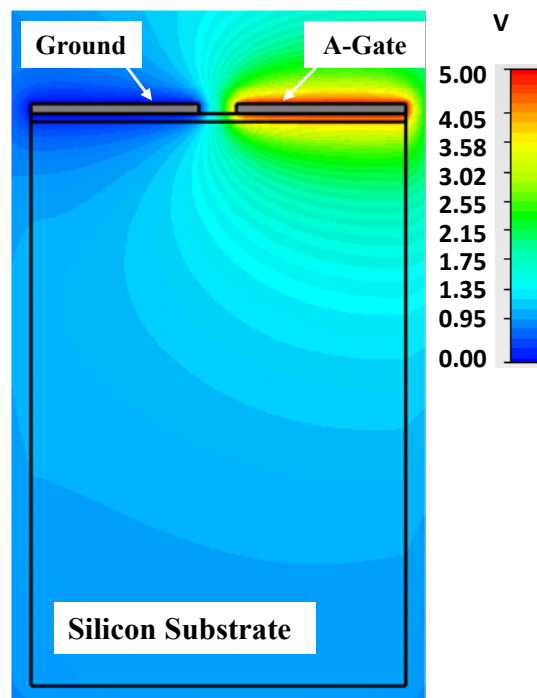


Figure 6.3. A typical 2D potential distribution of the coplanar A-gate structure shown in Fig. 6.1(a).

Note that this EM simulator gives the three-dimensional potential distribution inside the silicon substrate due to an arbitrary voltage excited on the A-gate lead. In this way, any geometric shape of an A-gate structure can be simulated to a very high accuracy, with no need of any kind of unrealistic assumptions.

typical calculated potential distribution by CST Electrostatic Solver for the basic coplanar A-gate structure in Fig. 6.1(a) is shown in Fig. 6.3, which shows a highly non-linear potential inside the silicon substrate.

## **6.2 The Performance of the New Structures**

### **6.2.1 The Potential Distributions**

The potential variation of the coplanar A-gate structure in Fig. 6.1(a) is shown in Fig. 6.4 in comparison with that of Kane's original A-gate structure. These two potential profiles are obtained along a line drawn from the A-gate lead down to the silicon substrate with  $x=40$  nm,  $y=0$ , and  $z=0 \sim -105$  nm, while a static voltage of 5 V is being applied on the A-gate lead. The dimensions of the coplanar A-gate and Kane's A-gate are given in Fig. 6.4. From this figure, it can be seen that the slopes of the two curves are quite different. For example, we can calculate the inverses of the slopes (which is proportional to the magnitude of the electric field intensity  $\mathbf{E}$ ) of these two curves at a position of  $z=-55$  nm down the A-gate lead and they are approximately 0.014 V/nm for the coplanar A-gate and 0.022 V/nm for the Kane's A-gate.

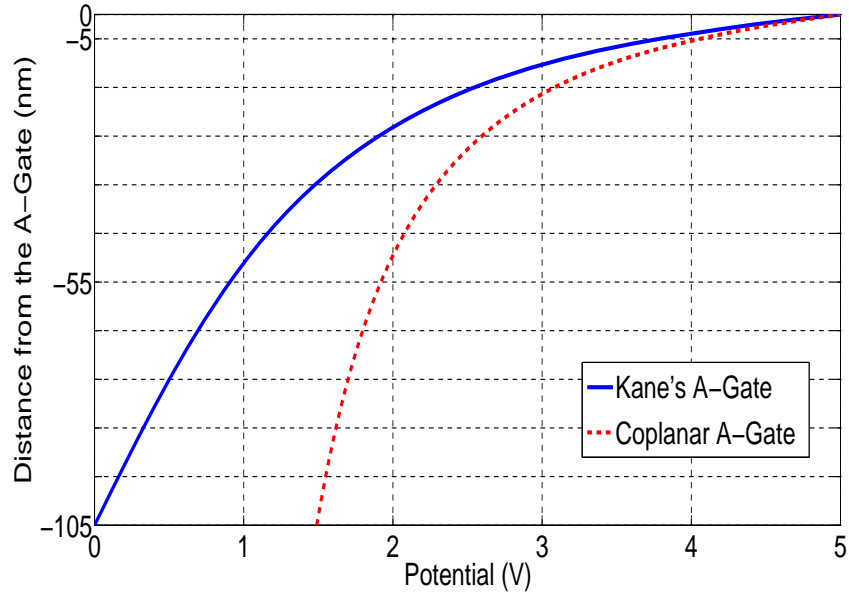


Figure 6.4. The variation of the potential for the coplanar A-gate structure in Fig. 6.1(a) along a line drawn from A-gate lead down to the silicon substrate with  $x=40$  nm,  $y=0$ , and  $z=0 \sim -105$  nm. A static voltage of 5 V is applied on the A-gate lead. The result is compared with that obtained with Kane's A-gate. The dimensions of the A-gate structure are:  $b=600$  nm,  $s=5$  nm,  $w=7$  nm,  $L_G=L_A=70$  nm, and  $L_s=10$  nm. The dielectric constant  $\epsilon_r$  of Si is 11.46 and that of SiGe is 13.95. For Kane's A-gate structure, the dimensions are: substrate thickness=100 nm, A-gate lead width=7 nm, insulating layer ( $\text{Si}_{0.5}\text{Ge}_{0.5}$ ) thickness=5 nm.

That means that the rate of change of the potential for the coplanar A-gate structure is substantially smaller than that for the Kane's A-gate structure. This difference has an impact on the rate of change of the NMR frequency with respect to the applied A-gate voltage, as will be shown later. The reason for this difference can be explained by the 2D potential profile in Fig. 6.3, in which the shift of the ground from the bottom of the substrate to the top of the substrate pushes more energy distribution into the air region above the A-gate structure, leading to a less rapidly decreasing potential distribution inside the silicon.

The potential variation of the split-ground A-gate structure in Fig. 6.2(a) is shown in Fig. 6.5 in comparison with that of Kane's original A-gate structure.



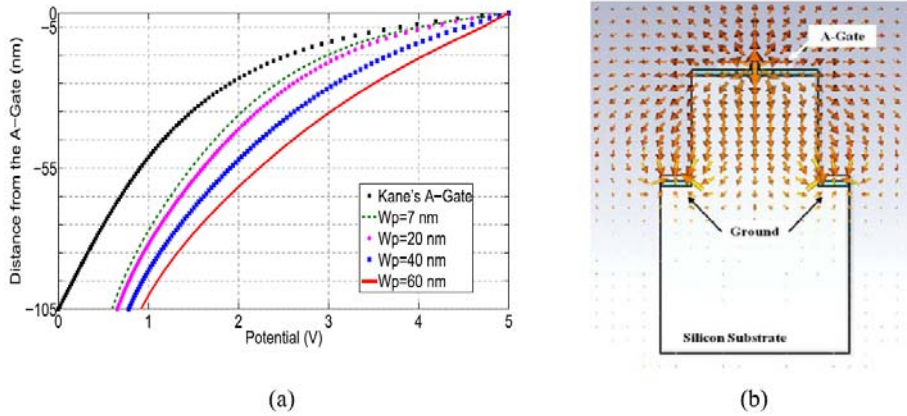


Figure 6.5. The variation of the potential for the split-ground A-gate structure in Fig. 6.2(a). (a) The 1D variation along a line drawn from A-gate lead down to the silicon substrate with  $x = 40$  nm,  $y = 0$ , and  $z = 0 \sim -105$  nm and for different A-gate lead widths  $W_p$ , and (b) the 2D distribution of the electric field on a vertical cross section cut at  $x=40$ nm and for the case of  $W_p=60$  nm. The results are compared with that obtained with Kane's A-gate. The dimensions of the split-ground A-gate structure are:  $b_1=100$  nm,  $s=5$  nm,  $L=100$  nm,  $w=7$  nm,  $L_p=40$  nm,  $W_S=100$  nm,  $W_G=25$  nm, and  $b_2=150$  nm. The dimensions of Kane's A-gate are same as those in Fig. 6.4.

Same as that in Fig. 6.4, the potential profiles in Fig. 6.5 are also obtained along a line drawn from A-gate lead down to the silicon substrate with  $x=40$  nm,  $y=0$ , and  $z=0 \sim -105$  nm, while a static voltage of 5 V is applied on the A-gate lead. The dimensions of the split-ground A-gate and Kane's A-gate are as given in Fig. 6.5. Different from the case of the coplanar structure, the inverses of the slopes of the potential curves in Fig. 6.5 are rather similar (for the case of  $W_p=7$  and 20 nm) to that of Kane's A-gate structure or even greater (for the cases of  $W_p=40$  and 60 nm). For example, the inverse of slope of the potential curve with  $W_p=40$  nm at a position of  $z=-55$  nm is approximately 0.031 V/nm, which is much greater than that of the Kane's A-gate (0.022 V/nm) or that of the coplanar A-gate (0.014 V/nm). This shows that the split-ground A-gate virtually preserves the potential distribution characteristics of Kane's A-gate while at the same time does not restrict the silicon substrate

thickness. This is an advantage for device integrations. Fig. 6.5(b) shows the 2D distribution of the electric field at the plane of  $x=40$  nm and for  $W_p=60$  nm. It shows that the electric field diminished quickly for the substrate region below the split grounds. This is one of the favorable characteristics of this structure because the potential distribution in the donor region (between the A-gate lead and the two split-grounds) is relatively unaffected by the thickness of the substrate below the grounds, providing the condition for downward device integrations as mentioned before. Fig. 6.5(b) further shows that due to the lowered ground levels, electric fields are pulled down to the substrate region between the A-gate lead and the two split grounds. This situation is similar to that of Kane's A-gate structure.

### 6.2.2 The NMR Frequencies

The potential distributions of the two new A-gate structures have significantly different effects on the NMR frequency of the donor. We investigate this by placing a phosphorus donor atom at a position of  $x=40$  nm,  $y=0$  nm, and  $z=-55$  nm under the A-gate lead (unless otherwise stated). A uniform static magnetic field of 2T is applied along the  $z$  direction. Fig.6.6 shows the characteristic curves for the change of NMR frequency with A-gate voltage for the three different A-gate structures (Kane's, the coplanar and the split-ground A-gate structures) operating under different A-gate dimensions or donor positions. First, it can be noticed that the characteristic curve for the coplanar A-gate for the case with donor position at  $z=-55$  nm is very weak compared to that of

Kane's A-gate, indicating that the voltage control on the NMR frequency for this structure is rather ineffective.

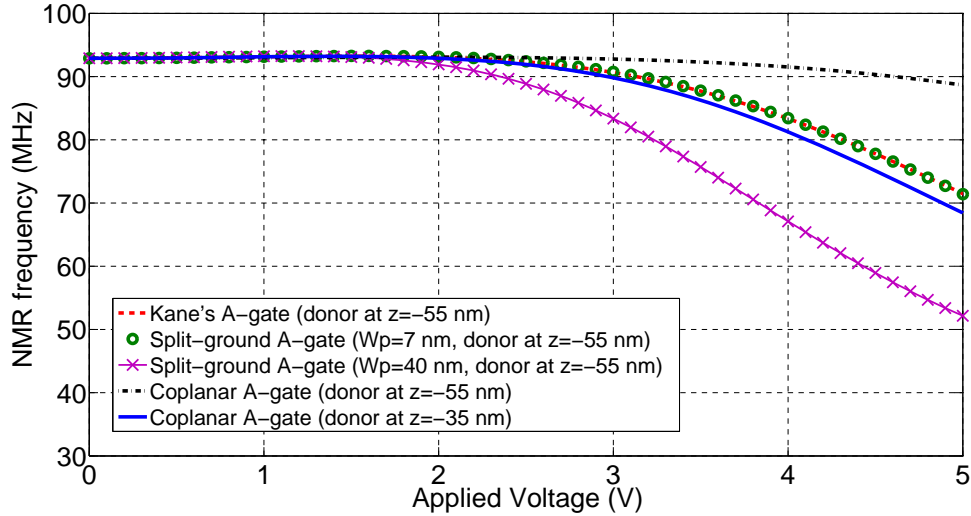


Figure 6.6. The variations of the NMR frequency with applied A-gate voltage for the three different A-gate structures with a uniform static magnetic field of 2T along the  $z$  direction. The dimensions of the coplanar A-gate structure, the split-ground A-gate structure, and Kane's A-gate structure are same as those in Figs. 6.4 and 6.5. For the coplanar A-gate structure, two donor positions are shown (at  $z=-35$  nm and  $-55$  nm). For the split-ground A-gate structure, results for two A-gate widths are shown ( $W_p=7$  nm and 40 nm).

Yet, when we change the donor position to a shallower position at  $z=-35$  nm, it shows that the characteristic curve is similar to or even better than that of Kane's A-gate in terms of effective voltage control. The reason for this difference may be probably due to the somewhat stronger potential variation along the  $x$  and  $y$  directions at the region near  $z=-35$  nm. Thus for the coplanar A-gate structure, the donor position should be chosen closer to the Si/SiGe interface but this may possibly lead to the increased chance of the donor valance electron being in strong interaction with the interface potential of Si/SiGe. It may also cause our current analysis method less accurate for regions near the interface. Next we observe that the curve of the split-ground A-gate structure with  $W_p=7$  nm and donor position at  $z=-55$  nm is almost

identical to that of Kane's A-gate structure, suggesting the more effective voltage control on the NMR frequency by using this A-gate. Further, when the width of the A-gate lead  $W_p$  is increased to 40 nm, the characteristic curve of the split-ground A-gate structure shows a much stronger voltage control on the NMR frequency than Kane's A-gate. For example, when the A-gate voltage is 5V, the NMR frequency is shifted to 52.5 MHz by the split-ground A-gate and to only 72 MHz by Kane's A-gate. This confirms our earlier potential calculations which indicate that the split-ground A-gate with a  $W_p=40$  nm has a much steeper voltage slope (0.031 V/nm) than that of the Kane's A-gate (0.022 V/nm).

The comparison in Fig. 6.6 suggests that the split-ground A-gate is a more effective design than either Kane's A-gate or the coplanar A-gate. In Fig. 6.7, we further investigate the effectiveness of the split-ground A-gate with varying dimensions. Fig. 6.7(a) illustrates the change of NMR frequency with the applied A-gate voltage with different substrate heights,  $b_1$ , above the ground. The other dimensions are same as those in Fig. 6.5. From the five characteristic curves shown, it can be seen that when  $b_1$  decreases from 120 nm to 80 nm, the characteristic curve bends further downward, indicating a more effective voltage control on the NMR frequency. For example, when the A-gate voltage is 5V, the NMR frequency changes from 57 MHz to 50 MHz (a 11% change) if the  $b_1$  changes from 120 nm to 80 nm. However, a further decrease in the substrate height from 80 nm to 50 nm actually does not favor a more effective voltage control of the NMR frequency but rather causes a rapid loss of control, with the NMR frequency increases from 50 MHz to 63 MHz at an A-gate voltage of 5V, i.e., a 26% increase. Note that the phosphorus donor

is at a position of 55 nm down the A-gate lead (50 nm from the silicon substrate surface). A substrate height too close to the donor depth inside the substrate (50 nm) will have an adverse effect on the effectiveness of the A-gate voltage control. This can be seen from Fig. 6.5(b) in which the electric field distribution indicates a rather weak electric field region at around the ground level. Thus it shows that, for the split-ground A-gate structure, the substrate height has to be substantially greater the donor depth in order to achieve an effective voltage control on the NMR frequency.

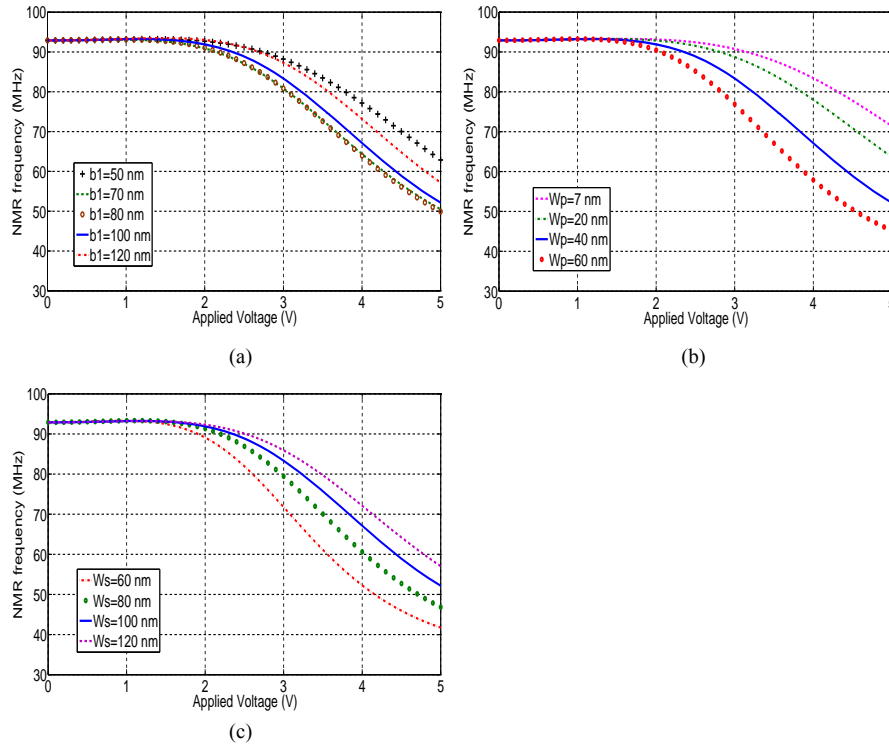


Figure 6.7. The variations of the NMR frequency with applied voltage for the split-ground A-gate structure with a uniform static magnetic field of 2T along the  $z$  direction, (a) for different substrate heights,  $b_1$ , above the ground, (c) for different widths,  $W_p$ , of A-gate lead, and (c) for different substrate widths,  $W_s$ . The dimensions of the split-ground A-gate structure are same as those in Fig. 6.5 except the ones being varied. Donor position is at  $z=-55$  nm.

In Fig. 6.7(b), the characteristic curves are shown with the width of the A-gate lead,  $W_p$ . It can be seen that  $W_p$  has a rather significant effect on the voltage control of the NMR frequency. As  $W_p$  increases from 7 nm to 60 nm, the characteristic curve continuously bends downward, indicating a more effective voltage control on the NMR frequency. This is not difficult to understand as an increase in the width of the A-gate lead will directly reduce the "fringing field effect" and pushes more electrical energy into the silicon substrate. Thus a wider A-gate lead favors a more effective voltage control on the NMR frequency. However, a wider A-gate lead also increases the degree of coupling with adjacent gates and is in general not in favor of increasing the packing density of A-gates on a certain fixed area. In Fig. 6.7(c), the characteristic curves are plotted with different substrate widths,  $W_s$ . It can be seen that as  $W_s$  decreases, the characteristic curve bends downwards, indicating an increasing effectiveness of the voltage control. For example, when the applied A-gate is fixed at 5V, the NMR frequency shifts from 57 MHz to 41 MHz as  $W_s$  decreases from 120 nm to 60 nm. It should be noted that a smaller  $W_s$  is in favor of achieving a higher packing density of A-gates. Another important parameter to study is the effect of the thickness of the supporting substrate block,  $b_2$ , extended beyond the ground for the split ground A-gate structure. This will tell us whether the supporting substrate can be used to grow other devices/structures for device integration. Our calculation results show that changing this dimension ( $b_2$ ) from 10 nm to 100 nm causes a 5% change in the NMR frequency while for values of  $b_2$  greater than 100 nm the change is less than 1%, showing that the NMR frequency is rather insensitive to  $b_2$  once it is somewhat greater than about 50 nm.

### 6.2.3 The Effect of Adjacent Qubits

For the integration of qubit structures in a scalable realization scheme of a quantum computer, it is important to know the effect of applying a voltage to the adjacent qubits on their NMR frequencies. For this, we have studied the additional shift in NMR frequency of a qubit due to the application of a control voltage on an adjacent qubit. This is the worse case studied among other possible situations due to the proximity coupling effect between adjacent qubits. As shown in Fig. 8, we consider a three-qubit system for both Kane's A-gate structure (Fig. 6.8(a)) and the split-ground A-gate structure (Fig. 6.8(b)). The dimensions of the A-gate structures are given in Fig. 6.8. In both structures, a 5 V is applied to all three qubits and the separation between adjacent qubits is set to  $D=100$  nm.

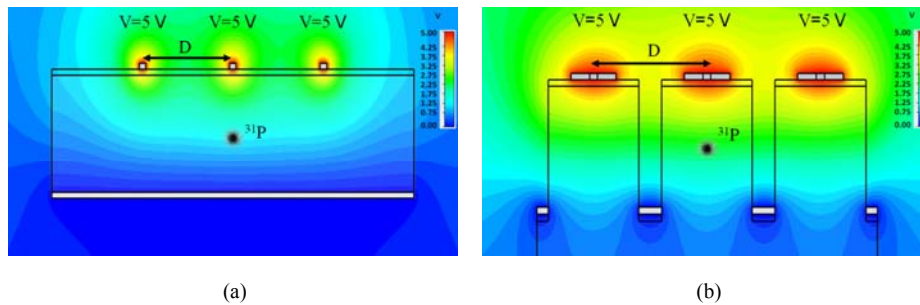


Figure 6.8. The 2D potential profiles for three A-gate structures with two end gates being excited, (a) Kane's A-gate structure, and (b) the split-ground A-gate structure. The separation between adjacent phosphorus donors ( $^{31}\text{P}$ ) are  $D=100$  nm for both cases, and the donors are at a distance of 50 nm from the A-gate leads. The dimensions for the split-ground A-gate structure are:  $b_1=100$  nm,  $b_2=100$  nm,  $W=7$  nm,  $s=5$  nm,  $W_p=40$  nm,  $W_s=80$  nm,  $W_G=20$  nm, and  $L=100$  nm. The dimensions for Kane's A-gate structure are same as those in Fig. 6.4.

Some previous studies<sup>116</sup> also suggested this separation for the design of adjacent qubits in Kane's A-gate structure. Ideally (i.e., with no coupling effect), the NMR frequencies of an isolated Kane's A-gate is 72 MHz and that of an isolated split-ground A-gate is 47 MHz. However, our calculation shows that the actual NMR frequency for the middle qubit of Kane's A-gate structure in Fig. 6.8(a) is shifted to 57 MHz while that for the split-ground A-gate, the NMR frequency of the middle qubit is shifted to 44 MHz. It can be seen that the frequency shift in Kane's A-gate structure is about 21% but that for the split-ground A-gate structure is only about 6%. This shows that the split-ground A-gate structure is a much better design in terms of minimizing the coupling effect from adjacent qubits. Note that a too large shift in the NMR frequency will make it difficult to design for a single NMR frequency for the operation of a semiconductor scalable quantum computer. On the other hand, the rather isolated operation characteristic of the split-ground A-gate structure also allows it to have a smaller adjacent qubit separation so as to increase the number of qubits fabricated on a fixed substrate area. However, modern electronic devices favor miniaturization. If an even smaller qubit separation is required, the effect due to the adjacent qubit will be intolerable. Under such a situation, a compensation technique as demonstrated by Kandasemy et al<sup>65</sup> can be used. In Kandasemy's study<sup>65</sup>, the strong cross-talk effect between closely placed (20-30 nm apart) adjacent gates was shown to be limited by the application of compensation voltages to a series of gates. Later it was shown that this compensation voltage technique was more effective if applied to a quasi-two-dimensional (2D) donor-based A-gate architecture as proposed by Hollenberg et al<sup>16</sup>.



Note that notwithstanding the above results being obtained from a theoretical study, the realization of the suggested alternative A-gate structures is made possible by the advances in the silicon fabrication methods. For example, using the ion implantation method, donor atoms can be positioned inside a silicon substrate even at the level of single donors<sup>116</sup>. Scanning probe techniques<sup>123</sup> can be utilized for the fabrication of donor arrays or A-gate arrays. More recent experimental techniques such as the single electron spin manipulation<sup>124</sup>, the experimental creation of the electron-nuclear spin-pair entanglement<sup>125</sup>, and the accurate fabrication of a single-atom transistor<sup>126</sup> further add to the possibility of realizing the proposed A-gate structures with better performance.

### **6.3 Summary**

Two new A-gate structures for the realization of the qubit for the semiconductor quantum computer are proposed and investigated rigorously by the previously introduced numerical simulation method. The coplanar A-gate structure has the advantage of easy fabrication but it offers only a relatively weak voltage control over the nuclear magnetic resonance (NMR) frequency of the donor atom. However, this short-coming can be overcome by doping the donor closer to the substrate interface. The split-ground A-gate structure, on the other hand, produces a similar potential distribution as that of the original Kane's A-gate structure and provides a relatively stronger control over the NMR frequency of the donor atom. Both structures have the advantage of allowing device integration or heterostructure fabrication from below the

silicon substrate. All simulations are carried out by a rigorous electromagnetic simulation tool plus a quantum mechanical perturbation theory.

**Chapter 7**

**Conclusions and Future**

**Works**

## 7.1 Conclusions

In this dissertation, the NMR frequency of a single qubit structure of Kane's solid-state quantum computer is investigated by using a second-order perturbation theory. With higher-order excited states (up to  $3d$  modes) included in our calculation, the perturbation frequencies and energies are obtained numerically. To compute for arbitrary A-gate geometries, the perturbation potential inside the qubit structure is determined through an electromagnetic simulation method. Calculations show that the potential distributions for realistic A-gate geometries are far from linear ones. Our method can be used to engineer A-gate structures of any shapes or geometries. We also investigate an alternative A-gate structure using SiGe as the insulation barrier. Our study shows that this A-gate structure offers a much more efficient utilization of the control voltage than the original A-gate structure using SiO<sub>2</sub> as the insulation barrier.

Furthermore, we have determined by using the same rigorous numerical method the electron-spin magnetic resonance frequency of an electron-spin qubit structure (Si:P) proposed for the realization of a quantum computer. Again, the perturbation theory to the second order was utilized to obtain the magnetic resonance frequency of the donor electron spin using the potential distribution inside the silicon qubit. Our results showed that for the same qubit structure as originally proposed by Kane for the nuclear spin quantum computer, a smaller static magnetic field  $B$  was in favor of producing a wider tunable bandwidth for the magnetic resonance frequency of the electron spin. Finally, two new A-gate structures for the realization of the qubit for the semiconductor quantum computer are proposed and investigated rigorously by

the previously introduced numerical method. The coplanar A-gate structure has the advantage of easy fabrication but it offers only a relatively weak voltage control over the NMR frequency of the donor atom. However, this short-coming is shown to be overcome by doping the donor closer to the substrate interface. The split-ground A-gate structure, on the other hand, produces a similar potential distribution as that of the original Kane's A-gate structure and provides a relatively stronger control over the NMR frequency of the donor atom. Both structures have the advantage of allowing device integration or heterostructure fabrication from below the silicon substrate. All simulations in this study are carried out by a rigorous electromagnetic simulation tool plus a quantum mechanical perturbation theory. The proposed new A-gate structures are realistic and practical for the implementation as a semiconductor qubit operation unit or for the demonstration of a general spintronics device design optimized for the electromagnetic field control.

## **7.2 Future Works**

### **7.2.1 More Efficient A-gate Structures**

As mentioned before, using the CST 3D simulation software we can simulate arbitrary A-gate geometries for obtaining a more linear potential distribution inside the qubit structure in order to effectively control the NMR frequency of the phosphorus donor electron. This is necessary because using the conventional gate structure causes a large portion of the applied voltage to drop across the insulating layer rather than the silicon substrate. By improving the efficiency in this sense, we can reduce the external applied voltage which

itself is a source of decoherence for the quantum system. Although two new structures have been proposed in this dissertation, it is worth the effort to perform further investigation on the A-gate geometry to improve the efficiency of the applied voltage in controlling the hyperfine behavior of the donor electron.

### **7.2.2 Different Materials for Insulating Layer**

As discussed in Chapter 4 and 6, using SiGe instead of SiO<sub>2</sub> (in the insulating layer) improves the efficiency of potential distribution by around 20%. An important step towards the realization of an efficient qubit is to find alternative materials to be used as the insulating layer. The new material should on one hand be more efficient as discussed, and on the other hand can be engineered easily and be grown on top of the silicon substrate using the present Silicon technologies. Similar to the gate geometry, an appropriate insulating material will help to decrease the decoherence factor by reducing the gate voltage.

### **7.2.3 Multi-Qubit Structures and Exchange Gates**

For realizing a real quantum computer, we should be able to integrate several qubits together. As discussed in chapter 6, certain precautions should be taken into account in order to avoid the unwanted interaction between the adjacent qubits. Although new A-gate geometries, such as the split-ground structures proposed in chapter 6, show a better degree of isolation compared to conventional qubits, it is still worth the effort to search for more efficient A-gate designs to improve the coherence of the quantum system. New

decoherence agents, finding the appropriate distance between two adjacent qubits, keeping the conditions as steady as possible in the multi-qubit system, and fabrication issues for an ideal control over the electron-mediated interactions are some of the important challenges in designing a multi-qubit operational system. Apart from multi-qubit structures for performing single qubit operations, we need to design exchange gates to realize two-qubit operational quantum gates. This should be further studied using exchange interaction concepts for controlling the interaction between two donor atoms and designing the corresponding exchange gates. By designing the exchange gates (J-gate), together with the multi-A-gate structures, we are able to construct a quantum computer capable of processing quantum information algorithms.

#### **7.2.4 Further Study on Perturbation Theory and Other Alternative Theories to Find the Wavefunction of the Donor Electron**

For many years, perturbation theory has been a well known solution to find the wavefunction of the donor electron in the presence of an external perturbation i.e. applied voltage. Since there hasn't been any report on the experimental results of NMR spin-based quantum bits, it is still a matter of debate that which of the proposed methods is more reliable in predicting the wavefunction of the donor electron. While modifying the perturbation theory to include more hydrogenic orbitals may help to more accurately predict the donor electron wavefunction, it is worth to try other approaches such as variational methods, the tight-binding calculations, the density functional theory (DFT), and the numerical diagonalization of the donor Hamiltonian.

### **7.2.5 Further Study on Determinant Factors Affecting the Wavefunction of the Donor Electron**

As discussed in chapter 6, many geometrical parameters are involved in the operation conditions of a qubit. Due to rather sensitive nature of a quantum computer, extensive care should be taken in designing qubit A-gate or J-gate geometries to avoid any instability in the operation and efficiency of the qubit. An important factor in determining the efficiency of hyperfine interactions is the doping depth of the donor atom. On one hand, reducing this distance may provide a greater portion of the external applied voltage to the donor atom which in turn increases the efficiency of controlling the hyperfine interaction. On the other hand, bringing the insulator interface too close to the donor atom will affect the electron cloud and wavefunction of the donor atom and the conventional perturbation theory does not hold anymore, not to mention the possibility of potential decoherence factors that may appear in the close proximity of the insulating layer. Therefore, other approaches such as variational methods can be considered to study the behavior of donor electron cloud in the vicinity of an interface.



## Bibliography

- 1 M. A. Nielsen and I. L. Chuang, Cambridge: Cambridge University Press **2**,  
23 (2000).
- 2 S. Lloyd, Science **261**, 1569 (1993).
- 3 A. M. Turing, Proceedings of the London Mathematical Society **2**, 544  
(1938).
- 4 G. E. Moore, Proceedings of the IEEE **86**, 82 (1998).
- 5 D. Deutsch and R. Jozsa, Proceedings of the Royal Society of London. Series  
A: Mathematical and Physical Sciences **439**, 553 (1992).
- 6 P. W. Shor, in *Algorithms for quantum computation: discrete logarithms and  
factoring*, 1994 (IEEE), p. 124.
- 7 F. A. Zwanenburg, A. S. Dzurak, A. Morello, M. Y. Simmons, L. C.  
Hollenberg, G. Klimeck, S. Rogge, S. N. Coppersmith, and M. A. Eriksson,  
arXiv preprint arXiv:1206.5202 (2012).
- 8 T. Ladd, F. Jelezko, R. Laflamme, Y. Nakamura, C. Monroe, and J. O'Brien,  
Nature **464**, 45 (2010).
- 9 B. E. Kane, Nature **393**, 133 (1998).
- 10 D. P. DiVincenzo, Physical Review A **51**, 1015 (1995).
- 11 J. Elzerman, R. Hanson, L. W. Van Beveren, B. Witkamp, L. Vandersypen,  
and L. P. Kouwenhoven, Nature **430**, 431 (2004).
- 12 F. Koppens, C. Buizert, K.-J. Tielrooij, I. Vink, K. Nowack, T. Meunier, L.  
Kouwenhoven, and L. Vandersypen, Nature **442**, 766 (2006).
- 13 F. Koppens, J. Folk, J. Elzerman, R. Hanson, L. W. Van Beveren, I. Vink,  
H.-P. Tranitz, W. Wegscheider, L. P. Kouwenhoven, and L. Vandersypen,  
Science **309**, 1346 (2005).
- 14 R. De Sousa, J. Delgado, and S. D. Sarma, Physical Review A **70**, 052304  
(2004).
- 15 C. D. Hill, L. Hollenberg, A. Fowler, C. Wellard, A. Greentree, and H.-S.  
Goan, Physical Review B **72**, 045350 (2005).
- 16 L. C. L. Hollenberg, A. D. Greentree, A. G. Fowler, and C. J. Wellard,  
Physical Review B **74**, 045311 (2006).
- 17 R. Vrijen, E. Yablonovitch, K. Wang, H. W. Jiang, A. Balandin, V.  
Roychowdhury, T. Mor, and D. DiVincenzo, Physical Review A **62**, 012306  
(2000).
- 18 M. Friesen, P. Rugheimer, D. E. Savage, M. G. Lagally, D. W. Van Der  
Weide, R. Joynt, and M. A. Eriksson, Physical Review B **67**, 121301 (2003).
- 19 L. Kouwenhoven, T. Oosterkamp, M. Danoesastro, M. Eto, D. Austing, T.  
Honda, and S. Tarucha, Science **278**, 1788 (1997).
- 20 D. Ali and H. Ahmed, Applied Physics Letters **64**, 2119 (1994).
- 21 D. Paul, J. Cleaver, H. Ahmed, and T. E. Whall, Applied Physics Letters **63**,  
631 (1993).
- 22 F. Simmel, R. Blick, J. Kotthaus, W. Wegscheider, and M. Bichler, Physical  
Review Letters **83**, 804 (1999).
- 23 W. Lim, F. Zwanenburg, H. Huebl, M. Mottonen, K. Chan, A. Morello, and  
A. Dzurak, Applied Physics Letters **95**, 242102 (2009).
- 24 C. Simmons, M. Thalakulam, N. Shaji, L. J. Klein, H. Qin, R. Blick, D.  
Savage, M. Lagally, S. Coppersmith, and M. Eriksson, arXiv preprint  
arXiv:0710.3725 (2007).
- 25 F. Zwanenburg, A. Van Loon, G. Steele, C. van Rijmenam, T. Balder, Y.  
Fang, C. Lieber, and L. Kouwenhoven, Journal of Applied Physics **105**,  
124314 (2009).

- 26 M. G. Borselli, R. S. Ross, A. A. Kiselev, E. T. Croke, K. S. Holabird, P. W.  
Deelman, L. D. Warren, I. Alvarado-Rodriguez, I. Milosavljevic, and F. C.  
27 Ku, *Applied Physics Letters* **98**, 123118 (2011).  
W. Lim, C. Yang, F. Zwanenburg, and A. Dzurak, *Nanotechnology* **22**,  
28 335704 (2011).  
M. Thalakulam, C. Simmons, B. Rosemeyer, D. Savage, M. Lagally, M.  
Friesen, S. Coppersmith, and M. Eriksson, *Applied Physics Letters* **96**,  
183104 (2010).  
29 B. Maune, M. Borselli, B. Huang, T. Ladd, P. Deelman, K. Holabird, A.  
Kiselev, I. Alvarado-Rodriguez, R. Ross, and A. Schmitz, *Nature* **481**, 344  
(2012).  
30 M. Fuechsle, S. Mahapatra, F. Zwanenburg, M. Friesen, M. Eriksson, and M.  
Y. Simmons, *Nature Nanotechnology* **5**, 502 (2010).  
31 G. Lansbergen, R. Rahman, C. Wellard, I. Woo, J. Caro, N. Collaert, S.  
Biesemans, G. Klimeck, L. Hollenberg, and S. Rogge, *Nature Physics* **4**, 656  
(2008).  
32 M. Fuechsle, J. A. Miwa, S. Mahapatra, H. Ryu, S. Lee, O. Warschkow, L. C.  
Hollenberg, G. Klimeck, and M. Y. Simmons, *Nature Nanotechnology* **7**, 242  
(2012).  
33 A. Morello, J. J. Pla, F. A. Zwanenburg, K. W. Chan, K. Y. Tan, H. Huebl,  
M. Möttönen, C. D. Nugroho, C. Yang, and J. A. van Donkelaar, *Nature* **467**,  
687 (2010).  
34 E. Nordberg, G. Ten Eyck, H. Stalford, R. Muller, R. Young, K. Eng, L.  
Tracy, K. Childs, J. Wendt, and R. Grubbs, *Physical Review B* **80**, 115331  
(2009).  
35 B. E. Kane, *Scalable Quantum Computers*, 253 (2000).  
36 H.-S. Goan, *International Journal of Quantum Information* **3**, 27 (2005).  
37 A. Larionov, L. Fedichkin, A. Kokin, and K. Valiev, *Nanotechnology* **11**, 392  
(2000).  
38 C. Wellard and L. Hollenberg, *Journal of Physics D: Applied Physics* **35**,  
2499 (2002).  
39 L. Kettle, H. S. Goan, S. Smith, C. Wellard, L. Hollenberg, and C. Pakes,  
*Physical Review B* **68** (2003).  
40 G. Smit, S. Rogge, J. Caro, and T. Klapwijk, *Physical Review B* **68**, 193302  
(2003).  
41 G. Smit, S. Rogge, J. Caro, and T. Klapwijk, *Physical Review B* **70**, 035206  
(2004).  
42 W. Kohn, F. Seitz, and D. Turnbull, *Academic*, New York **257** (1957).  
43 A. S. Martins, T. B. Boykin, G. Klimeck, and B. Koiller, *Physical Review B*  
**72**, 193204 (2005).  
44 A. S. Martins, R. B. Capaz, and B. Koiller, *Physical Review B* **69**, 085320  
(2004).  
45 M. Friesen, *Physical Review Letters* **94**, 186403 (2005).  
46 A. Debernardi, A. Baldereschi, and M. Fanciulli, *Physical Review B* **74**  
(2006).  
47 M. J. Calderón, A. Saraiva, B. Koiller, and S. Das Sarma, *Journal of Applied*  
*Physics* **105**, 122410 (2009).  
48 C. Wellard and L. Hollenberg, *Physical Review B* **72** (2005).  
49 R. Rahman, C. J. Wellard, F. R. Bradbury, M. Prada, J. H. Cole, G. Klimeck,  
and L. C. L. Hollenberg, *Physical Review Letters* **99**, 036403 (2007).  
50 F. R. Bradbury, A. M. Tyryshkin, G. Sabouret, J. Bokor, T. Schenkel, and S.  
A. Lyon, *Physical Review Letters* **97**, 176404 (2006).  
51 U. Gerstmann, *physica status solidi (b)* **248**, 1319 (2011).  
52 H. Overhof and U. Gerstmann, *Physical Review Letters* **92** (2004).

53 R. Rahman, G. Lansbergen, S. Park, J. Verduijn, G. Klimeck, S. Rogge, and  
 54 L. Hollenberg, *Physical Review B* **80** (2009).  
 55 M. Calderón, B. Koiller, and S. Das Sarma, *Physical Review B* **77** (2008).  
 56 Y. Hao, A. Djotyan, A. Avetisyan, and F. Peeters, *Physical Review B* **80**  
 57 (2009).  
 58 J. Ivey and R. Miehler, *Physical Review B* **11**, 822 (1975).  
 59 J. Ivey and R. Miehler, *Physical Review B* **11**, 849 (1975).  
 60 S. Park, R. Rahman, G. Klimeck, and L. Hollenberg, *Physical Review Letters*  
 61 **103** (2009).  
 62 R. Rahman, S. Park, T. Boykin, G. Klimeck, S. Rogge, and L. Hollenberg,  
 63 *Physical Review B* **80** (2009).  
 64 A. Thilderkvist, M. Kleverman, G. Grossmann, and H. Grimmeiss, *Physical*  
 65 *Review B* **49**, 14270 (1994).  
 66 L. Hollenberg, A. Dzurak, C. Wellard, A. Hamilton, D. Reilly, G. Milburn,  
 67 and R. Clark, *Physical Review B* **69** (2004).  
 68 X. Hu and S. Das Sarma, *Physical Review B* **71** (2005).  
 69 R. Rahman, S. H. Park, G. Klimeck, and L. C. Hollenberg, *Nanotechnology*  
 70 **22**, 225202 (2011).  
 71 C. Wellard, L. Hollenberg, and S. Das Sarma, *Physical Review B* **74** (2006).  
 72 G. Kandasamy, C. Wellard, and L. Hollenberg, *Nanotechnology* **17**, 4572  
 73 (2006).  
 74 A. Fang, Y. Chang, and J. Tucker, *Physical Review B* **66** (2002).  
 75 A. Abragam and L. Hebel, *American Journal of Physics* **29**, 860 (1961).  
 76 D. Freude, *Spectroscopy for Physicists* (universität Leipzig, 2006).  
 77 C. A. Fyfe, *Solid state NMR for chemists* (Guelph, Ont.: CFC Press, 1983).  
 78 M. H. Levitt, *Spin dynamics* (John Wiley & Sons, 2013).  
 79 R. Freeman, (1987).  
 80 D. G. Cory, R. Laflamme, E. Knill, L. Viola, T. Havel, N. Boulant, G. Boutis,  
 81 E. Fortunato, S. Lloyd, and R. Martinez, *Fortschritte der Physik* **48**, 875  
 82 (2000).  
 83 C. I. Pakes, C. J. Wellard, D. N. Jamieson, L. C. L. Hollenberg, S. Prawer, A.  
 84 S. Dzurak, A. R. Hamilton, and R. G. Clark, *Microelectronics Journal* **33**,  
 85 1053 (2002).  
 86 M. Lu, D. V. Melnikov, I. J. Chung, and J. P. Leburton, *Journal of Applied*  
 87 *Physics* **98**, 093704 (2005).  
 88 H. Hui, *Physical Review B* **74** (2006).  
 89 T. Castner, *Physical Review B* **77** (2008).  
 90 T. Ning and C. Sah, *Physical Review B* **4**, 3468 (1971).  
 91 J. Luttinger and W. Kohn, *Physical Review* **97**, 869 (1955).  
 92 W. Kohn and J. Luttinger, *Physical Review* **97**, 883 (1955).  
 93 W. Kohn and J. Luttinger, *Physical Review* **98**, 915 (1955).  
 94 R. Aggarwal and A. Ramdas, *Phys. Rev* **140**, A1246 (1965).  
 95 H. Hui, *Solid State Communications* (2012).  
 96 <http://www.cst.com/Content/Products/EMS/SolverElectrostatics.aspx>.  
 97 D.-B. Tsai, P.-W. Chen, and H.-S. Goan, *Physical Review A* **79**, 060306  
 98 (2009).  
 99 L. Hollenberg, C. Wellard, C. Pakes, and A. Fowler, *Physical Review B* **69**  
 (2004).  
 L. M. Kettle, H. S. Goan, S. C. Smith, L. C. L. Hollenberg, and C. J. Wellard,  
*Journal of Physics: Condensed Matter* **16**, 1011 (2004).  
 M. Mitic, M. C. Cassidy, K. D. Petersson, R. P. Starrett, E. Gauja, R.  
 Brenner, R. G. Clark, A. S. Dzurak, C. Yang, and D. N. Jamieson, *Applied*  
*Physics Letters* **89**, 013503 (2006).  
 A. Baldereschi, *Physical Review B* **1**, 4673 (1970).  
 S. T. Pantelides and C. Sah, *Physical Review B* **10**, 621 (1974).

90 K. Shindo and H. Nara, Journal of the Physical Society of Japan **40**, 1640  
(1976).

91 A. Martins, R. Capaz, and B. Koiller, Physical Review B **69** (2004).

92 H. Mirzaei and H. T. Hui, Journal of Applied Physics **108**, 094503 (2010).

93 K. Li, K. Atsuki, and T. Hasegawa, Microwave Theory and Techniques,  
IEEE Transactions on **45**, 2 (1997).

94 R. F. Harrington and J. L. Harrington, *Field computation by moment methods*  
(Oxford University Press, 1996).

95 D. J. Griffiths and E. G. Harris, *Introduction to quantum mechanics*, Vol. 2  
(Prentice Hall, 1995).

96 T. Weiland, Archiv Elektronik und Uebertragungstechnik **31**, 116 (1977).

97 T. Weiland, International Journal of Numerical Modelling: Electronic  
Networks, Devices and Fields **9**, 295 (1996).

98 T. Weiland, in *RF&Microwave Simulators--From Component to System*  
*Design*, 2003 (IEEE), p. 591.

99 T. Itoh, R. Mittra, and R. Ward, Microwave Theory and Techniques, IEEE  
Transactions on **20**, 847 (1972).

100 A. Skinner, M. Davenport, and B. Kane, Physical Review Letters **90** (2003).

101 M. Calderón, B. Koiller, X. Hu, and S. Das Sarma, Physical Review Letters  
**96** (2006).

102 M. J. Calderón, B. Koiller, and S. Das Sarma, Physical Review B **75** (2007).

103 D. McCamey, G. Morley, H. Seipel, L. Brunel, J. van Tol, and C. Boehme,  
Physical Review B **78** (2008).

104 J. Hodges, J. Yang, C. Ramanathan, and D. Cory, Physical Review A **78**  
(2008).

105 B. Koiller, X. Hu, and S. Das Sarma, Physical Review Letters **88** (2001).

106 C. Wellard, L. Hollenberg, F. Parisoli, L. Kettle, H. S. Goan, J. McIntosh,  
and D. Jamieson, Physical Review B **68** (2003).

107 A. Fang, Y.-C. Chang, and J. Tucker, Physical Review B **72** (2005).

108 L. Kettle, H.-S. Goan, and S. Smith, Physical Review B **73** (2006).

109 Q. Li, Ł. Cywiński, D. Culcer, X. Hu, and S. Das Sarma, Physical Review B  
**81** (2010).

110 C. Tahan, M. Friesen, and R. Joynt, Physical Review B **66** (2002).

111 V. Privman, D. Mozyrsky, and I. D. Vagner, Computer Physics  
Communications **146**, 331 (2002).

112 C. Hill and H.-S. Goan, Physical Review A **70** (2004).

113 W. Witzel and S. Das Sarma, Physical Review B **74** (2006).

114 D. Suter and T. S. Mahesh, J Chem Phys **128**, 052206 (2008).

115 J. O'Brien, S. Schofield, M. Simmons, R. Clark, A. Dzurak, N. Curson, B.  
Kane, N. McAlpine, M. Hawley, and G. Brown, Physical Review B **64**  
(2001).

116 T. Schenkel, A. Persaud, S. J. Park, J. Nilsson, J. Bokor, J. A. Liddle, R.  
Keller, D. H. Schneider, D. W. Cheng, and D. E. Humphries, Journal of  
Applied Physics **94**, 7017 (2003).

117 J. Bennett, O. Warschkow, N. Marks, and D. McKenzie, Physical Review B  
**79** (2009).

118 C. Wellard, L. Hollenberg, and C. Pakes, Nanotechnology **13**, 570 (2002).

119 E. Kasper, *Properties of strained and relaxed silicon germanium* (INSPEC,  
Institution of electrical engineers London, 1995).

120 C. P. Poole and H. A. Farach, *Theory of magnetic resonance* (Wiley New  
York (NY) et al., 1987).

121 G. Feher, Physical Review **114**, 1219 (1959).

122 G. Lampel, Physical Review Letters **20**, 491 (1968).

123 S. Schofield, N. Curson, M. Simmons, F. Rueß, T. Hallam, L. Oberbeck, and  
R. Clark, Physical Review Letters **91**, 136104 (2003).

- <sup>124</sup> J. J. Pla, K. Y. Tan, J. P. Dehollain, W. H. Lim, J. J. Morton, D. N. Jamieson, A. S. Dzurak, and A. Morello, *Nature* **489**, 541 (2012).
- <sup>125</sup> J. J. Morton, D. R. McCamey, M. A. Eriksson, and S. A. Lyon, *Nature* **479**, 345 (2011).
- <sup>126</sup> M. Fuechsle, J. A. Miwa, S. Mahapatra, H. Ryu, S. Lee, O. Warschkow, L. C. L. Hollenberg, G. Klimeck, and M. Y. Simmons, *Nature Nanotechnology* **7**, 242 (2012).

## Appendix I

The electron wavefunctions and the energy levels of a donor phosphorus atom in a silicon host given below in table (I.1) and (I.2) were obtained by Ning and Sah after a modification to the effective-mass theory (EMT) proposed by Kohn and Luttinger. The modification was mainly the consideration of the splitting of the degenerated  $1s$  state due to the valley-orbit interaction effect, the so-called multivalley effective-mass theory (MEMT). The most prominent difference of the MEMT from the original EMT is the splitting of the degenerated ground state ( $1s$ ) into three separated states called  $A_1$ ,  $T_2$ , and  $E$  states. Ning and Sah further used the variational method to obtain the energy levels which were in close agreements with the measurement values. But the variational method resulted in different Bohr radii of the hydrogenic wavefunctions for the three splitted  $1s$  states. The consequence of the Ning and Sah's variational analysis is the wavefunctions for the  $A_1$ ,  $T_2$ , and  $E$  states are no longer orthogonal to the other high-order wavefunctions and this needs to be taken into account in the derivation of the perturbation theory.

Table I.1. Electron Wavefunctions for of a donor phosphorus atom in a silicon host

State	Wavefunction <sup>†</sup>	Hydrogenic fuction	Effective Bohr radius (m)
$1s(A_1)$	$\Psi_{1s(A_1)}(\mathbf{r}) = \frac{1}{\sqrt{6}} F_{1s(A_1)}(\mathbf{r})$ $[\varphi(k_x, \mathbf{r}) + \varphi(-k_x, \mathbf{r})$ $+ \varphi(k_y, \mathbf{r}) + \varphi(-k_y, \mathbf{r})$ $+ \varphi(k_z, \mathbf{r}) + \varphi(-k_z, \mathbf{r})]$	$F_{1s(A_1)}(\mathbf{r}) = \frac{1}{\sqrt{\pi}} \left( \frac{1}{a_{A_1}} \right)^{3/2} e^{-\frac{r}{a_{A_1}}}$	$a_{A_1} =$ $12.22 \times 10^{-10}$
$1s(T_2)$	$\Psi_{1s(T_2)}(\mathbf{r})$ $= \frac{1}{\sqrt{2}} F_{1s(T_2)}(\mathbf{r}) [\varphi(k_x, \mathbf{r}) - \varphi(-k_x, \mathbf{r})]$	$F_{1s(T_2)}(\mathbf{r}) = \frac{1}{\sqrt{\pi}} \left( \frac{1}{a_{T_2}} \right)^{3/2} e^{-\frac{r}{a_{T_2}}}$	$a_{T_2} =$ $17.83 \times 10^{-10}$

	$\Psi_{1s(T_2,2)}(\mathbf{r})$ $= \frac{1}{\sqrt{2}} F_{1s(T_2)}(\mathbf{r}) [\varphi(k_y, \mathbf{r}) - \varphi(-k_y, \mathbf{r})]$ $\Psi_{1s(T_2,3)}(\mathbf{r})$ $= \frac{1}{\sqrt{2}} F_{1s(T_2)}(\mathbf{r}) [\varphi(k_z, \mathbf{r}) - \varphi(-k_z, \mathbf{r})]$		
1s(E)	$\Psi_{1s(E,1)}(\mathbf{r}) = \frac{1}{2} F_{1s(E)}(\mathbf{r})$ $[\varphi(k_x, \mathbf{r}) + \varphi(-k_x, \mathbf{r})$ $- \varphi(k_y, \mathbf{r}) - \varphi(-k_y, \mathbf{r})]$ $\Psi_{1s(E,2)}(\mathbf{r}) = \frac{1}{\sqrt{12}} F_{1s(E)}(\mathbf{r})$ $[-\varphi(k_x, \mathbf{r}) - \varphi(-k_x, \mathbf{r})$ $- \varphi(k_y, \mathbf{r}) - \varphi(-k_y, \mathbf{r})$ $+ 2\varphi(k_z, \mathbf{r}) + 2\varphi(-k_z, \mathbf{r})]$	$F_{1s(E)}(\mathbf{r}) = \frac{1}{\sqrt{\pi}} \left( \frac{1}{a_E} \right)^{3/2} e^{-\frac{r}{a_E}}$	$a_E =$ $18.83 \times 10^{-10}$
2s	$\Psi_{2s}(\mathbf{r}) = \frac{1}{\sqrt{6}} F_{2s}(\mathbf{r})$ $[\varphi(k_x, \mathbf{r}) + \varphi(-k_x, \mathbf{r})$ $+ \varphi(k_y, \mathbf{r}) + \varphi(-k_y, \mathbf{r})$ $+ \varphi(k_z, \mathbf{r}) + \varphi(-k_z, \mathbf{r})]$	$F_{2s}(\mathbf{r}) = \frac{1}{4\sqrt{2\pi}} \left( \frac{1}{a^*} \right)^{3/2}$ $\left( 2 - \frac{r}{a^*} \right) e^{-\frac{r}{2a^*}}$	$a^* =$ $21.00 \times 10^{-10}$
2p	$\Psi_{2p_{10}}(\mathbf{r}) = \frac{1}{\sqrt{6}} F_{2p_{10}}(\mathbf{r})$ $[\varphi(k_x, \mathbf{r}) + \varphi(-k_x, \mathbf{r})$ $+ \varphi(k_y, \mathbf{r}) + \varphi(-k_y, \mathbf{r})$ $+ \varphi(k_z, \mathbf{r}) + \varphi(-k_z, \mathbf{r})]$	$F_{2p_{10}}(\mathbf{r}) = \frac{1}{4\sqrt{2\pi}} \left( \frac{1}{a^*} \right)^{3/2}$ $\frac{r}{a^*} e^{-\frac{r}{2a^*}} \cos \theta$	$a^* =$ $21.00 \times 10^{-10}$
	$\Psi_{2p_{11}}(\mathbf{r}) = \frac{1}{\sqrt{6}} F_{2p_{11}}(\mathbf{r})$ $[\varphi(k_x, \mathbf{r}) + \varphi(-k_x, \mathbf{r})$ $+ \varphi(k_y, \mathbf{r}) + \varphi(-k_y, \mathbf{r})$ $+ \varphi(k_z, \mathbf{r}) + \varphi(-k_z, \mathbf{r})]$	$F_{2p_{11}}(\mathbf{r}) = -\frac{1}{8\sqrt{\pi}} \left( \frac{1}{a^*} \right)^{3/2}$ $\frac{r}{a^*} e^{-\frac{r}{2a^*}} \sin \theta e^{i\phi}$	$a^* =$ $21.00 \times 10^{-10}$
	$\Psi_{2p_{1-1}}(\mathbf{r}) = \frac{1}{\sqrt{6}} F_{2p_{1-1}}(\mathbf{r})$ $[\varphi(k_x, \mathbf{r}) + \varphi(-k_x, \mathbf{r})$ $+ \varphi(k_y, \mathbf{r}) + \varphi(-k_y, \mathbf{r})$ $+ \varphi(k_z, \mathbf{r}) + \varphi(-k_z, \mathbf{r})]$	$F_{2p_{1-1}}(\mathbf{r}) = \frac{1}{8\sqrt{\pi}} \left( \frac{1}{a^*} \right)^{3/2}$ $\frac{r}{a^*} e^{-\frac{r}{2a^*}} \sin \theta e^{-i\phi}$	$a^* =$ $21.00 \times 10^{-10}$
3s	$\Psi_{3s}(\mathbf{r}) = \frac{1}{\sqrt{6}} F_{3s}(\mathbf{r})$ $[\varphi(k_x, \mathbf{r}) + \varphi(-k_x, \mathbf{r})$ $+ \varphi(k_y, \mathbf{r}) + \varphi(-k_y, \mathbf{r})$ $+ \varphi(k_z, \mathbf{r}) + \varphi(-k_z, \mathbf{r})]$	$F_{3s}(\mathbf{r}) = \frac{1}{81\sqrt{3\pi}} \left( \frac{1}{a^*} \right)^{3/2}$ $\left[ 27 - 18 \frac{r}{a^*} + 2 \left( \frac{r}{a^*} \right)^2 \right] e^{-\frac{r}{3a^*}}$	$a^* =$ $21.00 \times 10^{-10}$

3p	$\Psi_{3p_{10}}(\mathbf{r}) = \frac{1}{\sqrt{6}} F_{3p_{10}}(\mathbf{r})$ $[\varphi(k_x, \mathbf{r}) + \varphi(-k_x, \mathbf{r})$ $+ \varphi(k_y, \mathbf{r}) + \varphi(-k_y, \mathbf{r})$ $+ \varphi(k_z, \mathbf{r}) + \varphi(-k_z, \mathbf{r})]$	$F_{3p_{10}}(\mathbf{r}) = \frac{\sqrt{2}}{81\sqrt{\pi}} \left(\frac{1}{a^*}\right)^{3/2}$ $\left(6 - \frac{r}{a^*}\right) \frac{r}{a^*} e^{-\frac{r}{3a^*}} \cos \theta$	$a^* =$ $21.00 \times 10^{-10}$
	$\Psi_{3p_{11}}(\mathbf{r}) = \frac{1}{\sqrt{6}} F_{3p_{11}}(\mathbf{r})$ $[\varphi(k_x, \mathbf{r}) + \varphi(-k_x, \mathbf{r})$ $+ \varphi(k_y, \mathbf{r}) + \varphi(-k_y, \mathbf{r})$ $+ \varphi(k_z, \mathbf{r}) + \varphi(-k_z, \mathbf{r})]$	$F_{3p_{11}}(\mathbf{r}) = -\frac{\sqrt{2}}{81\sqrt{\pi}} \left(\frac{1}{a^*}\right)^{3/2}$ $\left(6 - \frac{r}{a^*}\right) \frac{r}{a^*} e^{-\frac{r}{3a^*}} \sin \theta e^{j\phi}$	$a^* =$ $21.00 \times 10^{-10}$
	$\Psi_{3p_{1-1}}(\mathbf{r}) = \frac{1}{\sqrt{6}} F_{3p_{1-1}}(\mathbf{r})$ $[\varphi(k_x, \mathbf{r}) + \varphi(-k_x, \mathbf{r})$ $+ \varphi(k_y, \mathbf{r}) + \varphi(-k_y, \mathbf{r})$ $+ \varphi(k_z, \mathbf{r}) + \varphi(-k_z, \mathbf{r})]$	$F_{3p_{1-1}}(\mathbf{r}) = \frac{\sqrt{2}}{81\sqrt{\pi}} \left(\frac{1}{a^*}\right)^{3/2}$ $\left(6 - \frac{r}{a^*}\right) \frac{r}{a^*} e^{-\frac{r}{3a^*}} \sin \theta e^{-j\phi}$	$a^* =$ $21.00 \times 10^{-10}$
3d	$\Psi_{3d_{20}}(\mathbf{r}) = \frac{1}{\sqrt{6}} F_{3d_{20}}(\mathbf{r})$ $[\varphi(k_x, \mathbf{r}) + \varphi(-k_x, \mathbf{r})$ $+ \varphi(k_y, \mathbf{r}) + \varphi(-k_y, \mathbf{r})$ $+ \varphi(k_z, \mathbf{r}) + \varphi(-k_z, \mathbf{r})]$	$F_{3d_{20}}(\mathbf{r}) = \frac{1}{81\sqrt{6\pi}} \left(\frac{1}{a^*}\right)^{3/2}$ $\left(\frac{r}{a^*}\right)^2 e^{-\frac{r}{3a^*}} (3\cos^2 \theta - 1)$	$a^* =$ $21.00 \times 10^{-10}$
	$\Psi_{3d_{21}}(\mathbf{r}) = \frac{1}{\sqrt{6}} F_{3d_{21}}(\mathbf{r})$ $[\varphi(k_x, \mathbf{r}) + \varphi(-k_x, \mathbf{r})$ $+ \varphi(k_y, \mathbf{r}) + \varphi(-k_y, \mathbf{r})$ $+ \varphi(k_z, \mathbf{r}) + \varphi(-k_z, \mathbf{r})]$	$F_{3d_{21}}(\mathbf{r}) = -\frac{1}{81\sqrt{6\pi}} \left(\frac{1}{a^*}\right)^{3/2}$ $\left(\frac{r}{a^*}\right)^2 e^{-\frac{r}{3a^*}} \sin \theta \cos \theta e^{j\phi}$	$a^* =$ $21.00 \times 10^{-10}$
	$\Psi_{3d_{2-1}}(\mathbf{r}) = \frac{1}{\sqrt{6}} F_{3d_{2-1}}(\mathbf{r})$ $[\varphi(k_x, \mathbf{r}) + \varphi(-k_x, \mathbf{r})$ $+ \varphi(k_y, \mathbf{r}) + \varphi(-k_y, \mathbf{r})$ $+ \varphi(k_z, \mathbf{r}) + \varphi(-k_z, \mathbf{r})]$	$F_{3d_{2-1}}(\mathbf{r}) = \frac{1}{81\sqrt{6\pi}} \left(\frac{1}{a^*}\right)^{3/2}$ $\left(\frac{r}{a^*}\right)^2 e^{-\frac{r}{3a^*}} \sin \theta \cos \theta e^{-j\phi}$	$a^* =$ $21.00 \times 10^{-10}$
	$\Psi_{3d_{22}}(\mathbf{r}) = \frac{1}{\sqrt{6}} F_{3d_{22}}(\mathbf{r})$ $[\varphi(k_x, \mathbf{r}) + \varphi(-k_x, \mathbf{r})$ $+ \varphi(k_y, \mathbf{r}) + \varphi(-k_y, \mathbf{r})$ $+ \varphi(k_z, \mathbf{r}) + \varphi(-k_z, \mathbf{r})]$	$F_{3d_{22}}(\mathbf{r}) = -\frac{1}{162\sqrt{\pi}} \left(\frac{1}{a^*}\right)^{3/2}$ $\left(\frac{r}{a^*}\right)^2 e^{-\frac{r}{3a^*}} \sin^2 \theta e^{j2\phi}$	$a^* =$ $21.00 \times 10^{-10}$
	$\Psi_{3d_{2-2}}(\mathbf{r}) = \frac{1}{\sqrt{6}} F_{3d_{2-2}}(\mathbf{r})$ $[\varphi(k_x, \mathbf{r}) + \varphi(-k_x, \mathbf{r})$ $+ \varphi(k_y, \mathbf{r}) + \varphi(-k_y, \mathbf{r})$ $+ \varphi(k_z, \mathbf{r}) + \varphi(-k_z, \mathbf{r})]$	$F_{3d_{2-2}}(\mathbf{r}) = \frac{1}{162\sqrt{\pi}} \left(\frac{1}{a^*}\right)^{3/2}$ $\left(\frac{r}{a^*}\right)^2 e^{-\frac{r}{3a^*}} \sin^2 \theta e^{-j2\phi}$	$a^* =$ $21.00 \times 10^{-10}$



†where  $\mathbf{r} = (r, \theta, \phi)$  and  $\varphi(\pm k_i, \mathbf{r})$  (with  $i = x, y, z$ ) are the Bloch wavefunctions

Table I.2. Electron energy Levels of a donor phosphorus atom in a silicon host

State	Energy Level (reference from conduction band minimum) (meV)	
	Theory	Measurement
$1s(A_1)$	$E_{A_1} = -45.469$	$E_{A_1} = -45.47$
$1s(T_2)$	$E_{T_2} = -33.740$	$E_{T_2} = -33.74$
$1s(E)$	$E_E = -32.376$	$E_E = -32.37$
$2s$	$E_{2s} = -7.469^*$	$E_{2s} = -6.33$
$3s$	$E_{3s} = -3.320^*$	$E_{3s} = -3.06$

\*These values are obtained from a simple single-valley EMT instead.

## Appendix II

The perturbed ground-state wavefunction is expanded up to the 3s state while contributions from higher states are ignored. Note that the expansion coefficients associated with the  $\Psi_{T_2}$  and  $\Psi_E$  states vanish. Contributions of  $\Psi_{2p}(0)$ ,  $\Psi_{3p}(0)$ , and  $\Psi_{3d}(0)$  at the phosphorus nucleus site are all zero. The remaining expansion coefficients in equation (2.40) are given below:

$$\begin{aligned}
\lambda^2 \alpha_{A_1}^{(2)} = & -\frac{1}{2} \left( \lambda^2 |\alpha_{A_1}^{(1)}|^2 + \lambda^2 |\alpha_{2s}^{(1)}|^2 + \lambda^2 |\alpha_{3s}^{(1)}|^2 \right. \\
& \left. + \lambda^2 |\alpha_{2p_{10}}^{(1)}|^2 + \lambda^2 |\alpha_{2p_{11}}^{(1)}|^2 + \lambda^2 |\alpha_{2p_{1-1}}^{(1)}|^2 \right) \\
& -\frac{1}{2} \left( \lambda^2 |\alpha_{3p_{10}}^{(1)}|^2 + \lambda^2 |\alpha_{3p_{11}}^{(1)}|^2 + \lambda^2 |\alpha_{3p_{1-1}}^{(1)}|^2 \right) \\
& -\frac{1}{2} \left( \lambda^2 |\alpha_{3d_{20}}^{(1)}|^2 + \lambda^2 |\alpha_{3d_{21}}^{(1)}|^2 + \lambda^2 |\alpha_{3d_{2-1}}^{(1)}|^2 \right. \\
& \left. + \lambda^2 |\alpha_{3d_{22}}^{(1)}|^2 + \lambda^2 |\alpha_{3d_{2-2}}^{(1)}|^2 \right) \\
& -\text{Re} \left\{ \lambda^2 \alpha_{2s}^{(2)} H_{2sA_1} + \lambda^2 \alpha_{3s}^{(2)} H_{3sA_1} \right\} \\
& -\text{Re} \left\{ \lambda \alpha_{A_1}^{(1)*} \lambda \alpha_{2s}^{(1)} H_{2sA_1} \right\} \\
& -\text{Re} \left\{ \lambda \alpha_{A_1}^{(1)*} \lambda \alpha_{3s}^{(1)} H_{3sA_1} \right\}
\end{aligned} \tag{II-1}$$

$$\begin{aligned}
\lambda \alpha_{2s}^{(1)} = & \frac{1}{(E_{A_1} - E_2)(1 - H_{2sA_1}^2 - H_{3sA_1}^2)} \times \\
& (H_{V2sA_1}(1 - H_{3sA_1}^2) + H_{V3sA_1}H_{2sA_1}H_{3sA_1} - H_{VA_1A_1}H_{2sA_1})
\end{aligned} \tag{II-2}$$

$$\begin{aligned}
\lambda^2 \alpha_{2s}^{(2)} &= \frac{1}{(E_{A_1} - E_2)(1 - H_{2sA_1}^2 - H_{3sA_1}^2)} \times \\
&\left\{ \left( \lambda \alpha_{A_1}^{(1)} H_{V2sA_1} + \lambda \alpha_{2s}^{(1)} H_{V2s2s} + \lambda \alpha_{2p_{10}}^{(1)} H_{V2s2p_{10}} \right. \right. \\
&+ \lambda \alpha_{2p_{11}}^{(1)} H_{V2s2p_{11}} + \lambda \alpha_{2p_{1-1}}^{(1)} H_{V2s2p_{1-1}} \\
&+ \lambda \alpha_{3s}^{(1)} H_{V2s3s} + \lambda \alpha_{3p_{10}}^{(1)} H_{V2s3p_{10}} + \lambda \alpha_{3p_{11}}^{(1)} H_{V2s3p_{11}} \\
&+ \lambda \alpha_{3p_{1-1}}^{(1)} H_{V2s3p_{1-1}} + \lambda \alpha_{3d_{20}}^{(1)} H_{V2s3d_{20}} + \lambda \alpha_{3d_{21}}^{(1)} H_{V2s3d_{21}} \\
&+ \lambda \alpha_{3d_{2-1}}^{(1)} H_{V2s3d_{2-1}} + \lambda \alpha_{3d_{22}}^{(1)} H_{V2s3d_{22}} \\
&\left. + \lambda \alpha_{3d_{2-2}}^{(1)} H_{V2s3d_{2-2}} \right) (1 - H_{3sA_1}^2) \\
&+ \left( \lambda \alpha_{A_1}^{(1)} H_{V3sA_1} + \lambda \alpha_{2s}^{(1)} H_{V3s2s} + \lambda \alpha_{2p_{10}}^{(1)} H_{V3s2p_{10}} \right. \\
&+ \lambda \alpha_{2p_{11}}^{(1)} H_{V3s2p_{11}} + \lambda \alpha_{2p_{1-1}}^{(1)} H_{V3s2p_{1-1}} \\
&+ \lambda \alpha_{3s}^{(1)} H_{V3s3s} + \lambda \alpha_{3p_{10}}^{(1)} H_{V3s3p_{10}} + \lambda \alpha_{3p_{11}}^{(1)} H_{V3s3p_{11}} \\
&+ \lambda \alpha_{3p_{1-1}}^{(1)} H_{V3s3p_{1-1}} + \lambda \alpha_{3d_{20}}^{(1)} H_{V3s3d_{20}} + \lambda \alpha_{3d_{21}}^{(1)} H_{V3s3d_{21}} \\
&+ \lambda \alpha_{3d_{2-1}}^{(1)} H_{V3s3d_{2-1}} + \lambda \alpha_{3d_{22}}^{(1)} H_{V3s3d_{22}} + \lambda \alpha_{3d_{2-2}}^{(1)} H_{V3s3d_{2-2}} \left. \right) H_{3sA_1} H_{2sA_1} \\
&- \left( \lambda \alpha_{A_1}^{(1)} H_{VA_1A_1} + \lambda \alpha_{2s}^{(1)} H_{VA_12s} + \lambda \alpha_{2p_{10}}^{(1)} H_{VA_12p_{10}} \right. \\
&+ \lambda \alpha_{2p_{11}}^{(1)} H_{VA_12p_{11}} + \lambda \alpha_{2p_{1-1}}^{(1)} H_{VA_12p_{1-1}} + \lambda \alpha_{3s}^{(1)} H_{VA_13s} + \lambda \alpha_{3p_{10}}^{(1)} H_{VA_13p_{10}} \\
&+ \lambda \alpha_{3p_{11}}^{(1)} H_{VA_13p_{11}} + \lambda \alpha_{3p_{1-1}}^{(1)} H_{VA_13p_{1-1}} + \lambda \alpha_{3d_{20}}^{(1)} H_{VA_13d_{20}} + \lambda \alpha_{3d_{21}}^{(1)} H_{VA_13d_{21}} \\
&+ \lambda \alpha_{3d_{2-1}}^{(1)} H_{VA_13d_{2-1}} + \lambda \alpha_{3d_{22}}^{(1)} H_{VA_13d_{22}} + \lambda \alpha_{3d_{2-2}}^{(1)} H_{VA_13d_{2-2}} \left. \right) H_{2sA_1} \\
&- \lambda E^{(1)} \left( \lambda \alpha_{A_1}^{(1)} H_{2sA_1} + \lambda \alpha_{2s}^{(1)} \right) (1 - H_{3sA_1}^2) \\
&- \lambda E^{(1)} \left( \lambda \alpha_{A_1}^{(1)} H_{3sA_1} + \lambda \alpha_{3s}^{(1)} \right) H_{3sA_1} H_{2sA_1} \\
&\left. + \lambda E^{(1)} \left( \lambda \alpha_{A_1}^{(1)} + \lambda \alpha_{2s}^{(1)} H_{A_12s} + \lambda \alpha_{3s}^{(1)} H_{A_13s} \right) H_{2sA_1} \right\}
\end{aligned} \tag{II-3}$$

$$\begin{aligned}
\lambda \alpha_{3s}^{(1)} &= \frac{1}{(E_{A_1} - E_3)(1 - H_{2sA_1}^2 - H_{3sA_1}^2)} \times \\
&\left\{ H_{V3sA_1} (1 - H_{2sA_1}^2) + H_{V2sA_1} H_{2sA_1} H_{3sA_1} - H_{VA_1A_1} H_{3sA_1} \right\}
\end{aligned} \tag{II-4}$$

$$\begin{aligned}
\lambda^2 \alpha_{3s}^{(2)} &= \frac{1}{(E_{A_1} - E_3)(1 - H_{2sA_1}^2 - H_{3sA_1}^2)} \times \\
&\left\{ \left( \lambda \alpha_{A_1}^{(1)} H_{V3sA_1} + \lambda \alpha_{2s}^{(1)} H_{V3s2s} + \lambda \alpha_{2p_{10}}^{(1)} H_{V3s2p_{10}} + \lambda \alpha_{2p_{11}}^{(1)} H_{V3s2p_{11}} \right. \right. \\
&+ \lambda \alpha_{2p_{1-1}}^{(1)} H_{V3s2p_{1-1}} + \lambda \alpha_{3s}^{(1)} H_{V3s3s} + \lambda \alpha_{3p_{10}}^{(1)} H_{V3s3p_{10}} + \lambda \alpha_{3p_{11}}^{(1)} H_{V3s3p_{11}} \\
&+ \lambda \alpha_{3p_{1-1}}^{(1)} H_{V3s3p_{1-1}} + \lambda \alpha_{3d_{20}}^{(1)} H_{V3s3d_{20}} + \lambda \alpha_{3d_{21}}^{(1)} H_{V3s3d_{21}} + \lambda \alpha_{3d_{2-1}}^{(1)} H_{V3s3d_{2-1}} \\
&+ \left. \lambda \alpha_{3d_{22}}^{(1)} H_{V3s3d_{22}} + \lambda \alpha_{3d_{2-2}}^{(1)} H_{V3s3d_{2-2}} \right) (1 - H_{2sA_1}^2) \\
&\left( \lambda \alpha_{A_1}^{(1)} H_{V2sA_1} + \lambda \alpha_{2s}^{(1)} H_{V2s2s} + \lambda \alpha_{2p_{10}}^{(1)} H_{V2s2p_{10}} + \lambda \alpha_{2p_{11}}^{(1)} H_{V2s2p_{11}} \right. \\
&+ \lambda \alpha_{2p_{1-1}}^{(1)} H_{V2s2p_{1-1}} + \lambda \alpha_{3s}^{(1)} H_{V2s3s} + \lambda \alpha_{3p_{10}}^{(1)} H_{V2s3p_{10}} + \lambda \alpha_{3p_{11}}^{(1)} H_{V2s3p_{11}} \\
&+ \lambda \alpha_{3p_{1-1}}^{(1)} H_{V2s3p_{1-1}} + \lambda \alpha_{3d_{20}}^{(1)} H_{V2s3d_{20}} + \lambda \alpha_{3d_{21}}^{(1)} H_{V2s3d_{21}} + \lambda \alpha_{3d_{2-1}}^{(1)} H_{V2s3d_{2-1}} \\
&+ \left. \lambda \alpha_{3d_{22}}^{(1)} H_{V2s3d_{22}} + \lambda \alpha_{3d_{2-2}}^{(1)} H_{V2s3d_{2-2}} \right) H_{2sA_1} H_{3sA_1} \\
&- \left( \lambda \alpha_{A_1}^{(1)} H_{VA_1A_1} + \lambda \alpha_{2s}^{(1)} H_{VA_12s} + \lambda \alpha_{2p_{10}}^{(1)} H_{VA_12p_{10}} + \lambda \alpha_{2p_{11}}^{(1)} H_{VA_12p_{11}} \right. \\
&+ \lambda \alpha_{2p_{1-1}}^{(1)} H_{VA_12p_{1-1}} + \lambda \alpha_{3s}^{(1)} H_{VA_13s} + \lambda \alpha_{3p_{10}}^{(1)} H_{VA_13p_{10}} + \lambda \alpha_{3p_{11}}^{(1)} H_{VA_13p_{11}} \\
&+ \lambda \alpha_{3p_{1-1}}^{(1)} H_{VA_13p_{1-1}} + \lambda \alpha_{3d_{20}}^{(1)} H_{VA_13d_{20}} + \lambda \alpha_{3d_{21}}^{(1)} H_{VA_13d_{21}} + \lambda \alpha_{3d_{2-1}}^{(1)} H_{VA_13d_{2-1}} \\
&+ \left. \lambda \alpha_{3d_{22}}^{(1)} H_{VA_13d_{22}} + \lambda \alpha_{3d_{2-2}}^{(1)} H_{VA_13d_{2-2}} \right) H_{3sA_1} \\
&- \lambda E^{(1)} \left( \lambda \alpha_{A_1}^{(1)} H_{3sA_1} + \lambda \alpha_{3s}^{(1)} \right) (1 - H_{2sA_1}^2) \\
&- \lambda E^{(1)} \left( \lambda \alpha_{A_1}^{(1)} H_{2sA_1} + \lambda \alpha_{2s}^{(1)} \right) H_{3sA_1} H_{2sA_1} \\
&+ \left. \lambda E^{(1)} \left( \lambda \alpha_{A_1}^{(1)} + \lambda \alpha_{2s}^{(1)} H_{A_12s} + \lambda \alpha_{3s}^{(1)} H_{A_13s} \right) H_{3sA_1} \right\} \tag{II-5}
\end{aligned}$$

In equations (II-1), (II-3), and (II-5), the additional expansion coefficients for the  $p$  and  $d$  sub-shells of the first order perturbation wavefunction are:

$$\lambda \alpha_{2p_{10}}^{(1)} = \frac{H_{V2p_{10}A_1}}{E_{A_1} - E_2}, \quad \lambda \alpha_{2p_{11}}^{(1)} = \frac{H_{V2p_{11}A_1}}{E_{A_1} - E_2}, \quad \lambda \alpha_{2p_{1-1}}^{(1)} = \frac{H_{V2p_{1-1}A_1}}{E_{A_1} - E_2}, \tag{II-6}$$

$$\lambda \alpha_{3p_{10}}^{(1)} = \frac{H_{V3p_{10}A_1}}{E_{A_1} - E_3}, \quad \lambda \alpha_{3p_{11}}^{(1)} = \frac{H_{V3p_{11}A_1}}{E_{A_1} - E_3}, \quad \lambda \alpha_{3p_{1-1}}^{(1)} = \frac{H_{V3p_{1-1}A_1}}{E_{A_1} - E_3}, \tag{II-7}$$

$$\lambda\alpha_{3d_{20}}^{(1)} = \frac{H_{V3d_{20}A_1}}{E_{A_1} - E_3}, \quad \lambda\alpha_{3d_{21}}^{(1)} = \frac{H_{V3d_{21}A_1}}{E_{A_1} - E_3}, \quad \lambda\alpha_{3d_{2-1}}^{(1)} = \frac{H_{V3d_{2-1}A_1}}{E_{A_1} - E_3},$$

$$\lambda\alpha_{3d_{22}}^{(1)} = \frac{H_{V3d_{22}A_1}}{E_{A_1} - E_3}, \quad \lambda\alpha_{3d_{2-2}}^{(1)} = \frac{H_{V3d_{2-2}A_1}}{E_{A_1} - E_3}. \quad (\text{II-8})$$

In the equations, (II-1)-(II-8), the various “ $H$ ” terms are defined as below:

$$H_{\alpha\beta} = \langle \Psi_\alpha | \Psi_\beta \rangle, \text{ where } \alpha \text{ and } \beta \text{ stand for different states} \quad (\text{II-9})$$

and

$$H_{V\alpha\beta} = \langle \Psi_\alpha(\mathbf{r}) | H_V | \Psi_\beta(\mathbf{r}) \rangle. \quad (\text{II-10})$$

For example,

$$\begin{aligned} H_{V_{A_1A_1}} &= \langle \Psi_{A_1}(\mathbf{r}) | H_V | \Psi_{A_1}(\mathbf{r}) \rangle \\ &= \iiint_{V_0} \frac{1}{\sqrt{6}} F_{A_1}^{1s*}(\mathbf{r}) \frac{1}{\sqrt{6}} F_{A_1}^{1s}(\mathbf{r}) eV(\mathbf{r}) \cdot [\phi^*(k_x, \mathbf{r}) + \phi^*(-k_x, \mathbf{r}) \\ &\quad + \phi^*(k_y, \mathbf{r}) + \phi^*(-k_y, \mathbf{r}) + \phi^*(k_z, \mathbf{r}) + \phi^*(-k_z, \mathbf{r})] \cdot [\phi(k_x, \mathbf{r}) \\ &\quad + \phi(-k_x, \mathbf{r}) + \phi(k_y, \mathbf{r}) + \phi(-k_y, \mathbf{r}) + \phi(k_z, \mathbf{r}) + \phi(-k_z, \mathbf{r})] d\mathbf{r} \\ &\approx \sum_{m=1}^N \frac{1}{\sqrt{6}} F_{A_1}^{1s*}(\mathbf{r}_m) \frac{1}{\sqrt{6}} F_{A_1}^{1s}(\mathbf{r}_m) eV(\mathbf{r}_m) \\ &\quad \cdot \iiint_{\Omega} [\phi^*(k_x, \mathbf{r}) + \phi^*(-k_x, \mathbf{r}) + \phi^*(k_y, \mathbf{r}) + \phi^*(-k_y, \mathbf{r}) \\ &\quad + \phi^*(k_z, \mathbf{r}) + \phi^*(-k_z, \mathbf{r})] \cdot [\phi(k_x, \mathbf{r}) + \phi(-k_x, \mathbf{r}) + \phi(k_y, \mathbf{r}) \\ &\quad + \phi(-k_y, \mathbf{r}) + \phi(k_z, \mathbf{r}) + \phi(-k_z, \mathbf{r})] d\mathbf{r} \\ &= \sum_{m=1}^N \frac{1}{\sqrt{6}} F_{A_1}^{1s*}(\mathbf{r}_m) \frac{1}{\sqrt{6}} F_{A_1}^{1s}(\mathbf{r}_m) eV(\mathbf{r}_m) \cdot \Omega \cdot 6 \\ &= \Omega \sum_{m=1}^N F_{A_1}^{1s*}(\mathbf{r}_m) F_{A_1}^{1s}(\mathbf{r}_m) eV(\mathbf{r}_m) \end{aligned} \quad (\text{II-11})$$

Here  $\Omega$  is the volume of silicon unit cell,  $N$  is the number of unit cells in the silicon substrate layer (total volume is  $V_0$ ), and  $\mathbf{r}_m$  is the coordinate representing the center of the  $m$ th unit cell. For further simplification of Eq.

(II-10), the hydrogenic orbital wavefunction  $F_{A_1}^{1s}(\mathbf{r})$  and the potential distribution function  $V(\mathbf{r})$  due to the external A-gate voltage are assumed to be slow-varying functions with negligible variations inside a unit cell.

In simplifying the result in Eq. (II-10), we have assumed that the hydrogenic wavefunction  $F_{A_1}^{1s}(\mathbf{r})$  and the potential function  $V(\mathbf{r})$  due to the gate voltage are slow-varying functions and almost constant within a unit cell. It should be noted that the Bloch wave functions represented here are ortho-normalized. If the potential distribution function due to the gate voltage  $V(\mathbf{r}_m)$  is known, equation (II-11) can be numerically calculated.

Similarly, we have

$$H_{V_{2sA_1}} = \langle \Psi_{2s}(\mathbf{r}) | H_V | \Psi_{A_1}(\mathbf{r}) \rangle \approx \Omega \sum_{m=1}^N F_{2s}^*(\mathbf{r}_m) F_{A_1}^{1s}(\mathbf{r}_m) eV(\mathbf{r}_m) \quad (\text{II-12})$$

$$H_{V_{3sA_1}} = \langle \Psi_{3s}(\mathbf{r}) | H_V | \Psi_{A_1}(\mathbf{r}) \rangle \approx \Omega \sum_{m=1}^N F_{3s}^*(\mathbf{r}_m) F_{A_1}^{1s}(\mathbf{r}_m) eV(\mathbf{r}_m) \quad (\text{II-13})$$

The terms  $\langle \Psi_{2s}(\mathbf{r}) | \Psi_{A_1}(\mathbf{r}) \rangle$  and  $\langle \Psi_{3s}(\mathbf{r}) | \Psi_{A_1}(\mathbf{r}) \rangle$  are independent of the external applied A-gate voltage and can be numerically calculated. That is,

$$\begin{aligned} \langle \Psi_{2s}(\mathbf{r}) | \Psi_{A_1}(\mathbf{r}) \rangle &= \langle \Psi_{A_1}(\mathbf{r}) | \Psi_{2s}(\mathbf{r}) \rangle \\ &\approx \sum_{m=1}^N \frac{1}{\sqrt{6}} F_{2s}^*(\mathbf{r}_m) \frac{1}{\sqrt{6}} F_{A_1}^{1s}(\mathbf{r}_m) \cdot \Omega \cdot 6 \\ &= \Omega \sum_{m=1}^N F_{2s}^*(\mathbf{r}_m) F_{A_1}^{1s}(\mathbf{r}_m) \\ &= \iiint_V F_{2s}^*(\mathbf{r}) F_{A_1}^{1s}(\mathbf{r}) d\mathbf{r} = 0.71 \end{aligned} \quad (\text{II-14})$$

and

$$\langle \Psi_{3s}(\mathbf{r}) | \Psi_{A_1}(\mathbf{r}) \rangle = \langle \Psi_{A_1}(\mathbf{r}) | \Psi_{3s}(\mathbf{r}) \rangle \approx 0.27 \quad (\text{II-15})$$

The energy of the ground-state  $E_{A_1}$ , has been obtained before by Ning and Sah using the variational method and its value with respect to the conduction band

minimum is equal to 45.47 meV. The value of higher order excited states energies  $E_2$  and  $E_3$  are 7.5 meV and 3.3 meV, respectively, with respect to the conduction band minimum.